

AD-A119 078

NAVAL RESEARCH LAB WASHINGTON DC

F/O 20/9

THE LASSII PROGRAM: OBJECTIVES, SPACECRAFT DESIGN, AND MISSION --ETC(U)

JUN 82 E P SZUSZCZENICZ, R E PALMA

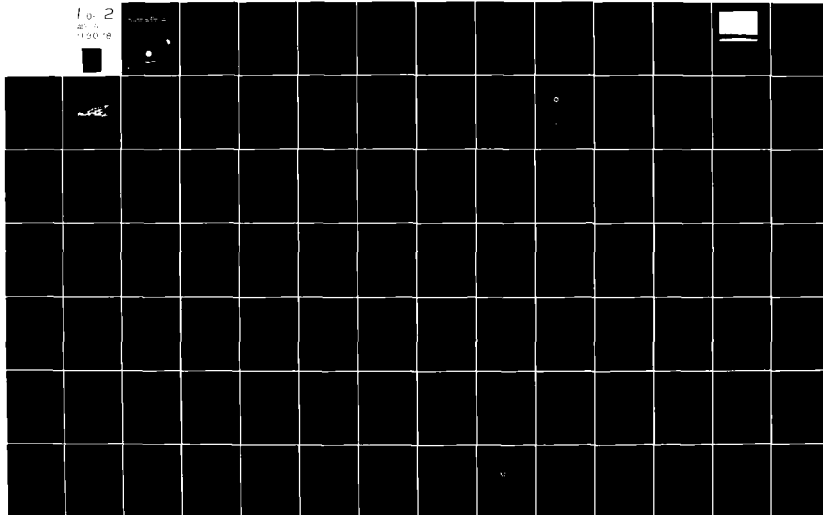
NRL-8420

NL

UNCLASSIFIED

10-2  
20-5  
11-20-18

10-2  
20-5  
11-20-18



AD A119078

NRL Report 540

# **The LASSII Program Objectives, Spacecraft Design, and Mission Scenarios for Full-Scale, Shuttle-Launched, Free-Flyer Operations**

**EDWARD P. SAMULOWICZ**

*Space Science Division*

and

**ROBERT E. PALMA**

*Space Science Division*

June 16, 1982

DTIC  
ECTE

SEP 8 1982

H

SECURITY CLASSIFICATION OF THIS PAGE (When Data Entered)

REPORT DOCUMENTATION PAGE		READ INSTRUCTIONS BEFORE COMPLETING FORM
1. REPORT NUMBER NRL Report 8420	2. GOVT ACCESSION NO. AD-A119 078	3. RECIPIENT'S CATALOG NUMBER
4. TITLE (and Subtitle) THE LASSII PROGRAM OBJECTIVES, SPACECRAFT DESIGN, AND MISSION SCENARIOS FOR FULL-SCALE, SHUTTLE-LAUNCHED, FREE-FLYER OPERATIONS		5. TYPE OF REPORT & PERIOD COVERED Interim report on a continuing NRL problem
7. AUTHOR(s)  Edward P. Szuszczewicz and Robert E. Palma		6. PERFORMING ORG. REPORT NUMBER
9. PERFORMING ORGANIZATION NAME AND ADDRESS  Naval Research Laboratory Washington, DC 20375		8. CONTRACT OR GRANT NUMBER(s)
11. CONTROLLING OFFICE NAME AND ADDRESS  Office of Naval Research Arlington, VA 22217		10. PROGRAM ELEMENT, PROJECT, TASK AREA & WORK UNIT NUMBERS  NRL Problem 41-0949-0-2 Subtask RR0330244
14. MONITORING AGENCY NAME & ADDRESS (if different from Controlling Office)		12. REPORT DATE June 16, 1982
		13. NUMBER OF PAGES 127
		15. SECURITY CLASS. (of this report) UNCLASSIFIED
		15a. DECLASSIFICATION/DOWNGRADING SCHEDULE
16. DISTRIBUTION STATEMENT (of this Report)  Approved for public release; distribution unlimited.		
17. DISTRIBUTION STATEMENT (of the abstract entered in Block 20, if different from Report)		
18. SUPPLEMENTARY NOTES		
19. KEY WORDS (Continue on reverse side if necessary and identify by block number)  Ionosphere                      Communication effects Shuttle                          Spacecraft technology Active plasma experiments		
20. ABSTRACT (Continue on reverse side if necessary and identify by block number)  The LASSII concept is simple, but fundamentally different from that of any past or present satellite mission: to employ a sortie-mode free-flying satellite which is launched and recovered by Shuttle, and instrumented with a complement of plasma diagnostic tools which have been specifically designed to spatially and temporally resolve all active elements within an ionospheric irregularity and determine associated effects on relevant military channels. The satellite, configured for maximum flexibility as an investigative platform, will co-orbit in tandem or in overflight with a  (Continued)		

DD FORM 1 JAN 73 1473

EDITION OF 1 NOV 65 IS OBSOLETE  
S/N 0102-014-6601

SECURITY CLASSIFICATION OF THIS PAGE (When Data Entered)

## 20. ABSTRACT (Continued)

Shuttle-borne plasma diagnostics complement, making possible separation of space and time dependencies and allowing important determinations of growth and transport mechanisms in turbulent ionospheric plasmas. The satellite will be able to execute Hohmann and Crocco maneuvers with complete flexibility for selection of time spacing between Shuttle-borne and LASSII free-flyer measurements of a given ionospheric volume while satellite-to-ground and satellite-to-satellite systems tests are executed.

The uniqueness of the LASSII concept makes it compatible with all Shuttle orbits from 200 to 1000 km and for all inclinations. The nature of the program, with emphasis on naturally occurring as well as artificially produced ionospheric irregularities, is also easily accommodated by Shuttle regardless of season or solar conditions. Program planning will focus on short-duration (7 to 30 days) experiments which will take advantage of built-in flexibility in the LASSII payload complement. The experiment duration will help develop efficiency through a concentrated approach to research problems designed to provide near-term solutions to issues of immediate military concern.

Accession For	
NTIS GRA&I	<input checked="" type="checkbox"/>
DTIC TAB	<input type="checkbox"/>
Unannounced	<input type="checkbox"/>
Justification	
By	
Distribution/	
Availability Codes	
Dist	Avail and/or Special
A	



## PREFACE

The Department of Defense has a continuing need for improved understanding of plasma processes in the near-Earth charged-particle environment and their relationship to military systems. In the case of transionospheric radio wave propagation, it is important to know ionospheric plasma production-loss mechanisms and the multitude of processes which control distribution and kinetics. Over the years, ground-based radar and ionosonde measurements as well as "in situ" rocket and satellite data have coupled with developing theoretical and computational models to provide basic descriptions of ionospheric conditions which can affect command, control, communications, and intelligence (C<sup>3</sup>I) systems operating in the military network. More recently, advancing technology and improved scientific understanding have been able to probe beyond these basic descriptions of the zero-order quiet ionosphere. Efforts are now focusing on the details of the fundamental cause-effect relationships responsible for ionospheric irregularities, associated plasma instability mechanisms, and associated C<sup>3</sup>I outages. These efforts represent important challenges in an ever-maturing science which looks to the quiet and turbulent ionosphere as a charged-particle environment that can be modified, controlled, and utilized for plasma and systems experiments untenable in confining laboratory chambers.

To meet this challenge the Naval Research Laboratory in collaboration with a number of government agencies, universities, and private institutions has developed the LASSII (Low Altitude Satellite Study of Ionospheric Irregularities) concept in a way intended to synthesize military needs with the latest thinking in theoretical and experimental plasma physics, ionospheric research, spacecraft technology, and communication engineering. An admittedly ambitious objective in the face of dwindling budgets and dynamic developments in science and Shuttle engineering, the task was lightened by unselfish contributions from many individuals in private and government sectors who believed in the concept, its goals, and unique capabilities to exploit the Space Shuttle. Threaded throughout this document are their shared experiences, insights, and guidelines. Without their help, this effort would have been impossible. To all these contributors we dedicate this document with the hope that continued interactions will eliminate any shortcomings and improve the overall concept.

As is always the case in an endeavor of this magnitude, changes take place before and during the actual publication of the program plan. Indeed, since the first draft of this document there have been many advances in the understanding of naturally occurring and artificially induced ionospheric irregularities. The advances have been substantial in their own right and continue to strengthen the fundamental LASSII concept. In the passing of time (almost 2 years), several of the related programs discussed in §3.4 have come to fruition, and their results appear in the scientific literature. The spacecraft configuration is unchanged, and the planning principles, mission scenarios, and objectives have remained intact. In addition, the LASSII concept has entered Phase I of what is hoped to be a three-phase effort resulting in the full-scale program described between these covers. Phase I represents the Shuttle-borne instrument complement designed to operate in tandem with the Shuttle-launched LASSII free-flyer. Phase II is a descoped free-flyer configuration with limited capabilities but with substantially lower budgetary requirements. Phase III represents the full-scale LASSII capability... a multiagency, multipurpose, maneuverable spacecraft, launched and recovered by Shuttle, with built-in flexibility in the payload complement to provide near-term solutions to issues of immediate military concern.

To all my colleagues I extend my deepest appreciation for unselfish contributions to the development of the LASSII concept and the definition of instrumentation, spacecraft design, and mission scenarios.

Edward P. Szuszczewicz  
LASSII Program Manager

## CONTENTS

PREFACE .....	iii
PROGRAM MANAGEMENT .....	vii
PARTICIPANTS IN PLANNING MEETINGS AND MISSION DEFINITION .....	viii
 1. INTRODUCTION .....	 1
2. OBJECTIVES .....	3
2.1 General Statement .....	3
2.2 Motivation .....	3
3. IONOSPHERIC PLASMA IRREGULARITIES: NATURAL AND ARTIFICIAL MECHANISMS .....	4
3.1 Introduction .....	4
3.2 Current Understanding .....	4
3.2.1 Natural Ionospheric Holes and Equatorial Spread-F .....	4
• Status of Experimental Results .....	4
• Developments in Plasma Instability Analyses .....	8
3.2.2 Ionospheric Modification and Artificial Spread-F .....	9
• Overview .....	9
• The Lagopedo Results .....	11
• Artificial Equatorial Spread-F .....	11
3.3 Deficiencies and the Need for Future Investigations .....	14
3.3.1 Electron Density and Spectral Characteristics .....	14
3.3.2 Electron Temperature and Chemistry .....	14
3.4 Related Programs and LASSII Projections .....	15
4. EXPERIMENTAL APPROACH .....	16
4.1 Overview .....	16
4.2 Scientific Instrumentation and Satellite Configuration .....	17
4.3 Remote Radio and Optical Diagnostics .....	20
5. SPACECRAFT DESCRIPTION AND OPERATIONAL DETAILS .....	21
5.1 Systems Engineering .....	21
5.1.1 Overview .....	21
5.1.2 Subsystem Summaries, Flexibilities, and Growth Potential .....	21
• Electrical Power System .....	21
• Microcomputer Controlled Command and Telemetry System — MICROCATS .....	23
• Attitude Control System .....	24
• Radio Frequency System .....	25
• Thermal Protection System .....	26
• Structures and Mechanisms .....	27

5.2	LASSII Electrical Power System .....	27
5.2.1	Load Requirements .....	28
5.2.2	Electrical Power Systems Description .....	28
	• Solar Array Description .....	28
	• Silver Zinc Battery Description .....	33
	• Nickel Cadmium Battery Description .....	35
	• Battery Charger .....	35
	• Shunt Regulator and Dissipators .....	35
	• 12 Volt Converter .....	35
	• Power Control Unit .....	36
	• Experiment Control Unit .....	36
	• Ordnance Control System .....	36
5.2.3	System Operation .....	37
	• General .....	37
	• Operational Modes .....	38
	• Mission Models .....	38
5.3	MICROCATS — Telemetry and Command System .....	38
5.3.1	Combined Telemetry and Command Subsystem .....	41
	• MICROCATS Functions .....	41
	• Telemetry Control Functions .....	45
	• Command and Control Functions .....	46
5.3.2	Experiment Interfacing .....	47
	• LASSII Experiment Format .....	49
	• User Telemetry Interface .....	49
	• User Command Interface .....	50
	• Serial Digital .....	50
5.3.3	Tape Recording Subsystem .....	50
5.3.4	Attitude Control Computer Interface .....	51
5.4	Attitude Control System .....	52
5.4.1	Requirements .....	52
	• Attitude Control Requirements .....	52
	• Orbit Control Requirements .....	52
	• Tandem Orbit Mission .....	53
	• Continuous Overflight Mission .....	54
5.4.2	ACS Configuration .....	55
5.4.3	ACS Implementation .....	55
5.4.4	Disturbance Analysis .....	59
5.4.5	Angular Momentum Sizing of Reaction and Momentum Wheels .....	60
5.4.6	Thruster Sizing Considerations .....	60
	• Counteractive Thrusting Against Aerodynamic Torque .....	61
	• Large $\Delta V$ Orbit Transfer Maneuvers .....	61
	• Acquisition/Requisition Precession Maneuvers .....	61
	• Retrieval Operations .....	61
5.4.7	Thruster Configuration .....	62
5.4.8	Mission Analysis .....	62
	• Continuous Overflight Mission .....	62
	• Tandem Orbit Mission .....	66
5.5	Radio Frequency (RF) System .....	69
5.5.1	Requirements .....	69
5.5.2	System Implementation .....	71
	• Multiple Access (MA) S-Band Transponder .....	72
	• S-Band Omni Antenna Array .....	72

5.5.3	Link Calculations .....	76
5.5.4	Power Density Considerations .....	80
5.5.5	TDRSS RFI Considerations .....	84
5.6	Thermal Protection System .....	84
5.6.1	Summary .....	86
5.6.2	Technical Discussion .....	88
	• Hot and Cold Orbital Conditions .....	88
	• The Hydrazine System .....	94
	• Electrical Heaters .....	94
	• Thermal Control in the Orbiter .....	94
	• Thermal Control of the Solar Cell Arrays .....	96
5.7	Structural and Mechanical Configuration .....	97
5.8	Product Assurance and Quality Control .....	100
5.8.1	Introduction .....	100
5.8.2	Program Overview .....	101
	• Reliability Analysis Program .....	101
	• Parts Program .....	101
	• Component Procurement Program .....	102
	• In-House Component Processing .....	102
	• System Test Program .....	102
	• Failure Reporting and Analysis .....	102
5.9	Orbital Mechanics Analysis .....	102
5.9.1	Introduction .....	102
5.9.2	Tracking Simulation Results .....	102
5.9.3	Ground Traces .....	104
5.9.4	Conclusions .....	114
5.10	LASSII Computer Systems .....	114
6.	REFERENCES .....	114



**LASSII  
Program Management**

<b>Program Management</b> <b>Dr. E.P. Szuszczewicz</b> <b>E.O. Hulburt Center for Space Research</b> <b>Space Science Division</b> <b>Naval Research Laboratory</b> <b>Washington, DC 20375</b>
--

In Situ Measurement Techniques	Numerical Simulation Techniques	Air Force Science Coordinator	Spacecraft Project Manager	Remote Ionospheric Sensing Techniques
<b>Dr. E.P. Szuszczewicz</b> <b>Ionospheric Diagnostics</b> <b>Section</b>  <b>Naval Research</b> <b>Laboratory</b>	<b>Dr. S.L. Ossakow</b> <b>Plasma Physics</b> <b>Division</b>  <b>Naval Research</b> <b>Laboratory</b>	<b>Dr. R.S. Narcisi</b> <b>Air Force Geophysics</b> <b>Laboratory</b>  <b>Hanscom Air Force</b> <b>Base</b> <b>Bedford, MA 01731</b>	<b>Mr. R.E. Palma</b> <b>Space Systems</b> <b>Division</b>  <b>Naval Research</b> <b>Laboratory</b>	<b>Dr. J.M. Goodman</b>  <b>Ionospheric</b> <b>Effects Branch</b>  <b>Naval Research</b> <b>Laboratory</b>

**PARTICIPANTS IN PLANNING MEETINGS  
AND MISSION DEFINITION**

Aerospace Corporation

Dr. J. Fennell  
Dr. H. Koons  
Dr. C. Rice  
Dr. F. Wang  
Mr. L. Weeks

Air Force Geophysics Laboratory

Dr. J. Aarons  
Dr. S. Basu  
Dr. R. S. Narcisi  
Mr. W. Vickery

Defense Nuclear Agency (DNA)

Lt.Col. R. Bigoni  
Maj. J. Clark  
Dr. H. Fitz, Jr.  
Dr. G. K. Soper

Johns Hopkins University

Dr. J. P. Doering

Johns Hopkins Applied  
Physics Laboratory (APL)

Dr. T. Potemera

National Aeronautics and  
Space Administration (NASA)

Dr. M. Acuna/GSFC  
Dr. R. Goldberg/GSFC

National Oceanographic and  
Atmospheric Association (NOAA)

Dr. B. B. Balsley  
Mr. W. Bernstein (Now at Rice Univ.)

National Science Foundation

Dr. D. Peacock

Naval Electronic Systems Command (NAVELEX)

Dr. F. W. Diederich

Naval Ocean Systems Center (NOSC)

Mr. R. Hopkins  
Mr. M. Paulson  
Dr. I. Rothmuller

Naval Research Laboratory (NRL)

Dr. D. Anderson  
Dr. G. Carruthers  
Dr. J. Fedder  
Dr. J. M. Goodman  
Mr. J. C. Holmes  
Dr. B. E. McDonald  
Dr. R. R. Meier  
Dr. C. Opal  
Dr. S. L. Ossakow  
Mr. R. E. Palma  
Dr. K. Papadopoulos  
Dr. H. Rabin  
Dr. E. P. Szuszcwicz  
Mr. P. G. Wilhelm

Naval Space Systems Activity (NSSA)

LCDR D. Snoddy

Office of Naval Research (ONR)

Mr. G. Joiner

SAMSO/Space Test Program

Maj. C. Jund  
Capt. L. Blackwelder

Stanford University/Radioscience  
Laboratory

Dr. P. Bernhardt (Now at LANL)

TRW

Mr. W. Berks  
Mr. H. F. Meissinger  
Mr. P. E. Romo  
Dr. N. Sanders  
Mr. C. Shreve

University of California at San Diego

Dr. E. C. Whipple

University of Texas at Dallas (UTD)

Dr. W. B. Hanson  
Dr. R. A. Heelis  
Dr. J. P. McClure

# **THE LASSII PROGRAM—OBJECTIVES, SPACECRAFT DESIGN, AND MISSION SCENARIOS FOR FULL-SCALE, SHUTTLE-LAUNCHED, FREE-FLYER OPERATIONS**

## **1. INTRODUCTION**

The LASSII design and overall mission definition is the result of a dynamic evolutionary process which originally considered a dedicated spin stabilized spacecraft in fixed orbit. Detailed reviews of inherent limitations revealed that such an approach could not solve many of the important problems facing the ionospheric research community and systems affected by plasma phenomena in the near-Earth environment. Follow-up studies focused on two fundamental concepts:

1) Short-duration experiments would be more efficient in their concentrated approach to research problems and more likely to provide near-term solutions. Ionospheric research has progressed to a level with less emphasis on the synoptic approach of long-lived satellite investigations. Many requirements now point to specific problem areas covering a wide range of altitudes, latitudes, and solar/geophysical conditions. In addition, the ionosphere can be viewed as a plasma medium to be modified, controlled, and exploited as a natural laboratory for experiments untenable in confining ground-based chambers.

2) Conventional approaches to in situ investigations with rockets and satellites cannot separate space and time variables from their observations, leaving open important questions on uniqueness and applicability of proposed solutions. Increasing interest in ionospheric dynamics, inherent instabilities, plasma turbulence, and associated growth mechanisms require space-time separation to unfold detailed cause-effect relationships and to develop predictive capabilities for naturally occurring or artificially created instabilities.

The advent of Shuttle provides a convenient vehicle for application of the above concepts with unprecedented opportunities for mission flexibility, problem applications, and reduced-cost research and systems development. The resulting study produced a double-spinner spacecraft design to be launched and recovered by Shuttle, and operated in tandem with Shuttle-borne sensors. The double-spinner configuration was found to yield maximum flexibility as an investigative platform, and the tandem operations provided a unique capability for separation of space and time variations in the ionospheric plasma and associated effects on military systems. Design drivers included state-of-the-art plasma instrumentation, battery-only operational capability, stabilized spacecraft potential, Crocco and Hohman maneuverability, the Tracking and Data Relay Satellite System (TDRSS), Shuttle, and direct downlink communications, as well as complete subsystem expansion capability to accommodate new and developing instrumentation and mission requirements. The LASSII sortie-mode free-flyer is viewed as a general purpose vehicle for the conduct of DoD-wide research and development, managed on the basis of an agency-by-agency requirement, and controlled by the Air Force Space Test Program.

*An Overview of Program Operations.* Formation flights of the LASSII free-flyer in conjunction with Shuttle-borne sensor packages (Fig. 1.1) will provide the first capability for the separation of space and time variations in the ionosphere and their effects on command, control, and communication systems. Every advantage will be taken of existing transit and geostationary satellites as well as ground-based diagnostic facilities. A typical mission profile will involve the Shuttle transport of LASSII to orbital altitudes, the launch of LASSII from Shuttle, tandem operations for 1- to 3-week periods, and subsequent

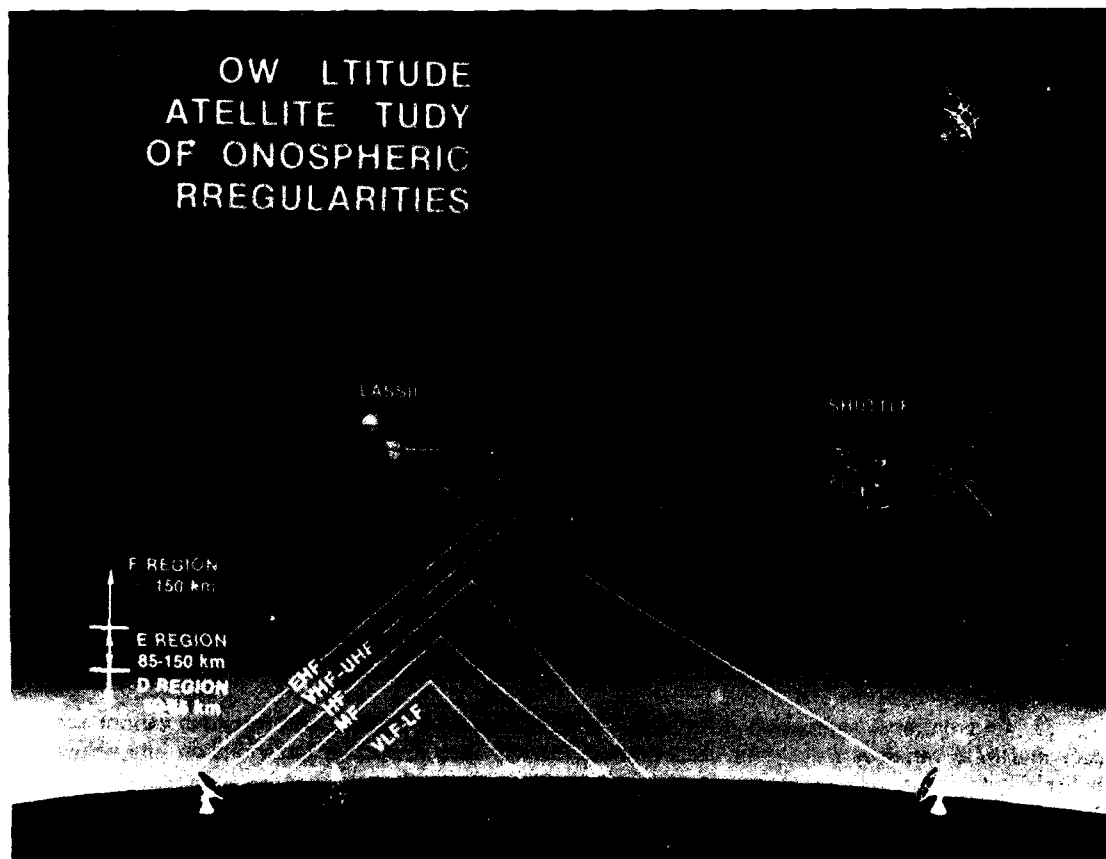


Fig. 1.1 — Tandem and overflight operations of the sortie-mode free-flyer and a Shuttle-borne instrument complement are important elements in mission planning

recovery for recharging and reflight. The recovery and reflight capability will allow mission unique modifications to the payload.

In addition to a multifrequency propagation experiment operating in the electromagnetic wave spectrum from ELF to EHF, the current LASSII free-flyer configuration carries an extensive complement of diagnostic devices which can develop a complete information profile on any ionospheric state and its associated effects on wave propagation. Measurements include: electron density, temperature, and density fluctuation power spectra, ion and neutral composition with associated temperatures and drift velocities, electric and magnetic fields, energetic particles, and photometric and spectrometric diagnostics in the ultraviolet. The complementarity of instrumentation has been designed to encompass areas of basic and applied plasma research and the associated development and test of DoD space networks. The payload subsystems (power, TM, etc.) include a 30% growth capability so that new concepts can be tested within the LASSII mission profile.

As a multiagency, multipurpose mission which is *R<sup>3</sup>* compatible (designed to be Recovered, Recharged, and Reflowed), LASSII allows for an extremely cost-effective and mission-flexible operation, designed to apply the ionospheric technology base for the ultimate benefit of the DoD. Initial efforts will involve naturally occurring ionospheric turbulence with associated experiments in modification and

control by localized chemical releases and beam-plasma interactions. Full advantage will be taken of ground-based diagnostic systems as well as existing transit and geostationary satellites in order to fully determine the effects of the locally perturbed ionosphere on the various signal channels. Reflights will test new and developing techniques for communications and tracking, as well as their survivability in naturally and artificially perturbed ionospheric environments.

## 2. OBJECTIVES

### 2.1 General Statement

There are three coupled objectives identified with the LASSII Mission Plan:

1. The development of a truly predictive capability for the onset of naturally occurring and artificially created ionospheric irregularities and their associated effects on command, control, and communication systems operating in the ELF, VLF, HF, UHF, and EHF domains.
2. The development of techniques for mitigation and/or control of plasma effects in the near-Earth environment through ionospheric modification and/or properly conceived adaptive system design. The ionospheric plasma effects include natural causes (e.g., equatorial spread-F and energetic particle precipitation) or manmade effects (e.g., chemical releases, atmospheric detonations, artificial injection of energetic beams, and nuclear warfare).
3. The development of a facility-class capability for general application to DoD-wide ionospheric research as well as the test and development of military systems affected by geophysical plasma phenomena.

### 2.2 Motivation

Theoretical considerations and various experimental observations indicate that ionospheric irregularities (spatial and temporal variations in ambient electron density) are the cause of many forms of degradation in military systems (e.g., amplitude and phase variations of electromagnetic waves propagating through the ionosphere). These irregularities can occur at all ionospheric altitudes and are known to result from natural as well as artificial causes.

Since the Navy and the entire Department of Defense have billion dollar plans for UHF and EHF satellite systems in communications and navigation, it is important to know the impact of various ionospheric irregularities on such systems. It is already known that scintillations threaten a fail-safe defense posture. For example, studies of TACSAT I have shown that UHF scintillation (i.e., phase and amplitude fluctuations) near 250 MHz exceeded 25 dB peak-to-peak, and faded quite regularly into the system noise; these scintillations greatly exceed nominal power margins of approximately 6 dB and result in 50 to 90% communication outages in the nighttime equatorial sector. Additionally, it is known that engineering solutions like space- and frequency diversity, improved antenna designs, and coding techniques have only provided a few decibels improvement and carry no special hope into the future.

The current technology base has largely been determined by naturally occurring irregularities (equatorial spread-F, auroral phenomena, solar flare effects, etc.) which have reasonably well-defined morphologies. The morphological models, however, have no intrinsic understanding of the cause-effect relationships and consequently provide no predictive capabilities necessary for a fail-safe C<sup>3</sup>I (Command, Control, Communications, and Intelligence) posture. While the LASSII program unfolds the fundamental cause-effect relationships active in the naturally irregular ionosphere, it will apply the developing understanding to active experimentation on ionospheric modification and control. This cou-

pling of peacetime investigations is critical to understanding and controlling ionospheric conditions during communications warfare. Given the current status of atmospheric nuclear test bans, it is evident that we must conduct relevant nonnuclear experiments like those planned for LASSII so that theoretical nuclear predictive capabilities can be validated. It has been demonstrated that natural equatorial spread-F and artificially produced barium clouds provide effective simulators of the nuclear environment. Basically, the systems of equations describing these three environments are the same and produce the same wavelength dependence for the density fluctuation power spectrum, and of course, the associated scintillation effects.

The current picture of geophysical plasma irregularities points to an incomplete knowledge of natural and artificial ionospheric phenomena and their effects on defense systems. History clearly shows an incomplete knowledge of the ionosphere has led to poor system performance and/or engineering changes through retrofitting or costly redesign. The major thrust of LASSII will overcome this problem by providing important ionospheric details as an integral part of pre-system design. Project LASSII will ensure a complete understanding of the ionospheric channel and provide an important theoretical and experimental base for communications warfare as it applies to artificially controlled ionospheric irregularities and nuclear effects.

### **3. IONOSPHERIC PLASMA IRREGULARITIES: NATURAL AND ARTIFICIAL MECHANISMS**

#### **3.1 Introduction**

Accumulating information regarding the near-Earth charged-particle environment has proven it to be a particularly important domain for the communications and ionospheric sciences as well as investigations of fundamental plasma processes that have counterparts in atmospheric releases, beam injections, and controlled laboratory experiments. This wide range of interest has spurred many investigations with major scientific and engineering advances contributing to our current understanding and future plans for adaptive communications system design and ionospheric modification and control.

Rapid advances require occasional synthesis in order to draw proper perspectives and establish an improved definition of near-term and longer range plans. This chapter bears that objective, particularly as it relates to radar, rocket, and satellite studies of the turbulent ionospheric plasma state, the theoretical and computational descriptions, and chemical releases for controlled ionospheric modifications. Although the LASSII effort is designed to address equatorial-, mid-, and high-latitude phenomena as well as controlled experiments at those sights, only low-latitude effects are treated here for purposes of brevity as well as projections of delayed Shuttle launches into polar orbit. We therefore restrict the discussion to important relationships involving spread-F, naturally occurring ionospheric bite-outs, and artificial ionospheric holes. Current understanding is reviewed, deficiencies are identified, and the LASSII/Shuttle role is described.

#### **3.2 Current Understanding**

##### **3.2.1 Natural Ionospheric Holes and Equatorial Spread-F**

###### **Status of Experimental Results**

Since the discovery of equatorial spread F by Booker and Wells [1], considerable observational and theoretical advances have been made in understanding the associated phenomena. (The term "spread-F" stems from the original observations of range and frequency spreading in ionograms.) The advances have been a result of improved "in-situ" measurement techniques, expanded and detailed

ground-based radar observations, and the development of computational techniques that describe candidate plasma instabilities that might be active in the equatorial ionosphere.

The increased activity in the study of the equatorial ionosphere has resulted in modifications in theoretical models as new and improved data have been made available. But as yet there is no completely satisfactory predictive capability for the onset, development, chemistry, and transport of irregularities in the equatorial ionosphere. Even the longstanding morphology of equatorial F-region irregularities has been scrutinized, raising questions of previously unrecognized longitudinal dependence.

The Jicamarca Observatory ( $76.87^{\circ}\text{W}$ ,  $11.95^{\circ}\text{S}$ ;  $1^{\circ}$  dip) near Lima, Peru has provided the most extensive data base for the time and space development of equatorial spread-F. Operating at 50 MHz, the observatory's radar shows reflections from 3-m size ionospheric irregularities as a function of altitude and time. Figure 3.1 shows a typical plot of RTI (Range-Time-Intensity) data collected in the evening during spread-F conditions. The abscissa is time, increasing from early evening on the left to the early morning hours on the right. The figure is used here to summarize salient features of the radar observations that will be coupled to subsequent discussions on chemistry and transport. More detailed discussions on RTI data at Jicamarca are available in the works of Woodman and La Hoz [3], Farley et al. [4], and Calderon [5].

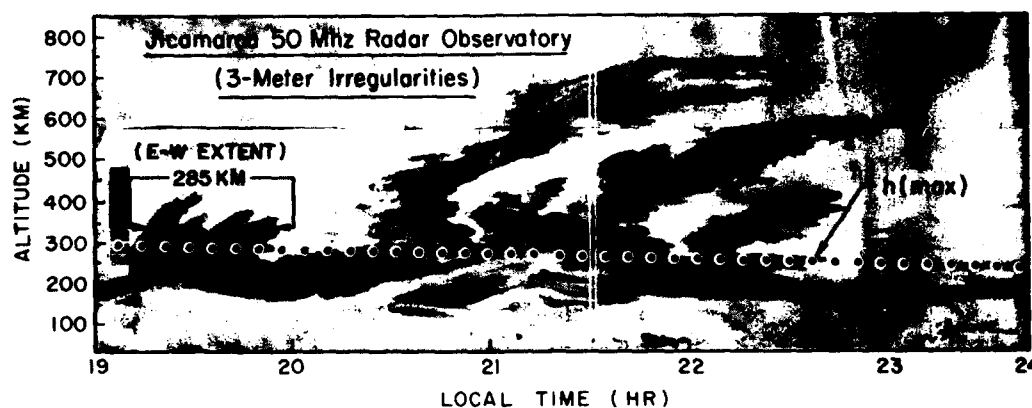


Fig. 3.1 — Range-time-intensity (RTI) plot of backscatter energy at Jicamarca Observatory. Superimposed is the nominal location of the F-layer peak (from Szuszczewicz [2]).

The gray scale shows intensity of radar energy reflected from 3-m scale size irregularities . . . the darker the image, the greater the reflected energy. The dotted line on the RTI plot locates the nominal altitude of the F-layer peak ( $h(\text{max})$ ). The  $h(\text{max})$  line is not the result of actual data collected simultaneously with the RTI plot but represents accumulated information on the postsunset behavior of the laminar ionosphere over Jicamarca (e.g., Farley et al. [6], and Calderon [5]).

The salient features in Figure 3.1 are as follows:

- (a) 3-m size irregularities are fundamentally a bottomside spread-F condition in the early evening hours.
- (b) The irregularities tend to rise and break away from their lower altitude source region. This observation has spawned the use of the terms "bubbles," "plumes," and "fingers" to describe the motion of the irregularity domains.

(c) The irregularities that break away generally move upward, with their intensity decreasing as time moves into the early morning hours.

(d) Bottomside irregularities generally persist throughout the entire period of spread-F conditions. This is not the case for topside irregularities.

Additional conclusions can be drawn from Woodman and La Hoz [3] concerning the relationship between the time axis of the RTI plot and the east-west profile of irregularity structure. They note that since the ionospheric plasma superrotates in an easterly direction at an approximate rate of 125 m/s, a 1-h excursion in time on an RTI plot is equivalent to a 450 km E-W separation. With some qualifications imposed by temporal F-region developments, one can view 1-h segments of any RTI plot as an approximate E-W snapshot of regions of 3-m size irregularities as one looks toward the south. This observation suggests the following conclusions:

- (i) The 3-m size irregularities generated on the bottomside tend to move upward and westward.
- (ii) The east-west extent of the topside irregularity regions are extremely variable with time and altitude. Consider in Fig. 3.1 the early evening horizontal cut at an altitude of 340 km. A properly instrumented satellite or Spacelab payload passing through this region would observe 3-m size irregularities over a 285-km range with substructure down to approximately 10 km.

A synthesis of radar results with the findings of rocket-, satellite-, and ionosonde investigations (Basu et al. [7]; Balsley et al. [8]; Dyson et al. [9]; Hanson et al. [10]; Farley [11]; Kelley and Mozer [12]; McClure and Woodman [13]; McClure and Hanson [14]) (including scintillation observations by Aarons and Allen [15] and Koster [16]) shows that F-region irregularities have latitudinal, diurnal, seasonal, and solar cycle variations with day-to-day perturbations superimposed. Spread-F is essentially a nighttime phenomenon in the equatorial region ( $\pm 20^\circ$  of the magnetic dip equator) with the most intense periods of irregularities occurring within  $2200 \pm 3$  h LT. It appeared at first that the majority of irregularities fell into the "noiselike" structure where the amplitude increased approximately as the irregularity scale size from 70 m to 70 km (Dyson et al. [9]). More recently, however, the works of Brinton et al. [17], McClure et al. [18], Morse et al. [19], and Szuszcwicz [20] indicate that the bite-outs (or holes as they are often referred to) reported by Hanson and Sanatani [21] and McClure and Hanson [14] occur more frequently than was originally thought and in fact are considered just as characteristic of spread-F as the less intense irregularities.

Typically, the ion composition is vastly different inside and outside the bite-outs.  $\text{Fe}^+$  ions may be enhanced or depleted, with molecular ions usually more abundant inside the bite-out. Brinton et al. [17] and McClure et al. [18] have found  $\text{O}^+$  depleted by as much as a factor of  $10^3$  to a concentration below that of  $\text{NO}^+$ . The molecular ion  $\text{NO}^+$  was found to be the dominant ion in the  $\text{O}^+$  depleted region, and it was found that the bite-outs varied from a few kilometers to tens of kilometers in width. A typical satellite observation of equatorial bite-outs is shown in Fig. 3.2.

In the analysis of the data in Fig. 3.2 particular attention was given to possible relationships between ionospheric holes and the smaller scale (3 m) irregularities observed by the Jicamarca radar [20]. Ion chemistry and transport considerations were found to support the concept that equatorial holes and equatorial spread-F could be one and the same phenomenon, with the smaller scale irregularities imbedded within the much larger scale ionospheric depletions. The chemistry and transport model which emerged from the analysis considered a given chemical volume on the bottomside F-layer ( $[\text{NO}^+], [\text{O}_2^+] > [\text{O}^+]$ ) to move upward through a stationary neutral atmosphere and appear at higher altitudes as a bite-out in the local plasma density. As this plasma cell moved upward, the relative magnitudes of its ionic components depended on altitude through the height distribution of the neutral gases.



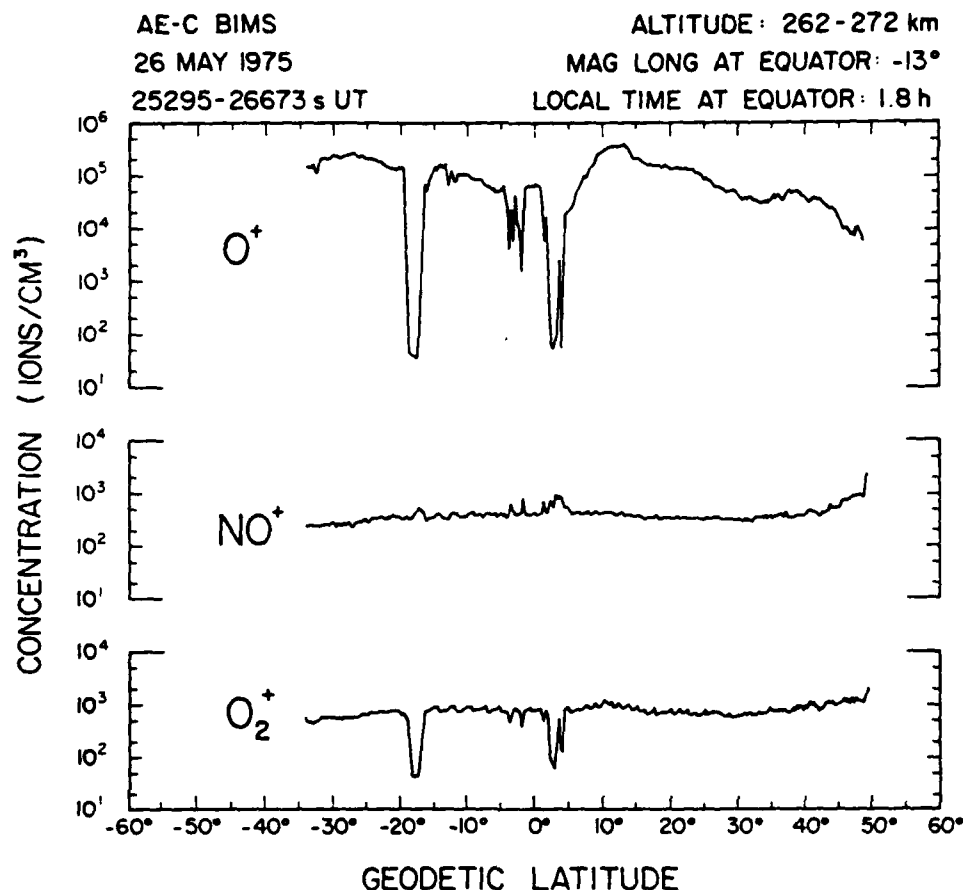


Fig. 3.2 — AE-C Bennett ion mass spectrometer (BIMS) measurement of  $O^+$ ,  $O_2^+$ , and  $NO^+$  in a single equatorial crossing near 265 km (from Szuszczewicz [20])

The concept of an upward moving ionospheric plasma cell is in agreement with the drift velocity measurements of McClure et al. [18]. The concept is also consistent with the computational work of Scannapieco and Ossakow [22], which showed that bottomside F-region irregularities at low plasma densities ( $10^2$  to  $10^4$   $\text{cm}^{-3}$ ) could be transported to more dense ionospheric domains ( $10^5$  to  $10^6$   $\text{cm}^{-3}$ ) and appear as ionospheric holes. The source region can be low enough in the ionosphere to encompass domains of molecular ion domination but cannot be so low as to damp the growth of plasma instabilities necessary to raise it to higher altitudes.

The arguments developed by Szuszczewicz [20], showing a parallel between large-scale ionospheric bite-outs and 3-m size irregularities normally identified with ionospheric spread F, are consistent with earlier observations of  $Fe^+$  at high equatorial altitudes. But the present picture is broader in scope, indicating that  $NO^+$  and  $O_2^+$  in the holes are more likely to be consistent signatures of spread-F since they are characteristic of bottomside composition which can be maintained in first order as it is transported to the topside. The existence of  $Fe^+$  on the topside is likely to be dependent on a two-step process which first requires the transport of metallic ions from the 95-km region to the bottomside of the F-layer as a result of the strong polarization fields which accompany the equatorial electrojet. The continued upward movement of  $Fe^+$  can then be a manifestation of the "fountain effect" as described by

Hanson et al. [23] or a further demonstration of a "frozen" chemical volume of bottom side composition transported to higher altitudes by the Rayleigh-Taylor process (Dungey [24]; Haerendel [25]; Hudson and Kennel [26]; Scannapieco and Ossakow [22]). In this case,  $O^+$  will always be depleted, while the moleculars  $NO^+$  and  $O_2^+$  dominate;  $Fe^+$  will be present only when the E region transport mechanism is actively depositing  $Fe^+$  on the bottomside of the F-layer.

### Developments in Plasma Instability Analyses

The advances in the observational data have been paralleled by developments in theoretical and numerical simulation techniques. The result has been a relatively intensive probe into the fundamental plasma instability mechanisms causing equatorial spread-F.

Serious spread-F plasma analysis had its beginning in linear theories with Dungey [24] being the first to suggest that equatorial spread-F was initiated on the bottomside of the F-layer by the Rayleigh-Taylor instability. In 1957 Dagg [27] proposed that it was due to coupling between the E and F-regions. Two years later, Martyn [28] suggested the  $E \times B$  gradient drift instability and in 1963 Calvert [29] proposed the downward motion of the neutral atmosphere at night as being responsible for equatorial spread-F. (This mechanism was essentially equivalent to the  $E \times B$  description because of the relative motion between ions and neutrals in determining the instability). All of the linear instability mechanisms suffered from a common problem, the inability to explain the formation of irregularities at and above the F-layer peak.

The collisional Rayleigh-Taylor instability with field line averaging was also proposed (Balsley et al. [8]; Haerendel [25]) as a linear instability mechanism. By averaging (integrating) the density along the magnetic field the total electron content profile becomes steeper on the bottomside and its effective peak is raised in altitude with respect to the local electron density peak. This allowed the linear mechanism to operate to slightly higher altitudes ( $\sim 100$  km greater), but still would not explain the existence of irregularities above this "new peak."

Hudson and Kennel [26] pointed out the importance of the collisional drift mode in the wavelength regime 30 to 100 m. This mode could be excited on both the top and bottomside but still would not explain the longer wavelengths. In their paper, finite Larmor radius corrections were also applied to the collisionless and collisional Rayleigh-Taylor instability.

Several nonlinear theories have been invoked to explain the different equatorial spread-F observations. For example Hudson et al. [30] suggested that the smallest scale ( $\leq 10$  m) irregularities (e.g., those seen by coherent radar backscatter) were due to a two-step process. In this prescription a longer wavelength instability sets up the driving conditions for the shorter wavelengths to become unstable. This is similar in spirit to the successful two-step theory (Sudan et al. [31]) proposed for Type II equatorial E-region electrojet irregularities. Haerendel [25] suggested that the range of wavelengths (many kilometers down to meters) exhibited by equatorial spread-F phenomena was due to a multistep process which initially involves the collisional Rayleigh-Taylor (R-T) instability driven by gravity and the zero order electron density gradient scale length on the bottomside. Then the  $E \times B$  gradient drift instability with vertical wave vectors arises due to the large-amplitude horizontal variations set up by the collisional R-T instability. As third and fourth steps the inertial (collisionless) dominated R-T instability takes over, followed by kinetic drift waves which grow upon the irregularities after they reach large amplitude. Like Haerendel [25], Chaturvedi and Kaw [32] also pointed to the unlikely probability that a single instability mechanism could directly excite plasma irregularities over as wide a range of wavelengths as that observed in equatorial spread-F. They suggested a two-step theory in which longer wavelength R-T modes coupled to kinetic collisional drift waves in a manner that resulted in a  $k^{-2}$  irregularity spectrum. (The need for the coupling of various instability processes has proven to be a necessary feature in explaining the full spectrum of phenomena. As another illustration there is the very recent radar observation of 1 m and 36 cm irregularities which motivated a proposed linear theory for

high-frequency drift waves generated by the drift-cyclotron and lower hybrid instabilities (Huba et al. [33]). This theory was set forth as a possible explanation for the occurrence of these irregularities below the ion gyroradius.)

A major breakthrough was made by Scannapieco and Ossakow [22] who performed a nonlinear numerical simulation of the collisional R-T instability. The simulation results showed that the collisional R-T instability generated irregularities and bubbles (plasma density depletions) on the bottomside of the F-region which subsequently rose beyond the F-peak by nonlinear polarization-induced  $E \times B$  forces. This was the first theoretical result to explain how long-wavelength irregularities could appear on both the bottomside and topside of the F-region. The results were in accord with the observations of Kelley et al. [34], McClure et al. [18], Woodman and La Hoz [3], and consistent with the more recent analysis of Szuszcwicz [20]. Ossakow et al. [35] extended the earlier work on nonlinear equatorial spread-F to study the dependence on altitude of the F-peak and the bottomside electron density scale length. They found that under favorable conditions, e.g., high altitude of the F-peak and/or steep bottomside background electron density gradients, the collisional Rayleigh-Taylor instability caused linear growth on the bottomside of the F-region. This in turn caused plasma density depletions or bubbles to be formed on the bottomside which then steepened on their top and rose nonlinearly above the F-layer by polarization (induced)  $E \times B$  motion. This in turn produced irregularities on the topside of the F-layer where a linear analysis would predict no irregularities. High altitude of the F-peak, small bottomside background electron density gradient scale lengths, and large initial bottomside depletions yielded large vertical bubble rise velocities. They specifically showed that changing the altitude of the F-peak from 300 to 430 km can have dramatic effects on the evolution of ESF. One of their simulations is shown in Fig. 3.3.

In parallel efforts Ossakow and his colleagues advanced an analytical nonlinear mode-mode coupling theory for the coherent development of the collisional R-T instability (Chaturvedi and Ossakow [37]). Their theory suggested that vertical modes would be dominant and result in a  $k^{-2}$  power spectrum. Hudson [38] extended the results to the collisionless R-T regime and reached similar conclusions. Analytical models for the rise of collisional and collisionless R-T equatorial spread-F bubbles, in analogy with fluid bubbles, were presented by Ott [39]. At the same time, Ossakow and Chaturvedi [40] presented analytical models for the rise of collisional R-T bubbles within the context of the electrical analogy with barium clouds.

Costa and Kelley [41,42] suggested that coherent steepened structures and not turbulence would give a  $k^{-2}$  power spectrum. Moreover, these sharp gradients could cause small scale sizes ( $\sim 20$  m) by collisionless low-frequency (much less than the ion gyrofrequency,  $\Omega_i$ ) kinetic drift waves via a two-step process. Their analysis was a linear one carried out on a nonlinear state, i.e., one achieves the steepened gradients by nonlinear processes and then one performs linear theory on this state. Kelley and Ott [43] suggested that the equatorial spread-F bubbles, in the collisionless R-T regime, generate a wake with vortices. They then applied two-dimensional fluid turbulence theory to the model. This resulted in the development of turbulence at shorter and longer wavelengths than the bubble size. This in turn led to a prediction of  $k^{-1}$  for the power spectrum (which does not appear to be in agreement with existing experimental observations).

### 3.2.2 Ionospheric Modification and Artificial Spread-F

#### Overview

Within the context of naturally occurring ionospheric holes and their relationship to equatorial spread-F, it becomes a natural scientific extension to test the hypotheses with a controlled experiment. In line with this idea has been a developing interest and technology which has focused on the artificial production of ionospheric holes by injection of chemically reactive species (Barnes [44]; Booker [45]; Bernhardt et al. [46]; Bernhardt [47]; Brown et al. [48]; Jackson et al. [49]; Mendillo et al. [50-52];

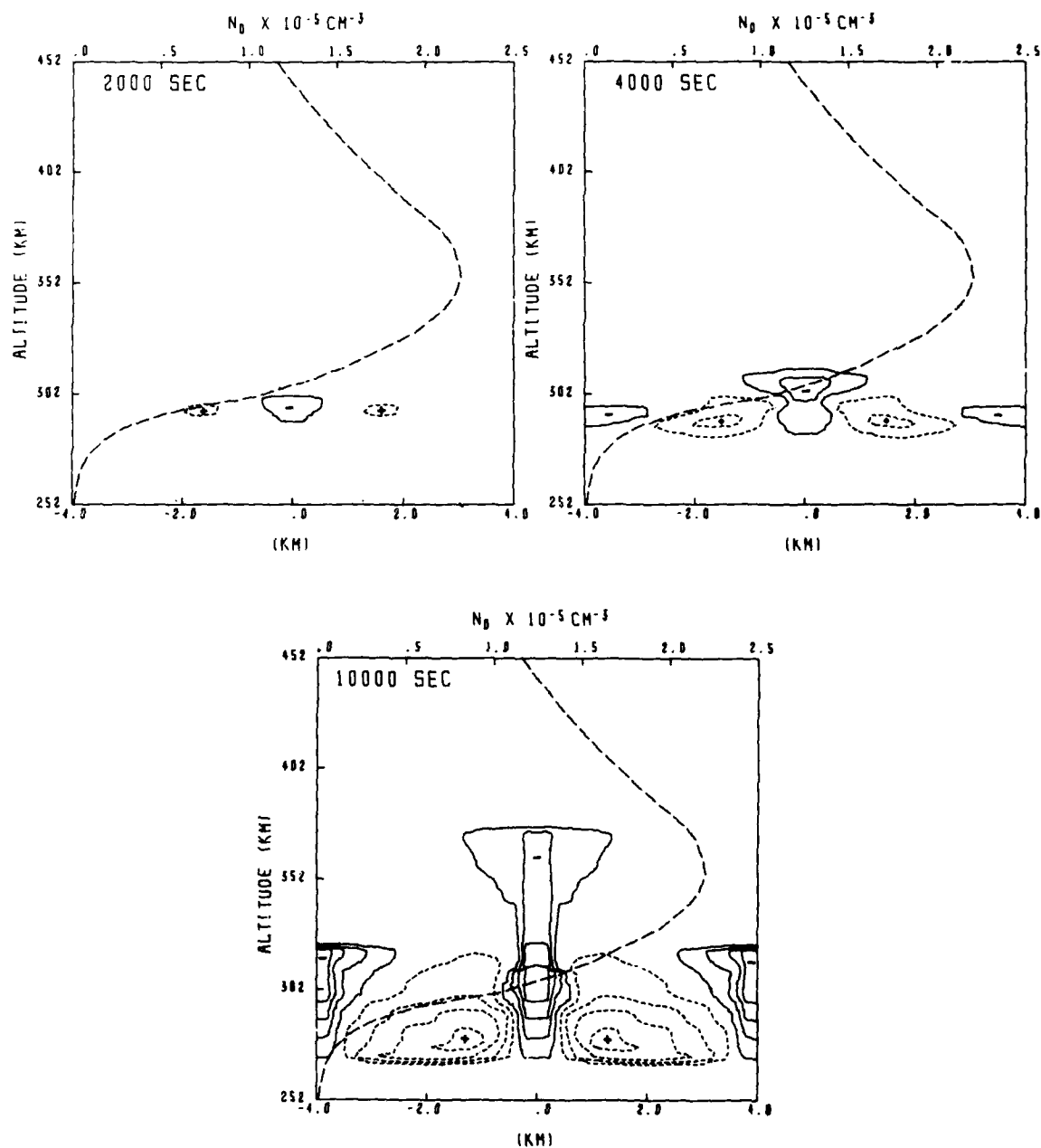


Fig. 3.3 — Contour plots of constant  $n_1/n_0$  for the simulation ESF 1 at  $t = 2000, 4000$ , and  $10,000$  s. The small dashed contours with a plus sign inside and the solid contours with a minus sign inside indicate enhancement and depletions over the ambient electron number density. The large dashed curve depicts the ambient electron number density (values on upper horizontal axis),  $n_0$ , as a function of altitude. The vertical  $y$  axis represents altitude, the lower horizontal  $x$  axis is east-west range, and the ambient magnetic field is along the  $z$ -axis, out of the figure (from Ossakow et al. [36]).

Pongratz et al. [53]; Sjolander et al. [54]; Anderson and Bernhardt [55]). The principle of artificial spread-F involves two questions: (a) Can a substantial ionospheric depletion be artificially produced in a controlled experiment? (b) If such a hole is generated on the bottomside or near the peak of the F-layer, will it rise to higher altitudes and produce irregularity spectra like that of natural equatorial spread-F? The first answer is affirmative, particularly since the recent success of the Lagopedo experiments (Pongratz et al. [53]; Sjolander and Szuszczewicz [56]). The second question has already received theoretical treatment (Ossakow et al. [36]) yielding some very promising results that point to meaningful applications and tests by LASSII/Shuttle operations.

### The Lagopedo Results

Lagopedo I and II were two rocket-borne modification experiments coordinated by the Los Alamos Scientific Laboratory during September 1977 operations at the midlatitude Kauai Test Facility in Hawaii (Pongratz et al. [53]). The Ionospheric Diagnostics Section of the Naval Research Laboratory provided the in situ measurements of the pre- and postinjection ion composition and developed the theoretical code which detailed the dominant modification chemistry (Sjolander et al. [54]; Sjolander and Szuszczewicz [56]). The principle of ionospheric modification involves the release of a chemically reactive gas such as  $H_2$  or  $H_2O$  into an  $O^+$  dominant domain. This enhances the normally slow depletion limiting reactions ( $O^+ + N_2 \rightarrow NO^+ + N$  and  $O^+ + O_2 \rightarrow O_2^+ + O$  with rates in the  $10^{-11}$  to  $10^{-13} \text{ cm}^3\text{s}^{-1}$  range) by introducing a more rapid process of charge exchange (e.g.,  $O^+ + H_2O \rightarrow H_2O^+ + O$  at  $10^{-9} \text{ cm}^3\text{s}^{-1}$ ). The subsequent dissociative recombination of the artificially produced molecular ions results in a charge-depletion process which exceeds that naturally occurring in the  $O^+$  dominant F-region. The Lagopedo experiments employed an 88-kg nitromethane-ammonium nitrate explosive which yielded an injection mixture of  $H_2O$ ,  $CO_2$ , and  $N_2$ . The experimental and theoretical results (solid lines) of Lagopedo II are presented in Fig. 3.4. Points relevant to artificial equatorial spread-F include:

(a) The unequivocal observation of an artificial hole with an approximate radius of 40 km with local depletions ranging from three orders of magnitude in the near-event space-time domain to approximately a factor of 50% near the edges of the injected cloud of gases.

(b) The presence of ion components normally not found in the natural ionosphere (e.g.,  $H_3O^+$ ,  $H_2O^+$ ,  $HCO^+$ ,  $HCO_2^+$ , and  $Al^+$  from disintegration of the explosive cannister). These were products of the injection process and in the application to artificial spread-F could prove themselves as easily identified tracers (Szuszczewicz [20]) if the hole were created on the bottomside and rose to higher altitudes.

### Artificial Equatorial Spread-F

To explore the possibility of artificial spread-F Ossakow et al. [36] developed a simplified model which merged the principles of Lagopedo with previous nonlinear numerical codes. They did not follow the chemical kinetics of the actual time- and space-dependent depletion process, but followed the evolution of the hole after it was produced (assuming time-dependent chemistry was no longer in effect). One of the cases which they considered in their simulations assumed the F-layer at 350 km with a peak background plasma density  $n_o = 2.2 (10^5) \text{ cm}^{-3}$ . Their initial conditions on the hole assumed a constant 97% depletion over a central 30-km domain decreasing to the ambient density over a 20-km extent on each side (total extent of the assumed hole was 70 km). The hole was located on the bottomside gradient at a release altitude of 300 km. The evolution of the bubble and its penetration above the F-layer peak is shown in Fig. 3.5. At  $t = 2000 \text{ s}$  the top of the hole has penetrated the F-peak . . . exhibiting a more rapid rise time than in a natural spread-F hole ( $\sim 8000 \text{ s}$ ) in this same ionospheric density profile (see Fig. 3.3). This happens because a large artificial depletion bypasses the initial linear phase of development.

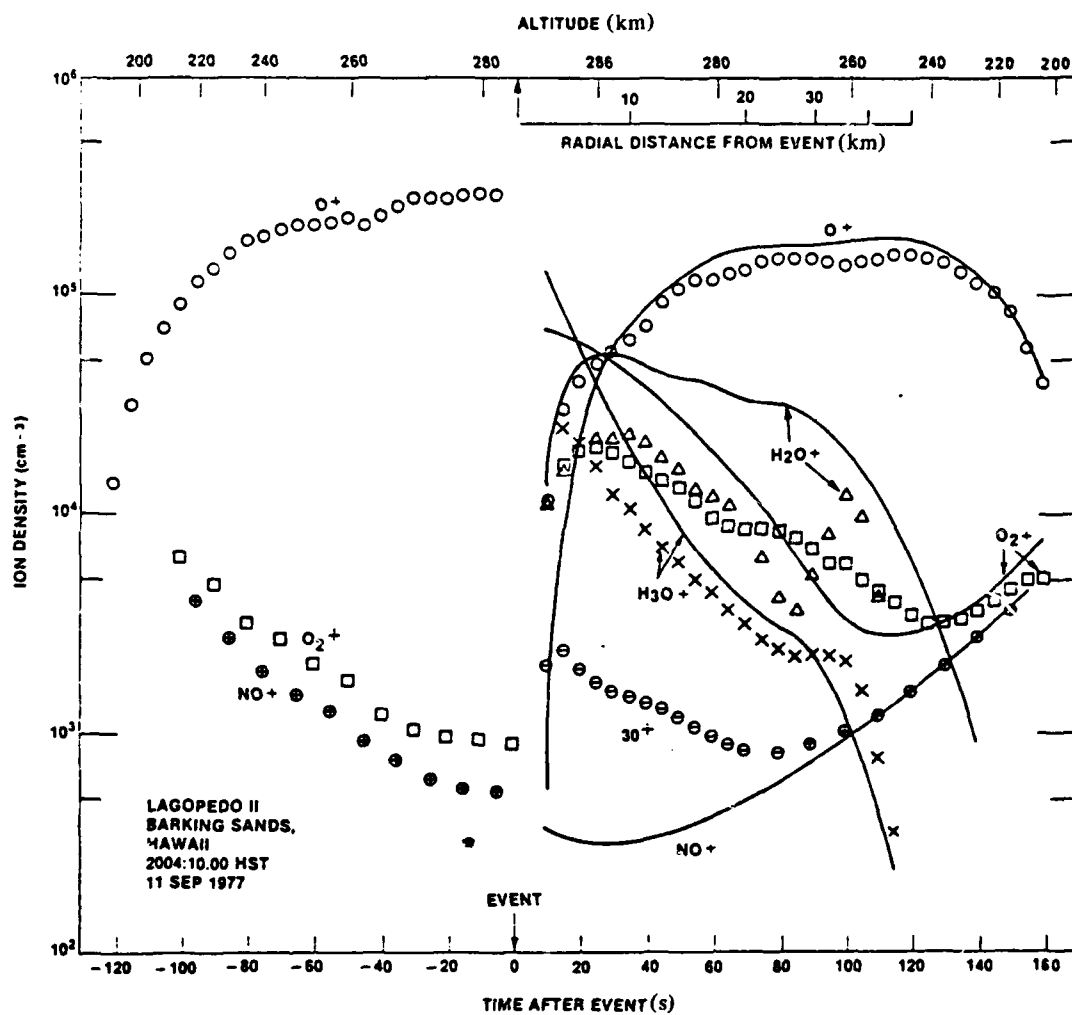


Fig. 3.4 — Lagopedo II rocket-borne mass spectrometer results (symbols) and computer simulation (solid lines). The data are presented as a function of time and radial distance (see inset at top of figure) relative to the event (i.e.  $t \equiv 0$  for explosive detonation). Rocket altitude is presented on the top abscissa (from Sjolander and Suszczewicz [56]).

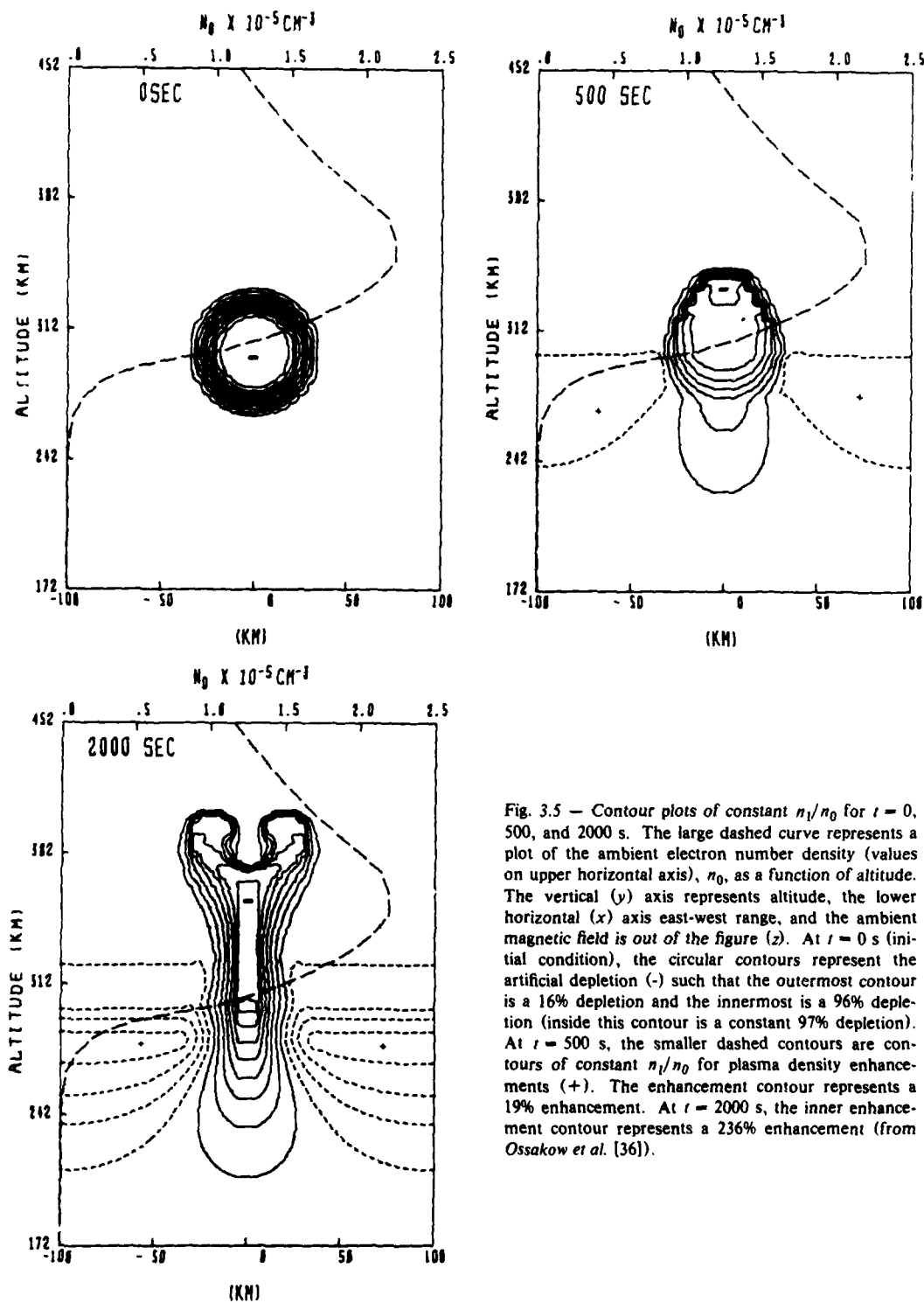


Fig. 3.5 — Contour plots of constant  $n_1/n_0$  for  $t = 0$ , 500, and 2000 s. The large dashed curve represents a plot of the ambient electron number density (values on upper horizontal axis),  $n_0$ , as a function of altitude. The vertical ( $y$ ) axis represents altitude, the lower horizontal ( $x$ ) axis east-west range, and the ambient magnetic field is out of the figure ( $z$ ). At  $t = 0$  s (initial condition), the circular contours represent the artificial depletion (-) such that the outermost contour is a 16% depletion and the innermost is a 96% depletion (inside this contour is a constant 97% depletion). At  $t = 500$  s, the smaller dashed contours are contours of constant  $n_1/n_0$  for plasma density enhancements (+). The enhancement contour represents a 19% enhancement. At  $t = 2000$  s, the inner enhancement contour represents a 236% enhancement (from Ossakow et al. [36]).

These results and others in the same work point to the potentially successful application of chemical modification to artificial triggering of equatorial spread-F.

### 3.3 Deficiencies and the Need for Future Investigations

#### 3.3.1. *Electron Density and Spectral Characteristics*

Although much progress has been made in understanding equatorial spread-F phenomena, more detailed work needs to be done on the fundamental plasma process in order to definitively unfold the active first principles and their coupling to the natural ionosphere. For example, we have yet to obtain the electron density fluctuation power spectrum over the broad domain encompassed by equatorial spread-F. The preceding sections clearly point to the importance of these measurements as a first approach in understanding the multistep plasma processes in which large-scale irregularities (kilometers) cascade to much smaller dimensions ( $< 3$  m). In this regard there has been only one satellite investigation (Dyson et al. [9]) which attempted to define the irregularity spectra and associated causal mechanisms. The data come from the OGO-6 retarding potential analyzer operating at altitudes above 460 km at an orbital inclination of  $82^\circ$ . With the instrument limited to scale sizes greater than 70 m, the most common feature at all latitudes appeared to be an irregularity spectrum with amplitude structure increasing approximately as the scale size. Departures from this power law spectral behavior were classified as "sinusoidal" or "ground glass" irregularities and tentatively identified as different phases of the (unknown) process responsible for the power law dependence. The work of Dyson et al. [9], along with the cataloging efforts of McClure and Hanson [14], represents one of the most important experimental steps. From here higher resolution correlative plasma measurements must be made in high- and low-inclination orbits in order to establish the degree of isotropy in the irregularity spectra perpendicular and parallel to the geomagnetic field. The definition of spectral characteristics needs to be extended down to sizes  $\leq 3$  m and must be studied within the context of positions relative to the F-layer peak and any superimposed ionospheric depletions. These measurements must also be extended into the domain of time correlation in order to study the variations of spectral distributions that are expected to take place during the development of the multistep plasma instability processes.

#### 3.3.2 *Electron Temperature and Chemistry*

The need for extended studies of electron density fluctuation power spectra cannot stand alone in determining all the causal mechanisms. The existing data show that any study of equatorial irregularities must determine the degree of balance between the chemistry and the dynamics of the ionosphere. Here the electron energy plays a critical role in the dissociative and radiative recombination processes (Biondi [57,58]; Lindinger et al. [59]; Oppenheimer et al. [60]; Torr et al. [61]; Oppenheimer et al. [62]). The impact of  $T_e$  on chemistry, coupled with the fact that  $T_e$  controls the short wavelength cutoff in the linear development of ionospheric fluid-type plasma instabilities (Ossakow [63]), establishes the measurement of electron temperature as important to a full understanding of spread-F irregularities and equatorial bite-outs.

The  $T_e$  measurements must be made inside and outside of the ionospheric holes, as well as across the sharp boundaries that are a characteristic feature of many of the depleted domains. The measurement capability must clearly extend to rapidly changing density environments and into domains where contaminating species (e.g.,  $H_2O$  in a modification experiment) can seriously degrade the measurement integrity (Holmes and Szuszczeicz [64]; Szuszczeicz and Holmes [65]). The electron temperature must be determined in F-region chemical release experiments, particularly in the daytime ionosphere where the electron gas can be heated by as much as a factor of two in the presence of an artificially depleted ion population (Bernhardt [47]). The  $T_e$  measurement should be done simultaneously with the measurement of electron density fluctuation power spectra in order to determine the role of electron energy in the naturally occurring instability processes as well as those that might be triggered by chemical releases.



### 3.4 Related Programs and LASSII Projections

In an effort to close the gap between macroscopic phenomenology and detailed understanding of causal mechanisms, the Naval Research Laboratory is participating in a number of programs specifically designed for the development of predictive capabilities for the naturally and artificially triggered onset of ionospheric irregularities. In many cases these programs involve cooperative efforts with other agencies. Near-term contributors in this category include the DNA/Kwajalein campaign of August 1979, the F-region polar orbiting STP satellite S3-4, and laboratory simulations of beam-plasma interactions for applications to beam injection experiments at ionospheric altitudes.

The DNA effort involved two rockets instrumented with high-resolution plasma probes, electric field sensors, a mass spectrometer, and a VHF-UHF beacon experiment. The rocket launches were timed for penetration of equatorial spread-F plumes, and the in situ diagnostics were coupled with the ground-based measurements of radar, ionosonde, and neutral winds. The results (Keskinen et al. [73]; Narcisi and Szuszczewicz [74]; and Tsunoda [75]) have advanced the understanding of naturally occurring spread-F and have strengthened the interpretations presented in this document.

The STP/S3-4 satellite (launched March 1978) included a pair of precision plasma probes which provided direct measurements of the ionospheric state, its condition of irregularity, and the associated electron density fluctuation power spectra. This experiment is providing the first satellite opportunity to assemble power-law information to wavelengths as small as 19 m and to compare the results with the Kwajalein/Altair radar observations. In addition, the experiment has operational modes which test the roles of electron energy and ion composition in the distribution of wave energy in the cascading process of large- to small-scale ionospheric plasma irregularities (Szuszczewicz et al. [76]; Singh et al. [77]; and Rodriguez et al. [78]).

The work on beam-plasma interactions has been stimulated by considerations bearing on vehicle neutralization during spaceborne accelerator experiments, enhanced beam-plasma ionization processes, and in general, collective phenomena initiated by beam injection into neutral gas and charged-particle environments. With plans for experiments directed at controlled beam-plasma interactions and the use of beams to probe ionospheric/magnetospheric electric and magnetic fields, it became important to conduct laboratory simulations which supported the LASSII plans and helped establish definitive Shuttle-borne experiments. As part of just such a plan involving a continuing investigation of large-facility beam-plasma interactions (Bernstein et al. [66-68]), the Naval Research Laboratory has been participating in a series of experiments at the NASA Johnson Space Center. The NRL contribution involves the direct measurement of electron density, temperature, and density fluctuation power spectra under varying conditions of beam-plasma and neutral gas parameters. Some of the initial work (Szuszczewicz [69]), under conditions intended to simulate Shuttle- and LASSII-borne beam-plasma investigations, has uncovered a diffusion process orders of magnitude larger than would be expected from cross-field collisional diffusion . . . a result identified with the turbulent state of collective beam-plasma interactions. Continued investigations will help determine beam-induced modifications in the ambient plasma, the distortion of single particle phenomena by collective plasma effects, and the total energy deposited by the beam in the ambient neutral and charged-particle environment (Bernstein et al. [79]; Jost et al. [80]; and Szuszczewicz et al. [81]).

The accumulating information will become part of a dynamic LASSII investigative plan which focuses on formation flights of the sortie-mode free-flyer with Orbiter-borne sensor packages. The tandem operations will explore and exploit natural and artificial controls of ionospheric plasma while providing the first capability for the separation of space and time variations in the ionosphere and their effects on transionospheric communications. Initial efforts will address specific issues involving fundamental causal mechanisms. Among these issues are:

- (a) The relationship between very small scale irregularities ( $\leq 1$  m) and the longer wavelength fluid type perturbations;

- (b) The effects of zero-order ionospheric plasma conditions including location and intensity of the F-layer peak, the scale size of the bottomside gradient, and ion inertia;
- (c) The equatorial spread-F bubble decay process and the role of plasma diffusion perpendicular and parallel to the geomagnetic field;
- (d) Irregularity spectral characteristics as a function of space, time (in the instability growth sequence), and F-layer parameters . . . particularly as they correlate in space relative to ambient depletions (i.e., What are the spectral indices within the hole, across its boundaries, and in the nearby domains?);
- (e) The degree of degradation of communication channels as a function of irregularity spectral indices, particularly as it might be controlled by artificial means;
- (f) The transport of bottomside F region plasma cells (both natural and artificial) to higher altitudes and the variations in initial characteristics (e.g.,  $N_e$ ,  $T_e$ , and  $M_f$ ) as the cell penetrates the F-layer peak and appears on the topside;
- (g) Beam-injection characteristics and the relationships to ambient plasma conditions and spacecraft charging; and
- (h) Various modes of beam-plasma interactions, including transitions from single-particle interactions to collective plasma processes and their roles in triggered ionospheric turbulence, ionospheric/magnetospheric probing, artificial aurora, and beam weaponry.

By no means is the list intended to be comprehensive but rather to be representative of the issues currently faced by geophysical plasma science and affected military systems.

## 4. EXPERIMENTAL APPROACH

### 4.1 Overview

An overview of the experimental approach is presented here in order to establish the general plan for achieving the LASSII mission objectives. Some details have already been presented in preceding chapters while the specifics of operations, mission scenarios, and spacecraft design are reserved for Chapter 5.

The experimental concept is simple, but fundamentally different from that of any past or present satellite mission: to employ a sortie-mode free-flying satellite which is launched and recovered by Shuttle, and instrumented with a complement of plasma diagnostic tools which have been specifically designed to spatially and temporally resolve all the active elements within an ionospheric irregularity. The satellite, configured for maximum flexibility as an investigative platform, will co-orbit in tandem or in overflight with a Shuttle-borne plasma diagnostics complement, making possible separation of space and time dependencies and allowing important determinations of growth and transport mechanisms in turbulent ionospheric plasmas. The satellite will be able to execute Hohmann and Crocco maneuvers with complete flexibility for selection of time spacing between Shuttle-borne and LASSII free-flyer measurements of a given ionospheric volume.

The uniqueness of the LASSII Mission makes it compatible with all Shuttle orbits from 200 to 1000 km and for all inclinations. The nature of the program, with emphasis on naturally occurring as well as artificially produced ionospheric irregularities, is also easily accommodated by Shuttle regardless of season or solar conditions. Program planning will focus on short-duration (7 to 30 days) experi-

ments which will take advantage of built-in flexibility in the LASSII payload complement. The experiment duration will help develop efficiency through a concentrated approach to research problems designed to provide near-term solutions to issues of immediate military concern.

## 4.2 Scientific Instrumentation and Satellite Configuration

The double-spinner spacecraft design was selected in order to accommodate simultaneous requirements for scan and fixed-position diagnostics. The spacecraft (see Fig. 4-1) consists of a central 3-axis stabilized section (stator) and a symmetric double-ended spin platform (rotor). The stator contains the high-demand space-time resolution plasma instrumentation, most of which are mounted on one of its surfaces to be held within  $1^\circ$  of ram. The rotor consists of two major elements, a solar array section and scanning instrumentation.

The scientific instrumentation and associated measurements are listed in Table 4-1. Mounted to the stator section are two pulsed-plasma-probes ( $P^3$ ), a quadrupole ion mass spectrometer (QIMS), an ion drift meter (IDM), a retarding potential analyzer (RPA), a cold cathode ion gauge (CCIG), the far ultraviolet spectrograph (FUVS), four-frequency radio propagation (FFRP) instrumentation, and the three-axes fluxgate magnetometer (B-FIELD).

From a plasma diagnostics point of view the stator instrument complement will provide a comprehensive measurement set which will define the ambient thermal plasma state. The  $P^3$  technique is particularly well suited for in situ investigations of ionospheric irregularities because it can measure electron densities and energy distribution functions under fluctuating plasma conditions. To this capability the  $P^3$  experiment adds a simultaneous measurement of the density fluctuation power spectrum, providing an important link between plasma instabilities, the resulting irregularities, and associated scintillation phenomena. The QIMS, IDM, and RPA represent state-of-the-art instrumentation with the highest available measurement capabilities for determinations of ion composition, density, drift velocity, and temperature. The CCIG provides coordinated measurements of neutral density and neutral density fluctuations while the FUVS and FFRP establish remote sensing capabilities for  $O^+$  and  $N_e$  variations through UV imaging and measurements of Faraday rotation, dispersive doppler, and associated intensity scintillation power spectrum.

From the  $P^3$ , RPA, and QIMS experiments will come independent measurements of the density fluctuation power spectra  $P_n(k)$ . This parameter provides information on the nonlinear saturated state of the instabilities responsible for the irregularities and thus can be compared directly with density fluctuation power spectrum predicted by numerical simulations. In addition, there are important cases for which a simple relationship exists between the measured in situ density fluctuation power spectrum  $P_n(k)$  and the intensity scintillation power spectrum  $P_s(k)$  determined by the FFRP experiment. Thus a direct test is provided for a correlation between a measured irregularity and a perturbation of a propagating radio wave.

The cooperative theoretical and experimental programs will probe still further. The electron density and electric and magnetic field fluctuation measurements ( $P^3$ , E-FIELD, and B-FIELD, respectively) will identify the electrostatic and electromagnetic natures of the various ionospheric irregularities and will provide the basic data needed to test the existence of candidate instability mechanisms. The measurements of electron and ion temperature ( $P^3$  and RPA) are important to the thermal equilibrium of the unstable state while the ion density, temperature, and degree of turbulence influence the role of diffusion in an instability. The distribution in space and time of ionic species (QIMS), neutral densities (CCIG), and neutral composition (NAMS) will confirm or deny the influence of heavy particles or otherwise unexpected concentrations on irregularity development, and will test the uniqueness of time-dependent chemical codes in experiments employing artificial chemical injection. In addition, the knowledge of ion composition serves to identify artificial tracer elements and evaluate the role that gravitation might play in the generation or irregularities. Furthermore, the density, temperature, and

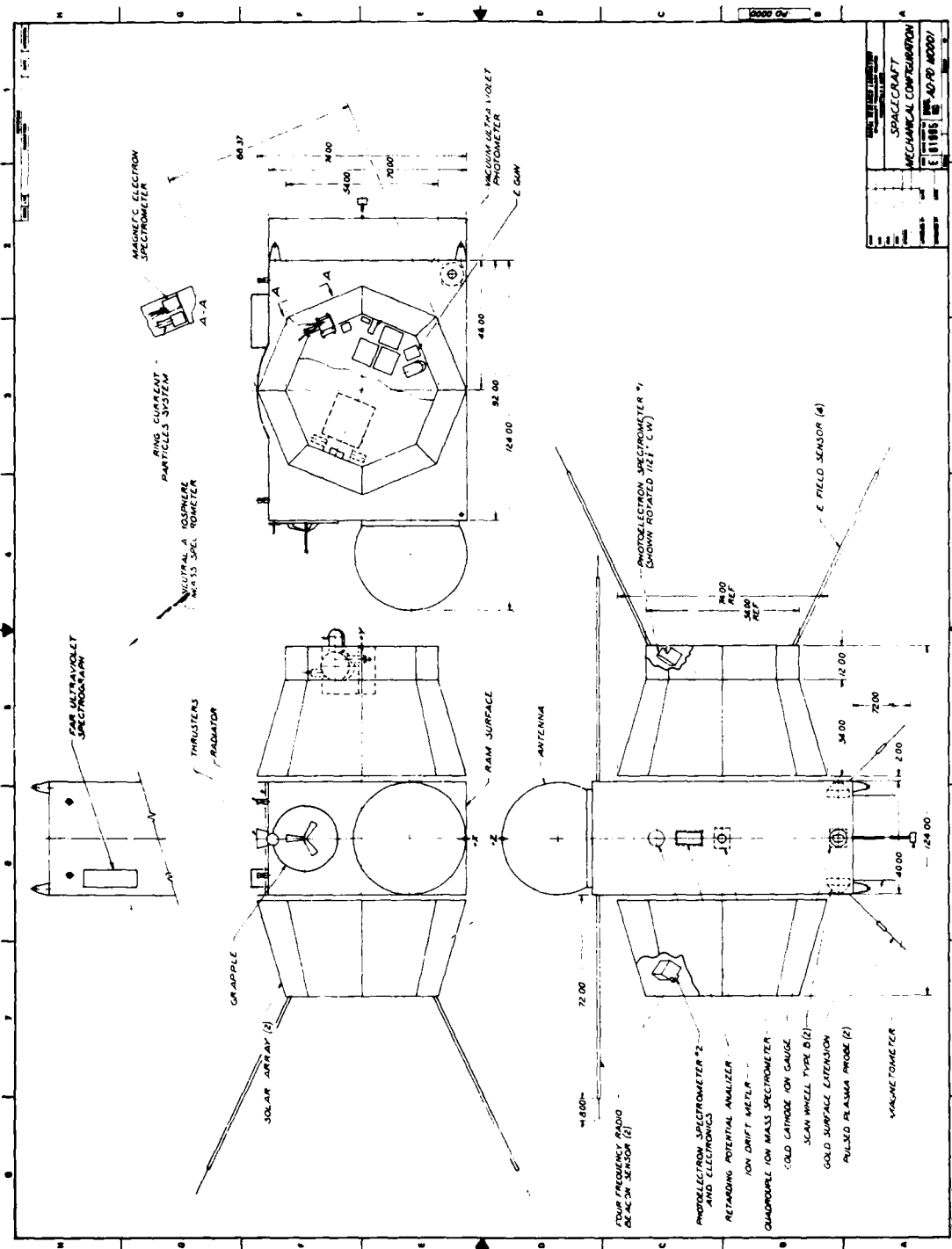


Fig. 4.1 — The Interim LASSII spacecraft configuration

Table 4.1 — LASSII Instruments

	Instrument	Measured Parameters	
		Primary	Secondary
STATOR	P <sup>3</sup> Pulsed Plasma Probe (1 pair of probes) Exp. 4	-Electron temperature, $T_e$ -Electron density, $N_e$ -Density fluctuations, $\delta N_e/N_e$ -Fluctuation power spectra, $P_n(k)$	-Mean ion mass fluctuations, $\delta \bar{m}_i/\bar{m}_i$ -Plasma potential
	QIMS Quadrupole Ion Mass Spectrometer Exp. 7	-Ion composition, $N_i(m_i)$	-Ion density fluctuations, $\delta n_i$
	IDM Ion Drift Meter Exp. 8	-Transverse ion drift velocities, $V_i^v, V_i^h$	
	RPA Retarding Potential Analyzer Exp. 9	-Ram ion drift velocity, $V_i^R$ -Ion temperature, $T_i$ -Ion density, $N_i$	-Mean ion mass, $\bar{m}_i$ -Ion density fluctuations, $\delta N_i/N_i$
	CCIG Cold Cathode Ion Gauge Exp. 10	-Neutral gas density, $\rho$ -Neutral density fluctuations, $\delta \rho/\rho$	
	FLVVS Far Ultraviolet Spectrograph Exp. 1	-FUV radiation spectra, 300-1400 300-2000	-Remote sensing of $[O^+], [N^+]$
	FFRP Four Frequency Radio Propagation Exp. 3	-Phase and amplitude scintillation -Total electron content -Wave emissions and channel characteristics	-Remote sensing of ionospheric irregularities
	B-Field Three-Axis Fluxgate Magnetometer Exp. 15	-Magnetic field, $\vec{B}$	
ROTOR	E-FIELD Exp. 5	-Electric fields, $E$	
	MES Magnetic Electron Spectrometer Exp. 11	-Energetic electrons, $N_e (0.46 \leq E_e \text{ (keV)} \leq 400)$ -Energetic protons, $N_H^+(E_H^+ > 50 \text{ keV})$	-Energetic neutrals and heavy ions $N_{n,i} (25 < E < 50 \text{ keV})$ $N$
	RCPS Ring Current Particle Spectrometer Exp. 12	-Energetic ions, $N_i (25 \leq E_i \text{ (keV)} \leq 8000)$	-Energetic electrons $N_e (50 < E_e \text{ (keV)} < 500)$
	NAMS Neutral Atmosphere Mass Spectrometer Exp. 6	-Neutral atmospheric composition, $N_n(M_n)$ -Neutral temperature, $T_n$ -Neutral winds, $V_n$	
	E-GUN Electron Gun Exp. 14	-Electron beam, $E_e < 2 \text{ keV}$ $I_e < 0.5 \text{ A}$	
	LEPD Low Energy Particle Detectors Exp. 13	-Electron energy distribution, $1 \leq E_e \text{ (ev)} \leq 500$	
	VUVP Vacuum Ultraviolet Photometer Exp. 2	-VUV radiation, 1325-1600 Å	- $[O^+]$ morphology -Photoelectron flux, $O^+ (1256 \text{ Å})$ $N_2 \text{ (LBH)}$
	UVI UV Imagery/Shuttle Attached	-UV images in 1050-1600 and 1250-2000 Å regions	-Particle induced emissions -Gas releases
ORBITER	FFRP Four Frequency Radio Propagation	-Phase and amplitude scintillation -Total electron content -Wave emissions and channel characteristics	-Remote sensing of ionospheric irregularities
	P <sup>3</sup> Pulsed Plasma Probe (1 pair of probes)	-Electron temperature, $T_e$ -Electron density, $N_e$ -Density Fluctuations, $\delta N_e/N_e$ -Fluctuation power spectra, $P_n(k)$	-Mean ion mass fluctuations, $\delta \bar{m}_i/\bar{m}_i$
	QIMS Quadrupole Ion Mass Spectrometer	-Ion composition, $N_i(m_i)$	-Ion density fluctuations, $\delta n_i$

vertical ion drift measurements (RPA and IDM) are capable of identifying large-scale plasma outflow, the polar wind, or inflow along the geomagnetic field at latitudes above the plasmapause boundary. Along with the determination of suprathermal electron fluxes (LEPD, MES, and RCPS), ultraviolet emissions (FUVS and VUVP), and measurements of ambient electron densities and temperatures ( $P^3$ ) comes the capability for evaluating the effects of SAR arcs on ionospheric irregularities.

The two vacuum ultraviolet instruments on LASSII (VUVP and FUVS) and the UV imaging cameras attached to the Shuttle will provide a means for remote sensing of ionospheric composition and electron temperature as a complement to the in situ measurements. In particular, these instruments provide measurements of total column density over a long path in the ionosphere, which, when correlated with local densities measured by other instruments, can provide information on the spatial extent of the ionized and/or depleted regions, and the spatial distribution of ion density in three dimensions. The variation in one dimension (the direction of travel of the spacecraft) can be determined by in situ measurements, but the variations in the other two dimensions can be provided by the FFRP and by remote-sensing UV measurements scanning in the plane perpendicular to the velocity vector.

The VUV photometer will provide remote sensing of the nighttime  $O^+$  concentrations by monitoring the 1356 Å emission of neutral oxygen produced in the electron recombination of  $O^+$ . The intensity of this emission is proportional to the concentrations of  $O^+$  and electrons (or the square of the  $O^+$  density if  $O^+$  is the dominant ion species); it also is proportional to the path length (for a given local  $O^+$  concentration). On the dayside, the VUV photometer will provide measurements of photoelectron fluxes and energies from observations of the Lyman-Birge-Hopfield (LBH) emission bands of  $N_2$  which are excited in the day glow by the photoelectrons. On the dayside, the 1356 Å emission of oxygen is primarily due to photoelectron excitation of neutral oxygen, rather than to  $O^+$  recombination, so measurements at this wavelength are indicative of neutral O concentrations.

The FUV spectrograph will provide line-of-sight measurements of  $O^+$  and  $N^+$  concentrations on the dayside by observations of their resonance emissions at 834 Å (along with O II 539 Å and 617 Å in second order) and 1085 Å, respectively. FUVS capabilities also include observations of neutral species like H, N, O, and  $N_2$ . As in the case of VUV photometer, the FUVS measurements will supplement the in-situ mass spectrometer measurements in providing information on total column densities over very long path lengths. The VUV spectrograph will also be a valuable diagnostic tool in the study of phenomena associated with chemical releases and with electron beam impact with the upper atmosphere.

Finally, the electron gun (E-Gun) and the entire LASSII diagnostics complement will play a vital role in a large number of investigations involving beam-plasma interactions. Special attention will be given to considerations bearing on vehicle neutralization, spacecraft charging, enhanced beam-plasma ionization processes, collective phenomena initiated by beam injection into neutral gas and charged particle environments, and the use of beams to probe ionospheric/magnetospheric electric and magnetic fields.

#### 4.3 Remote Radio and Optical Diagnostics

The LASSII program will take full advantage of ground-based diagnostic systems as well as transit and geostationary satellites in order to augment the in situ measurements with remote and line-of-sight integrated sensing capabilities and to fully determine the effects of the locally perturbed ionosphere on the various signal channels. Included in this area of sensors are ionosondes, coherent and incoherent radars, HF through EHF receivers, and all sky photometric imaging systems.

The ionosonde and incoherent radars will measure local time variations in the height and density of the F-layer peak as well as macroscale variations in horizontal electric fields. Incoherent radar and

amplitude and phase scintillation measurements will provide long-baseline time scaling of local ionospheric turbulence. In this regard the FFRP experiment will determine the horizontal scale and amplitude of ionospheric inhomogeneities, thus providing excellent corroborative information for the in situ experiments. The FFRP experiment has been specifically designed so that both Faraday rotation and dispersive doppler techniques may be employed to measure ionospheric inhomogeneities in the LASSII-to-Shuttle or LASSII-to-ground link.

The ground-based photometric imaging system will employ the techniques of the USAF/AFGL program to monitor the development, structure, and motion of F-region irregularities leading to scintillations of satellite signals. The imaging system will provide all-sky pictures of the 6300 Å OI airglow emission resulting from dissociative recombination of  $O_2^+$  in the F-region. This technique will provide minute-by-minute images of the large-scale structure of the bottomside F-layer, and hence will be an important corroborative tool in studying instability growth and decay mechanisms and establish important north-south/east-west morphologies.

## 5. SPACECRAFT DESCRIPTION AND OPERATIONAL DETAILS

### 5.1 Systems Engineering

#### 5.1.1 Overview

The preceding chapters have dealt with the fundamentals of the LASSII concept with the mission objectives, the experiment complement, and projected efforts all having been detailed. This chapter deals with the engineering subsystems which contribute to the sortie-mode free-flyer design (Fig. 4.1) and the overall program implementation. Specifically, Section 5.1 constitutes a spacecraft systems' capabilities summary. The top-level specifications and capabilities are condensed for each major subsystem. In addition, the inherent flexibility of the particular subsystem to adapt to changing support requirements is brought out. Although the subsystems were designed to current LASSII mission requirements, Section 5.1 can be used to gain an understanding of the "general purpose engineering platform" capabilities alone, as might be appropriate for guest investigations and mission expansion. In general, the subsystem sections (5.2 through 5.9) contain more detailed information than the summaries in Section 5.1.2.\*

#### 5.1.2 Subsystem Summaries, Flexibilities, and Growth Potential

##### Electrical Power System

The electrical power system consists of high-capacity nonrechargeable silver-zinc batteries supplemented by a relatively low-power solar array. The silver zinc batteries provide inherent bus voltage regulation over a wide range of loads. The solar array is shunt limited, maintaining the voltage regulation during load fluctuations, and permitting smooth transfer from full solar array support of the loads to sharing with batteries to full battery-supplied power. A small, nickel cadmium battery and charger are incorporated to afford, in conjunction with the solar array, a low-power survival capability should the silver zinc batteries near depletion.

A Power Control Unit (PCU) contains the switching and power distribution system for the power system and other engineering and service loads. The scientific experiment loads are interfaced in the Experiment Control Unit (ECU) which provides buffering and fault unloading isolation between the

\*The product assurance (5.8) and orbital mechanics (5.9) sections are not summarized in 5.1.2.

## SZUSZCZEWICZ AND PALMA

experiments and the power system, as well as switching and special conditioning. In addition to regulated bus power, both the PCU and ECU switch  $\pm 12$  V regulated power to experiment and housekeeping instrumentation loads.

Ordnance functions are fully redundant and contained in a package that provides power conditioning, logic, interlocks, and switching of pyrotechnics.

### Power System Characteristics

Normal Bus Voltage	27.5 $\pm$ 1.5 V dc
Survival Bus Voltage	25 $\pm$ 4 V dc
Max Power Capability	820 W @ 27 V
Energy Storage	
Two Silver-Zinc Batteries	30 780 Wh mass: 196 kg (432 lb)
Reserve	10 260 Wh
Three Silver Zinc Batteries	46 170 Wh mass: 294 kg (648 lb)
Reserve	15 390 Wh
One Nickel Cadmium (Survival) Battery	270 Wh

### POWER GENERATION

#### DUAL SOLAR ARRAY ROTORS

Normal Mode, one rotor active

    Minimum Orbit Average Power: 80 W, summer solstice, Alpha = 90°

    Peak Array Power in Sunlight: 152 W, winter solstice, Alpha = 60°

Survival Mode, two rotors active

    Minimum Orbit Average Power: 80 W

    Peak Array Power in Sunlight: 300 W

### LASSII MISSION

Seven Day Mission Models

Two Silver Zinc Batteries, 45% Depth of Discharge

Fourteen Day Mission Models

Three Silver Zinc Batteries, 75% Depth of Discharge

at 12.9 days worst case, to greater than 14 days.

*Flexibility inherent in the electrical power system design is as follows:*

1. Up to three silver zinc batteries, each storing 760 Ah (20 520 Wh), may be used.
2. Alternate primary battery types, i.e., lithium, or secondary batteries and chargers may replace the silver-zinc batteries (within the weight-volume constraints), producing different bus voltages, energy storage, and power delivery capabilities.
3. Nearly 300 W of continuous power from the solar array in sunlight can be attained by maintaining the solar array rotor spin axis normal to the Sun line; alternatively, the solar array panels could be removed.
4. Deployable fixed solar array paddles, or a Sun tracking deployable solar array could be designed to replace the LASSII dual rotor array (no study has been made for this concept).



### Microcomputer Controlled Command and Telemetry System—MICROCATS

MICROCATS will provide LASSII a capability for command distribution and telemetry acquisition. MICROCATS will acquire, format, and encode real-time telemetry data for transmission to ground stations, TDRSS, and storage in on-board tape recorders or memory. In addition, MICROCATS will decode, authenticate, and distribute to all spacecraft systems commands received from ground stations, TDRSS, or spacecraft memory. MICROCATS will provide spacecraft time information and logic timing signals for control of experiments and other spacecraft functions.

MICROCATS real-time data acquisition formats and command distribution are generated by microprogramming, with the format-generating algorithms, command collection, and command distribution algorithms stored in Programmed Read Only Memories (PROM). The use of microprogramming permits flexibility in formatting LASSII sequences by writing new microinstructions in PROM. All operations required for MICROCATS will be controllable directly, using PROM control techniques. The telemetry system will provide three fixed formats stored in PROM, and a stored memory for in-flight, reprogrammable formats. Communications between the data acquisition subsystems and MICROCATS are supported by a serial bus party line and the Special Retrieval Interface (SRI).

The MICROCATS top level specifications follow:

- Command Rates ..... 250 bps and 1 kbps for TDRSS
- Command Capability ..... 24 redundant, 16-bit serial magnitude word; 217 redundant, discrete/relay driver; 512 in-orbit programmable, stored commands; 6 timers, useable for delay commands.
- Telemetry Rates ..... Real-time or memory dump 250 and 8192 bps
- Stored Experiment Telemetry Transport Dump Rate ..... 1.3 Mbps maximum
- Telemetry Formats ..... 3 selectable preprogrammable formats and in-orbit programmable capability
- Telemetry Capability ..... Retrieval interface units: 768 redundant inputs; all inputs useable for analog/discrete, bi-level; 192 inputs useable for serial digital; each word 8 bits. Special retrieval interface units; 128 redundant inputs useable for bipolar/unipolar analog and discrete bi-level; 16 useable for serial digital; each word 12 bits.
- Telemetry Memory ..... 22 bits per word; 8k words of memory, 6 bits of error correction and 16 bits of data.
- Transport Recorder Rates ..... 134 and 268 kbps
- Transport Storage .....  $1.7 \times 10^9$  bits—redundant.

MICROCATS architecture is very similar to that of most ground computer systems. This architecture allows the addition and changes of interfaces with a minimum impact. MICROCATS has concentrated all possible functions in firmware and not in hardware. It is possible to augment or redirect

MICROCATS requirements with a minimum of hardware redesign. This allows the addition of new functions or interfaces by the addition of physical hardware interface boards to MICROCATS mainframe. Each new interface will increase MICROCATS size by one-half inch. MICROCATS remote data acquisition units and remote command decoders are responsible for communication with MICROCATS for retrieving data and distributing uplink commands via a redundant party bus. The remote unit capability can be expanded by adding additional remote units or expander units.

#### Attitude Control System

The attitude control system achieves stabilization by the bias momentum technique. A momentum wheel is located in the despun section with spin axis aligned to the pitch or rotor axis. Wheel momentum is augmented by rotor momentum for additional gyroscopic stiffness. The total wheel/rotor angular momentum is typically 70 ft-lb-s. Larger wheels may be used in missions where aerodynamic fuel usage effects become critical. A small reaction wheel is used to provide full three-axis stabilization of the stator section with the ram face aligned perpendicular to the velocity vector.

Attitude sensing is achieved with redundant IR sensors. These may be either mounted on independent scanwheels or made integral with the momentum wheel. Fine and coarse static sun sensors and a three-axis magnetometer all mounted on the stator section are also provided. Additional components include a two-axis rate integrating gyro for short-term attitude reference and a three-axis accelerometer package for  $\Delta V$  control and drag measurements.

The key attitude and propulsion control system specification parameters are as follows:

System	Performance/Specification	
Attitude Control	Attitude Measurement	
	Roll	$\pm 1.0^\circ$
	Pitch/Yaw	$\pm 0.5^\circ$
	Attitude Stability	
	Max rate, all axes	$\pm 0.4^\circ/\text{min}$
	Control, all axes	$\pm 1.0^\circ$
	Weight	163 lb
Propulsion	Total Average Power	55 W
	Thruster Configuration	12 0.2 lbf bol 4 5.0 lbf bol 1 150 lbf bol
	Fuel Capacity	750 lb $\text{N}_2\text{H}_4$
	Max Total $\Delta V$ Capability	2034 fps

The ACS design concept allows for substantial improvement in control accuracy to support expanded missions. The electronics is designed with an independent microprocessor that interfaces with the individual sensors and reaction devices. This allows flexibility limited only by the amount of memory. The present configuration requires 25% of the maximum limit of memory, thus allowing considerable expansion. Sensor additions or deletions can be handled relatively easily with this approach.

The ACS, as presently configured, is designed to support the current complement of LASSII experiments. These requirements are satisfied by a control system providing accuracies of  $0.5^\circ$  to  $1.0^\circ$  in attitude measurement and  $1.0^\circ$  in attitude control.

Increased control and stability over current levels could be achieved by changing algorithms and deadzones and supplying more fuel. Depending on the mission length and fuel available, the present

configuration could achieve  $0.2^\circ$  measurement and control accuracies. If the spacecraft weight grew, the  $0.2^\circ$  mission could be supported with the same electronics if more fuel were available and larger wheels were substituted.

Further increases in accuracy and control would require improved attitude reference data. This could be achieved by the addition of a high-accuracy Inertial Reference unit, star sensors, and a new software package. The design of the basic electronics allows this to be done but at a significant cost increase for those new items.

### **Radio Frequency System**

The RF system provides dual band, multimode communications operation. S-band capability includes high, medium, and low bit rates and high-gain and omnidirectional antennas. The VHF hardware provides medium and low bit rates with omnidirectional coverage. The top-level specifications follow:

#### **A. Forward Link (Up Link)**

1. TDRSS Multiple Access Compatible
  - a. Bit rate 250 bps
  - b. Omni antenna
  - c. RF frequency 2106.4 MHz
2. TDRSS Multiple Access compatible
  - a. Bit rate 1000 bps
  - b. 18 dBi antenna gain
  - c. RF frequency 2106.4 MHz
3. TDRSS S-Band Single Access compatible
  - a. Nominal bit rate 1000 bps (max data rate greater than 100 kbps)
  - b. 18 dBi antenna gain
  - c. RF frequency 2025 to 2120 MHz
4. Blossom Point Tracking Station compatible
  - a. Bit rate 1000 bps
  - b. VHF omni antenna
  - c. RF frequency 142 MHz

#### **B. Return Link (Down Link)**

1. TDRSS Multiple Access compatible
  - a. Bit rate 256 bps
  - b. Omni antenna
  - c. 5 W transmitter output
  - d. RF frequency 2287.5 MHz

2. TDRSS Multiple Access compatible

- a. Bit rate 8192 bps
- b. 18 dBi antenna gain
- c. 5 W transmitter output
- d. RF frequency 2287.5 MHz

3. TDRSS S-Band Single Access compatible

- a. Bit rate 1.3 Mbps
- b. 18 dBi antenna gain
- c. 20 W transmitter output
- d. RF frequency 2200 to 2300 MHz

4. Blossom Point Tracking Station compatible

- a. Bit rate 256 or 8192 bps
- b. VHF omni antenna
- c. 0.5 W transmitter output
- d. RF frequency 136 to 138 MHz

The RF system is generally built from a number of modules. Both the S-Band Single Access transponder and the Multiple Access transponder are modularized and can be configured to slightly different requirements. Different power amplifiers can be employed to allow more efficient utilization of higher or lower bit rates. The antennas can be in a different configuration to accomplish the same purpose.

The VHF portion of the system can also have an alternate transmitter, receiver, or antenna to fill different needs.

**Thermal Protection System**

LASSII thermal design satisfies thermal requirements for the free-flyer portion of the mission as well as the storage time in the Shuttle cargo bay.

Both active and passive thermal control techniques are used. The thermal protection system (TPS) consists of multilayer insulation, radiators, thermostatically controlled heaters, ammonia filled heat pipes, and a freon liquid loop system with a positive displacement pump.

The following data were derived and used in developing the thermal design for LASSII and selecting components for the thermal protection system.

**Orbital average flux intensity**

Solar: 282.5 W/m<sup>2</sup>

Albedo: 44.6 W/m<sup>2</sup>

Earth IR: 76.2 W/m<sup>2</sup>

**Primary heat rejection radiator**

338 W rejected @ t = 0°C

442 W rejected @ t = 10°C

557 W rejected @ t = 20°C

- Radiators sized to reject internal power dissipation as well as absorbed fluxes.
- Internal temperature of spacecraft  $20^{\circ} \pm 10^{\circ}\text{C}$ .
- Maintain temperature of hydrazine system above  $10^{\circ}\text{C}$  by thermostatically controlled heaters.
- Heaters on all experiments to maintain lower temperature limits.

Use of the heat pipe and liquid loop systems allows flexibility in transferring heat to the radiator and in the placement of the various components. Most of the heat in the stator is conducted to the back-side radiator for rejection from the spacecraft, leaving the remaining outer surfaces free for experiment mounting and for providing the maximum gold surface environment for the plasma experiments. With the same thermal protection system, any mission not requiring as much gold surface would allow greater internal power dissipation.

### Structures and Mechanisms

The LASSII physical configuration (Fig. 4.1) consists of a stable platform (stator) and a rotating platform (rotor). The stator consists of a box structure 40 in. wide by 70 in. long by 90 in. high. It contains most of the housekeeping, control, and power systems plus those experiments that require location on a stable platform. A 40 in. diam by 32 in. high spherical antenna is located on top of the stator. The rotor consists of two tapered octagons, and a regular octagon which mounts to the end of one of the tapered octagons. The octagons are located on either side of the stator ( $70 \times 90$  surfaces) and connected by a common shaft. The tapered octagons provide the support structure and surface area for the solar arrays. The regular octagon houses experiments. The tapered octagon sections are 34 in. long and 67.4 and 49.9 in. across the flats. The regular octagon is 49.9 in. across the flats by 12 in. high. The overall envelope for the LASSII spacecraft is 124 in. wide by 130 in. high by 75 in. deep. LASSII is designed to be accommodated by its own pallet within the Space Shuttle. The overall weight of LASSII is approximately 3000 lb.

The LASSII spacecraft configuration will accommodate a wide variety of experiments both internally and externally. Equipment inside the spacecraft will be mounted in a modular fashion as far as practical. This will allow rapid and easy exchange of equipment and experiments. Externally mounted probes may be mounted on most surfaces with limitations and restrictions controlled primarily by other experiments and the particular mission.

Should the requirements arise, the volume of the LASSII spacecraft can be increased. The width and depth dimensions may be increased with a minimum of redesign. These dimensions are restricted primarily by the Space Shuttle envelope and the LASSII support pallet configuration.

## 5.2 LASSII Electrical Power System

### General Requirements

An electrical power system is required to provide energy to the LASSII scientific experiments, data conditioning and storage equipment, telemetry system, and for other nonscience or engineering housekeeping functions. Mission periods of 7 days and 14 days, including launch and retrieval, are envisioned. Expansion to 30 days is also within design capabilities.

The electrical power system is largely nonmagnetic, and the magnetic field generated by the delivery of power is minimized. Surface conductivity of the satellite exterior is maximized to improve stability of the spacecraft potential, and exposed power system electrical conductors are avoided to

reduce stray field penetration of the ambient plasma and possible distortion of sensitive plasma measurements.

### 5.2.1 Load Requirements

The design electrical losses for all engineering components and scientific experiments are given in Table 5.2-1 for the expected and contingency operational modes. A 30% growth allowance is provided for the scientific payload. Loads shown are the average of duty cycled or variable loads for the conditions listed. The difference between sun period loads and eclipse loads is attributable to nickel cadmium battery trickle charge while in sun. Figure 5.2-1 depicts a typical three-orbit operational profile for a maximum eclipse orbit. Operational modes 2, 3, and 4 (see Table 5.2-1) are shown, which include the science and data dump modes.

### 5.2.2. Electrical Power Systems Description

The LASSII electrical power system (EPS) design is a hybrid between typical long-duration power systems, with a full-capability solar array and secondary batteries, and an all primary battery energy storage system useful for short-duration or suborbital missions. The concept evolved in response to LASSII scientific requirements.

The power system includes a solar array designed to support the major fraction of housekeeping and engineering loads. This array consists of a nonshadowed array designated the primary array, and a partially shadowed array designated the auxiliary array. Multiple primary silver zinc batteries support the science and data transmission loads, and share loads with the solar array as needed. The silver zinc batteries are not recharged, and when nearing depletion, limit the scientific mission duration.

The LASSII EPS concept offers the advantages of an inherently regulated low-impedance electrical power source in the silver zinc batteries while the solar array "saves" extensive use of the battery during sunlight nonscience periods. The solar array, in conjunction with a small secondary nickel cadmium battery, provides the additional advantage of a low-power survivability mode. Survival in mode 7 is accomplished by turning off all science and nonessential engineering loads, and permitting the bus voltage to go unregulated (21 to 27 Vdc). Control of LASSII can be maintained until capture by the Shuttle is achieved.

During normal operations the nickel cadmium battery is also connected through its charger and a diode discharge gate to an auxiliary unregulated bus. This bus uses the solar array power from the non-dedicated rotor and the nickel cadmium battery to provide an energy pool for the thermal control system. Although both the battery charger and thermal system will preferentially use the auxiliary bus as a power source, both will use main bus power should the battery become deeply discharged and temperatures in the LASSII fall too low. This auxiliary and the primary solar arrays will also be open circuited during science collection orbits.

An electrical power system block diagram appears in Fig. 5.2-2.

### Solar Array Description

The solar array design has taken into consideration the science requirements and constraints as a primary objective. Ten square meters of highly conductive gold coating on the satellite surface have been maintained. No protrusions of the solar array will penetrate the plane of the RAM surface. The exposed surface of the solar array panels are conductive and are essentially at ground potential. No solar array electrical conductors are exposed to the plasma. The solar panel circuitry will use antimagnetic paths to virtually eliminate magnetic field generation due to the flow of electrical current.

Table 5.2-1 — Operational Modes

Mode	Mode Description	Electrical Power System									Ther Ctrl System		Attitude Control System						
		Ag Zn Batt	Solar Array	Ni Cd Batt*	Ni Cd Charger*	Shunt Reg	±12V Reg	Pwr Dist Unit	Ord Ctrl Dist Unit	Exp Ctrl Unit	Ther Ctrl Unit	Rotor Motor	Momen Wheel 1	Momen Wheel 2	Ctrl Elect	Horizon Scanner	Fine Sun Sensor	Coarse Sun Sensor	
0	Mated with Orbiter	0	(On)	5.6	2.0	1	4	1	0	1	10	0	0	0	10	0	0	0	
1	Separation and Science-off	0	(On)	5.6/0	2.0/1.4	1	4	1	0	0	10	15	8	2	10	12	1	1	
2	Coast Mode Science Standby Bit Rate-256 BPS OMNI Antenna On	0	(On)	5.6/0	2.0/1.4	1	4	1	0	1	10	14.25	7.6	1.9	10	11.4	.95	1	
3	Research Mode Science Tape On, OMNI Antenna On Solar Array Off Bit Rate 256 BPS	0	(Off)	0/0	1.4	1	4	1	0	1	10	14.25	7.6	1.9	10	11.4	.95	1	
4	Dump Mode, Science Standby, Tape Dump, HPA On Steerable Antenna on Bit Rate 1 MBPS	0	(On)	0/0	1.4	1	4	1	0	1	10	14.25	7.6	1.9	10	11.4	.95	1	
5	Maneuver Mode Bit Rate 8 KBPS Steerable Antenna On, Science Standby	0	(On)	5.6/0	2.0/1.4	1	4	1	0	1	10	14.25	8	2	10	12	1	1	
6	(Same as 5 but Science Completely Off)	0	(On)	5.6/0	2.0/1.4	1	4	1	0	1	10	14.25	8	2	10	12	1	1	
7	Survival Mode Science Off, Engr Standby, All S-Band Off, VHF On AG ZN Off Bit Rate 256 or 8 KBPS	(Off)	(On)	44.45/0	5.4/1.4	1	4	1	0	0	10	4.75	7.6	1.9	10	0	0	0	

Mode	Mode Description	Science Experiments																Grand Total		
		Spin Section Experiment Number							De Spun Section Experiment Number							Science Total	Science Incid. Contin.	Sun	Eclipse	
		2	5	6	11	12	13	14	1	3	4	7	8	9	10					15
0	Mated with Orbiter	0	0	0	0	0	0	0	0	0	0	0	0	0	0	0	0	0	50.75	—
1	Separation and Science-off	0	0	0	0	0	0	0	0	0	0	0	0	0	0	0	0	0	147.5	141.3
2	Coast Mode Science Standby Bit Rate-256 BPS OMNI Antenna On	0	0	0	0	0	2.3	0	10	3	0	0	0	0	0	0	15.9	20.7	166.25	160.05
3	Research Mode Science Tape On, OMNI Antenna On Solar Array Off Bit Rate 256 BPS	.35	6	18	5.5	1.8	3.1	Neg.	10	16	6	18	5	5.5	2.4	.6	98.25	127.7	280.8	280.8
4	Dump Mode, Science Standby, Tape Dump, HPA On Steerable Antenna on Bit Rate 1 MBPS	0	0	0	0	0	2.3	0	10	3	0	0	0	0	0	.6	15.9	20.7	329.05	329.05
5	Maneuver Mode Bit Rate 8 KBPS Steerable Antenna On, Science Standby	0	0	0	0	0	2.3	0	10	3	0	0	0	0	0	.6	15.9	20.7	176.25	170.05
6	(Same as 5 but Science Completely Off)	0	0	0	0	0	0	0	0	0	0	0	0	0	0	0	0	0	155.55	149.35
7	Survival Mode Science Off, Engr Standby, All S-Band Off, VHF On AG ZN Off Bit Rate 256 or 8 KBPS	0	0	0	0	0	0	0	0	0	0	0	0	0	0	0	0	0	92.94	44.49

\*Two levels of power consumption shown separated by slash (/) indicate sunlight and eclipse load respectively.

## Operational Modes

n	Attitude Control System								Telemetry and Command System				RF System						Engr Total	
	Ctrl Elect	Horizon Scanner	Fine Sun Sensor	Coarse Sun Sensor	Accelerometer	Magnetometer	Rate Gyro	RCS	STACC	7 RMTS	Tape	Ant	XMTRS	Rec 1-5	Rec 2-5	Amp-5	XMTR V	Rec-V	Sun	Ecl use
2	10	0	0	0	0	0	0	0	3.25	11.9	0	0	0	0	0	0	0	1	50.75	—
	10	12	1	1	1	1	6	1.5	3.25	11.9	0	0	25	12	12	0	25	1	147.5	141.35
	10	11.4	95	1	.95	1	6	.15	3.25	11.9	0	0	25	12	12	0	25	1	145.55	139.35
	10	11.4	95	1	.95	1	6	.15	4.0	14.0	11.15	0	25	12	12	0	25	1	153.1	153.1
	10	11.4	95	1	.95	1	6	.15	4.0	14.0	51.5	15	25	12	12	100	25	1	35	308.35
	10	12	1	1	1	1	6	1.5	3.25	11.9	0	15	25	12	12	0	25	1	160.55	154.55
	10	12	1	1	1	1	6	1.5	3.25	11.9	0	15	25	12	12	0	25	1	160.55	154.35
9	10	0	0	0	0	1	0	.15	.32	.12	0	0	0	0	0	0	25 10% Duty	1	92.94	44.49

2



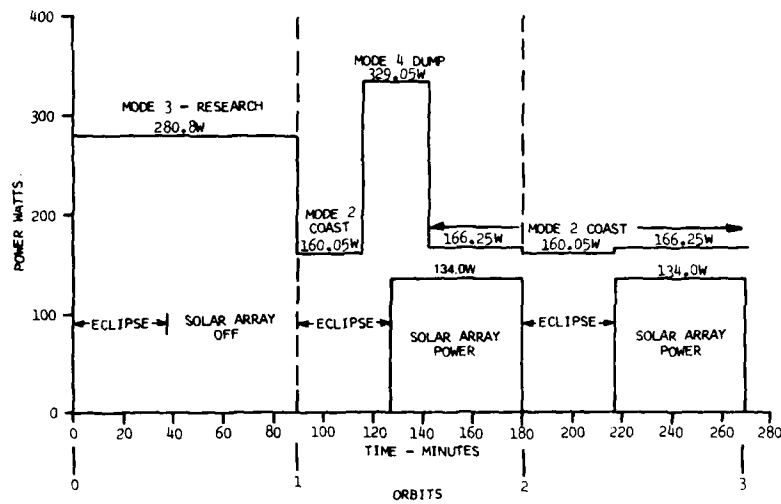


Fig. 5.2-1 - LASSII-three orbit load profile during science phase of missions minimum sun orbit

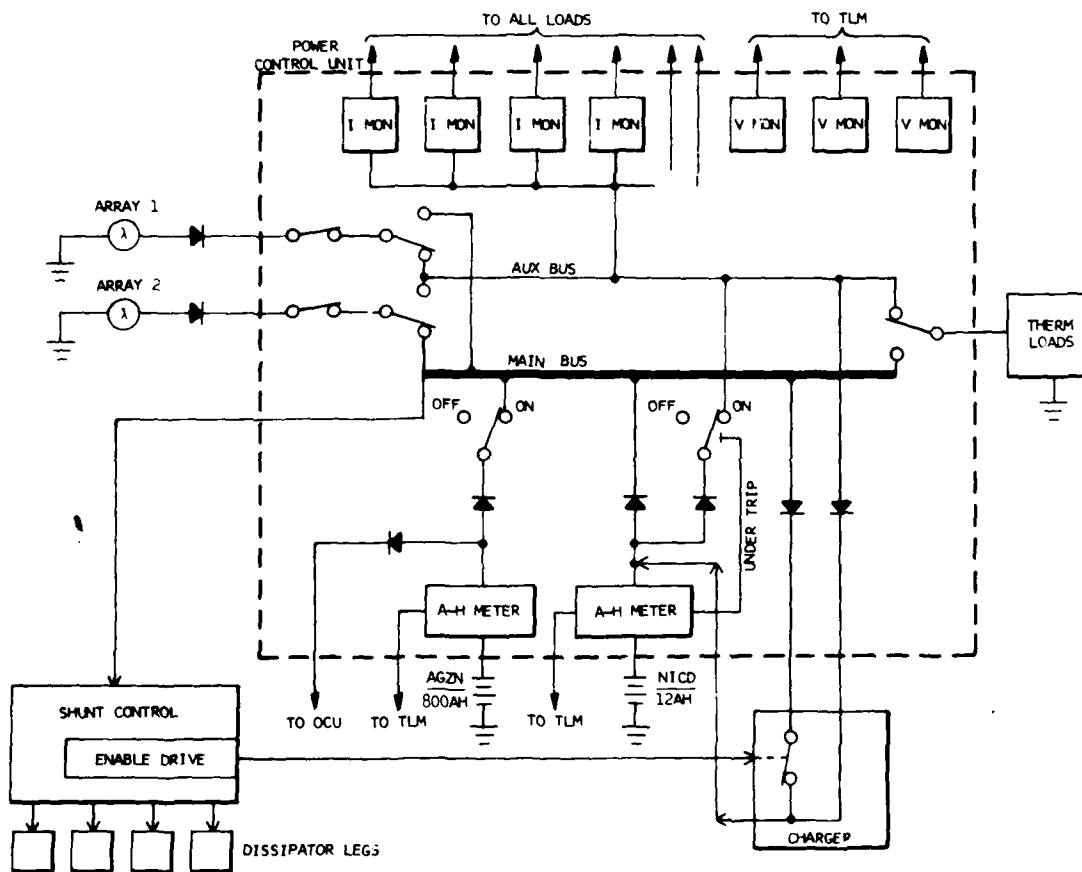


Fig. 5.2-2 - Electrical power system block diagram

The solar arrays are located on the rotors of the satellite. Use of a spinning solar array reduces solar cell temperature to provide greater efficiency. The slope of the array surfaces on the drum has been optimized to provide a uniform minimum average orbital power generating capability under all solar angles possible in the LASSII orbit planes. When the angle of the orbit plane with respect to the sunline is such that one drum is shadowed by the stator section or antenna, the other drum provides continuous power. The partially shadowed array drum may be turned off, or left on to help support loads such as the thermal control system.

The electrical power generating capability of one solar array drum is shown in Fig. 5.2-3 as a function of alpha angle (the angle between the normal to the orbit plane and the sunline). With the selected system, orbit average power is used to size the array and determine the array panel slope angle. When the alpha angle is  $16^\circ$  or less (or  $174^\circ$  or more), the satellite is in full sunlight. The array generating capability is less than the load requirement, and the silver zinc battery will share the load. However, the average energy discharged from the battery, whether in the share mode or during satellite occultation in maximum eclipse orbits, is approximately equal.

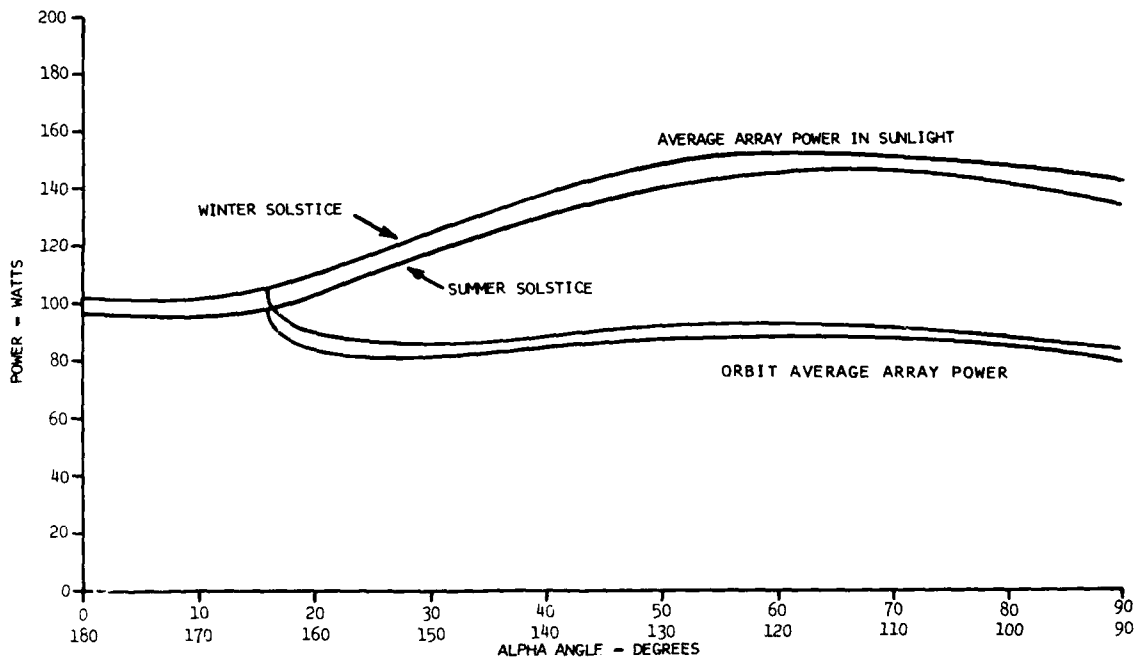


Fig. 5.2-3 — LASSII dual rotor solar array power, one drum, vs alpha angle (rotor slope  $15^\circ$ )

The solar array panels themselves are of unique configuration, but proven in concept and by application of variations of the concept. Rather than using the conventional individual cell glass covers, the LASSII array will use large sheets of glass to cover a number of cells and the cell electrical interconnections. The exposed exterior surface of the glass is coated with indium oxide,  $\text{InO}$ . The coating is essentially transparent (95% transmittance in the wavelength band of solar cell response), yet has a surface resistivity of about 1000 ohms per square. The edges of the glass covers have nontransparent metallization to facilitate current collection and grounding of the conductive  $\text{InO}$  coating. The interconnected solar cells are mounted to the inner surface of the glass, thus preventing exposure of the solar array electrical potential to the plasma under investigation.

Directly under each solar cell circuit is mounted a sheet consisting of expanded copper foil sandwiched between thin epoxy impregnated fiberglass material. The copper foil provides the electrical conductor for the circuit of solar cells wherein the current generated by the cells flows equally in the opposite direction. The solar cells and the electrical return path are separated by only a few thousandths of an inch of insulator. This antimagnetic technique, used in conjunction with twisted power and return leads, will minimize any current generated field due to the solar array.

**Solar Cells**—The selected solar cell is a 2 by 4 by 0.03 cm low base resistivity ( $2\Omega$  cm) shallow junction silicon cell with a back surface reflector. The cell is approximately 12% efficient, but most importantly the cell has a fairly high voltage at its maximum power point, a low thermal absorptance, and on a watts/cost basis is more economical than higher efficiency cells.

Based on the maximum expected solar array temperature of  $48^{\circ}\text{C}$ , 66 series cells will be required to provide the necessary voltage to supply the electrical bus. A circuit of a single cell series will be used to minimize shadowing losses and facilitate the circuit layout. Nonmagnetic silver mesh intercell connectors with multiple contacts will be soldered to the cells to complete the circuit.

The back of each solar array panel, inside the rotor, will be thermally insulated to ensure proper temperature control of the array.

#### Silver Zinc Battery Description

The silver-zinc batteries for LASSII are based on an existing space qualified cell design. Eighteen cells in series provide a constant voltage output in the  $27 \pm 1$  V range under the expected loads. Two batteries would provide adequate energy storage for 7-day missions, and the satellite design will permit the installation of a third battery for the extended missions. For handling convenience, each battery will be divided into three six-cell assemblies. The LASSII battery characteristics are tabulated in Table 5.2-2.

As all silver zinc batteries tend to continuously evolve hydrogen, each six-cell sealed case will also contain a scavenging cell to harmlessly react the hydrogen to water.

Table 5.2-2 — LASSII Battery Characteristics

- Silver Zinc	- Single Mission
- Proven Cell	- Eagle Picher MAP 4453
- Mission Capacity Rating	- 760 Ah
- Two or three, 18-cell Batteries in 6-cell modules	
- Battery Voltage	- 28.7 - 26.7 Vdc
- Bus Voltage	- 28.0 - 26.0 Vdc
- Maximum Depth of Discharge	- 75%
- Estimated Mass	- 216 lb/18-cell battery

**Battery Cell** — The silver zinc cell, designated MAP 4453 by Eagle Picher Industries, is nominally rated at 800 ampere hours (Ah). The cell incorporates secondary cell type separator to improve wet stand life and reliability, but without the excess negative active material required for true secondary cell application. The lack of excess negative material saves weight, but severely limits the storable capacity on recharge.

Figure 5.2-4 depicts the voltage characteristic of a sample MAP 4453 cell under load. Although the test depicted was designed for another program, the rates used are comparable to those required for the LASSII mission. Initially, the cell voltage exceeds the value corresponding to an 18 cell,  $27 \pm 1$  V bus voltage, (allowing 0.7 V drop for diode gates). But this higher voltage persists for only about 3% of the total capacity and could readily be removed prior to installation. The depicted test begins with a low rate discharge until 400 Ah of capacity have been removed. At that point the discharge rate is increased to 3 A continuously, except for a 4.5 s, 15 A pulse once each hour. The battery is rerated for the LASSII mission to the useful voltage range under LASSII loads to 760 Ah total capacity. To provide a mission reserve, only 75% or 570 Ah will be the maximum design depth of discharge for any mission.

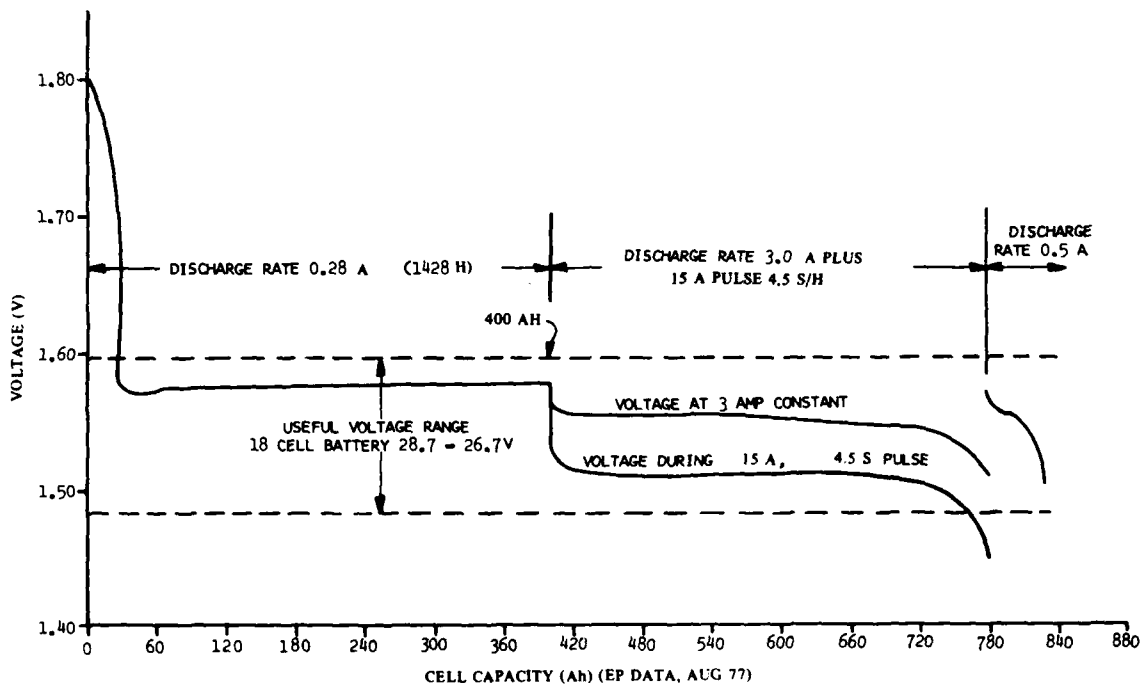


Fig. 5.2-4 — Map 4453 cell voltage discharge voltage profile

**Hydrogen Management** — Silver zinc battery cells continuously evolve hydrogen at low rates both on open circuit and during discharge. It is not practical to construct a battery case with sufficient strength and volume to contain the hydrogen for the mission duration. Each cell is fitted with a pressure relief valve to permit cell venting into the common battery module sealed enclosure. Rather than venting the pressure within the battery case overboard, an additional single cell, using either the nickel hydrogen or silver hydrogen system, will be incorporated in each module. Hydrogen within the battery case would be free to enter the cell and would be catalyzed to water at the hydrogen electrode. The initially fully charged counter electrode ( $\text{Ag}_2\text{O}$  or  $\text{NiOOH}$ ), when connected through a resistor to the hydrogen electrode, would discharge in proportion to the hydrogen consumed. The reaction is safe and reliable, involving hydrogen and hydroxyl ions, and the small amount of heat evolved would be dissipated external to the battery (2.6 mW/module). No net water is produced, since the discharge of the positive electrode consumes water and yields hydroxyl ions.

### Nickel Cadmium Battery Description

A small nickel cadmium battery is incorporated into the electrical power system for the main purpose of providing a rechargeable energy storage device for the Mode 7 survival operation should the primary silver zinc batteries approach the 75% depth of discharge (leaving 25% for mission reserve) and recapture by the shuttle not being imminent. With all loads reduced to minimum values, and the silver zinc battery off line, the solar array and nickel cadmium battery will provide an unregulated bus with sufficient orbital average power to maintain attitude control and communications capability.

The nickel cadmium battery will consist of 18 cells rated at 12 Ah and provide an energy storage on 270 Wh. Typical maximum depth of discharge is 10% of capacity. The battery design is similar to that used on other satellites and would weigh approximately 28.5 lb.

Throughout the normal mission, the nickel cadmium battery is connected to the auxiliary bus for use with the thermal control subsystem. Recharge is accomplished from the auxiliary solar array rotor.

Nickel cadmium batteries are inherently magnetic. A battery of twice the capacity has been measured as having a residual magnetic dipole moment equal to 1800 pole-cm. After "de-perm" the same battery measured a magnetic moment equal to 18 pole-cm. To reduce the magnetism further, a shielded case would be applied.

### Battery Charger

The nickel cadmium battery charger utilizes solar array power that is excess to the load requirement to maintain a trickle charge on the battery. A second commandable charge mode provides up to 3 A to recharge the battery in the survival mode, and automatically reduces the charge current based on the battery voltage and temperature once full charge is approached.

This charger design has been proven in over 4 years of orbital operation. Its weight is approximately 1.2 lb.

### Shunt Regulator and Dissipators

A linear, sequential shunt regulator is used to limit the maximum voltage of the bus when the solar array generates more power than is required by the loads. The regulator senses the variations in bus voltage due to changes in loads and array output and applies an error signal to each of nine shunt regulator drivers. As each shunt operates within a given voltage band, separated from the others by a dead band, only one regulator is in active control at any time. The other shunts are either saturated or off, minimizing variable dissipation in the regulator. The resistive dissipators themselves are located on the rear side of the solar array panel, so that excess heat is released overboard. The total voltage control band for all nine regulators, including dead bands, lies within a range of 28.0 to 28.8 V. Each shunt can handle 1.5 A of current, giving a total of 13.5 A of shunting, which exceeds the maximum array capability by 1.5 A. The shunt control and dissipators design have been proven in application. The regulator weighs 3 lb, and each of the nine dissipators weighs 1 lb.

### 12 Volt Converter

The LASSII 12 V converter provides  $\pm 12$  Vdc for experiment and housekeeping loads. It is a redundant unit packaged in a single enclosure.

This unit is a dc to dc switching converter utilizing standard transformer coupling techniques.  $\pm 12$  Vdc power from this converter will be source regulated better than 1%. The principle type of load will be instrumentation amplifiers and as such, the converter will provide low noise power. Switching

of  $\pm 12$  Vdc power to loads will be done by the Power Control Unit (PCU) and the Experiment Control Unit (ECU).

#### Power Control Unit

The LASSII Power Control Unit (PCU) is the primary control and distribution element in the EPS. All sources of power and all loads are interfaced here. In addition, the PCU provides instrumentation of source and load voltage and current.

The PCU is pictured in the EPS block diagram (Fig. 5.2-2). The two rotor-mounted solar arrays are individually switched on, off, or to either power bus. Power for the main bus comes from the solar arrays and the two batteries. The primary battery (silver zinc) can be switched on or off the main bus. The secondary battery (nickel cadmium) is permanently connected to the main bus and is switched onto the auxiliary bus as long as its state-of-charge does not become too low. The secondary battery is charged from the auxiliary bus given sufficient potential. It can also be charged from the main bus. Main bus charging requires an enable signal from the shunt control electronics. Battery charging then takes place prior to shunt leg conduction.

Current, voltage, and ampere-hour monitors are contained within the PCU. (Note: Several monitor functions are not noted in the block diagram.) The Shunt Control Unit is connected to the main bus and allows the NiCd charger to preferentially absorb excess array power.

#### Experiment Control Unit

The LASSII Experiment Control Unit (ECU) is the primary configuration, instrumentation, and control interface for experiment dc power. This unit is redundant in critical functions and matches redundancy with the experiment loads in individual functions. The ECU is packaged in a single enclosure.

The ECU receives power from the EPS. This power is then conditioned, instrumented, and switched as necessary for the experiment loads. The ECU also serves as isolation between the experiments and the EPS in both buffering and fault unloading functions. The ECU interfaces with the command and telemetry systems for control and instrumentation requirements.

#### Ordnance Control System

The LASSII Ordnance Control System provides the necessary conditioning, logic, and switching to control and meter all electrically initiated pyrotechnic functions. The space flight electronics are packaged in a single enclosure Ordnance Control Unit (OCU).

Figure 5.2-5 is the Ordnance Control System block diagram. The functions internal to the OCU are shown with top level interfaces both in and out of the box. Actuation of any LASSII pyrotechnic event is controlled by several levels of interlocks. Closure of LASSII/SHUTTLE separation switches occurs at the first moment of separation. This switch closure will enable further Ordnance Control System "unlocking" via the command system.

Certain events are actuated by a general purpose OCU timer. An example is the timed shutdown of OCU enable circuitry to disallow inadvertent commands from affecting the OCU when not in sight of TDRSS.

The OCU and its peripheral hardware is a completely redundant system. With exception of certain low-risk elements, no single point failures will cause an ordnance event to actuate or to be inoperable.

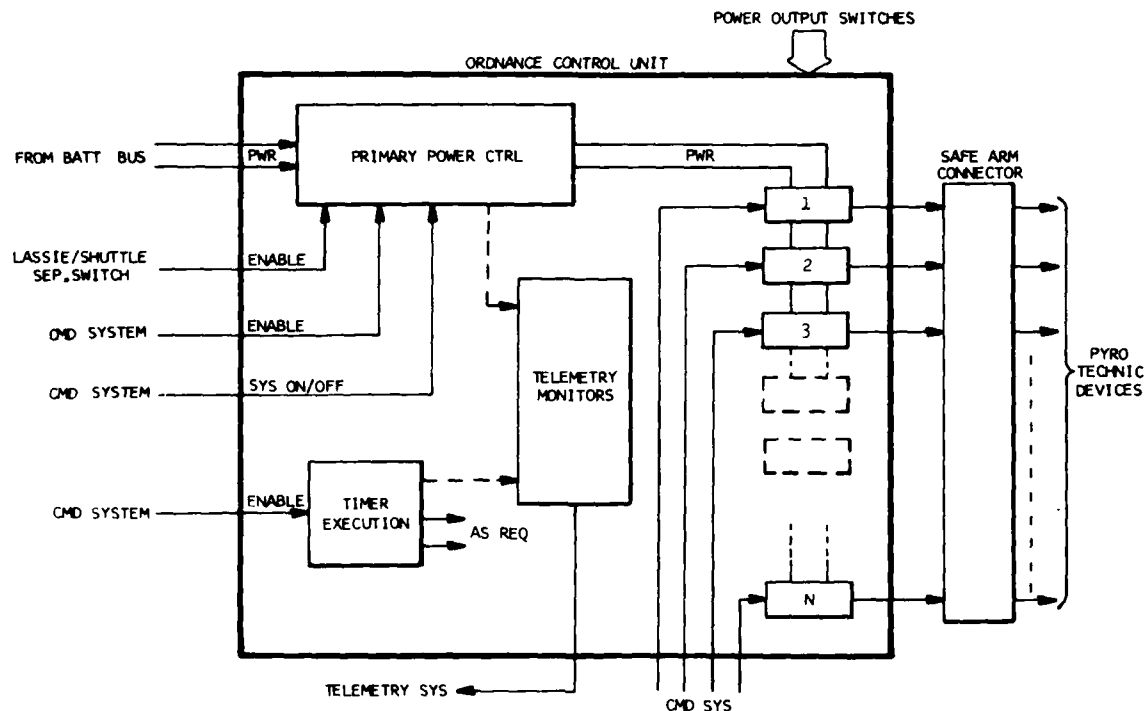


Fig. 5.2-5 — Ordnance Control System block diagram

The LASSII Ordnance Control System is designed to the requisite Navy, Air Force, and NASA ground and flight safety requirements. EMI protection is included in the form of shielded-twisted cabling and filtercon type connectors.

### 5.2.3 System Operation

#### General

During prelaunch, launch, and just prior to release from Shuttle, electrical power is provided from the Shuttle power system through an umbilical connection. Upon umbilical disconnect, the LASSII silver zinc batteries assume the engineering loads. Normal generation of solar array power will commence after release from the Shuttle RMS and after rotor spin-up has been initiated. Normally only one rotor solar array assembly is connected to the main bus to provide power since the other rotor will undergo substantial shadowing from the antenna dome and the stator and produce a pattern of largely unusable power. The shadowed array is connected to the auxiliary bus to provide limited power to the thermal loads and NiCd battery charging. During the engineering and science standby modes of operation, the solar array will provide the baseline power, with the silver zinc battery delivering current to the loads in excess of the array capability. When the array capability exceeds the load requirement, the shunts will limit the bus voltage and dissipate the excess power. During all eclipses, the silver zinc battery will support all loads. In the research mode, when the scientific experiments are gathering data, the solar array will be open circuited to bring to a minimum any magnetic field attributable to current flow in the array. Total power capability of the two silver zinc battery systems is in excess of 820 W at 27 V. Maximum bus voltage is less than 28.8 V with science in standby or off and the solar array on.

### Operational Modes

*Launch and Recovery* — Certain assumptions have been made regarding the operating modes of Table 5.2-1. Mode 0, while LASSII is in the Shuttle bay, shows minimum load consumption with all science completely off, and engineering systems on minimum power. The electrical supply is provided by the STS Orbiter during prelaunch, launch, and until just prior to RMS removal of LASSII from the Shuttle bay. Critical electronics checks are made in the bay prior to umbilical disconnect. Mode 1, separation, commences with umbilical separation and RMS removal of LASSII from the Shuttle. Additional electronics checks, including telemetry and science on-off functioning, are verified once LASSII is out of the Shuttle, but prior to release from the RMS. Mode 1 continues with release of LASSII and the initial stage of free flight. When adequate separation between LASSII and the Shuttle has been achieved, the remaining engineering systems are checked, attitude control initiated, and rotor operation begun. Mode 1 duration is expected to be approximately 24 hours.

*Free Flight Mission* — Mode 6, maneuver mode with science off, is used to obtain the proper separation time from the Shuttle or establish the overflight orbit. The difference between Mode 1 and Mode 6 is primarily the additional load of the steerable antenna to provide tracking and communication capability.

Modes 2, 3, and 4, the coast mode, research mode, and dump mode, respectively, combine to support the scientific functions of LASSII as depicted in Fig. 5.2-1. The operations profile for experiments is based on a 33% duty-cycle averaged over total flight time. During science collection and data storage the solar array is commanded off (open circuit) to minimize the magnetic field generation. This phase of the mission is interrupted by maneuver Mode 5 for orbit adjustments. Maneuver Mode 5 differs from Mode 6 in that science is now in standby.

At the completion of the scientific mission, Maneuver Mode 6 with science off would be initiated to return LASSII to the Shuttle location and prepare for capture and reinstallation in the Shuttle bay.

### Mission Models

*Seven Day Missions* — The electrical energy status for four 7-day mission profiles is shown in Table 5.2-3. These missions are assumed in the  $\alpha = 90^\circ$  orbit where eclipse is at maximum duration and at minimum solar constant, to present a nominal worst case capability. The operating modes are listed in Table 5.2-1 and described above. The 7-day mission models require two silver zinc batteries and provide more than adequate reserve energy storage.

*Fourteen Day Missions* — Table 5.2-4 depicts the same four mission models with extended scientific duration in a nominal 14-day mission. A maximum allowable 75% depth of discharge of the three silver zinc batteries limits the total mission duration. Maximum mission capability is in the range of 12.9 to 14.1 days at 33% science daily cycle but can be extended by corresponding reduction in percentage science on-time.

### 5.3 MICROCATS—Telemetry and Command System

The Micro Computer Controlled Command and Telemetry System (MICROCATS) will provide LASSII requirements for multiple data rates, multiple format organizations, TDRSS modulation, 15 experiment sources data sampling with 30% overdesign capability, strobes and clocks for synchronization of subsystems, tape recording of processed data, and capabilities for direct and indirect commanding of discrete and 16 bit serial magnitude words. See Tables 5.3-1, 5.3-2, and 5.3-3 for a summary of MICROCATS specifications.



Table 5.2-3 — Electrical Energy, Nominal 7 Day Mission Capability  
2 Batteries — Alpha 90° (Minimum Sun)

	Power Mode	Rev Start	Rev End	Time Start	Time End	Rev	Time	Initial Cap.	Avg. Load	Batt Net Load	Cap	Final Cap
	#	#	#	h	h	#	h	Wh	W	W	Wh	Wh
Mission 1	1	0	16	0	24	16	24	41040	1458.0	66.04	-1585	39455
	6	16	18	24	27	2	3	39455	158.0	79.1	-237	39218
	2,3,4	18	94	27	141	76	114	39218	218.0	165.4	-18856	20362
	6	94	96	141	144	2	3	20362	158.0	79.1	-237	20124
	6	96	112	144	168	16	24	20124	158.0	79.1	-1898	18226
DEPTH OF DISCHG: 55.6%												
Mission 2	1	0	16	0	24	16	24	41040	145.0	66.04	-1585	39455
	6	16	19	24	28.5	3	4.5	39455	158.0	79.1	-356	39099
	2,3,4	19	93	28.5	139.5	74	111	39099	218.0	165.4	-18359	20740
	6	93	96	139.5	144	3	4.5	20740	158.0	79.1	-356	20383
	6	96	112	144	168	16	24	20303	158.0	79.1	-1898	18485
DEPTH OF DISCHG: 55.0%												
Mission 3	1	0	16	0	24	16	24	41040	145.0	66.04	-1585	39455
	6	16	21	24	31.5	5	7.5	39455	158.0	79.1	-593	38862
	2,3,4	21	39	31.5	58.5	18	27	38862	218.0	165.4	-4466	34390
	5	39	44	58.5	66	5	7.5	34396	173.7	94.8	-711	33685
	2,3,4	44	62	66	93	18	27	33685	218.0	165.4	-4466	29219
	5	62	67	93	100.5	5	7.5	29219	173.7	94.8	-711	28508
	2,3,4	67	86	100.5	129	19	28.5	28508	218.0	165.4	-4714	23794
	6	86	96	129	144	10	15	23794	158.0	79.1	-1187	22608
	6	96	112	144	168	16	24	22608	158.0	79.1	-1898	20709
DEPTH OF DISCHG: 49.5%												
Mission 4	1	0	16	0	24	16	24	41040	145.0	66.0	-1585	39455
	6	16	21	24	31.5	5	7.5	39455	158.0	79.1	-593	38862
	2,3,4	21	34	31.5	51	13	19.5	38862	218.0	165.4	-3225	35636
	5	34	44	51	66	10	15	35636	173.7	94.8	-1422	34214
	2,3,4	44	57	66	85.5	13	19.5	34214	218.0	165.4	-3225	30989
	5	57	67	85.5	100.5	10	15	30989	173.7	94.8	-1422	29567
	2,3,4	67	81	100.5	121.5	14	21	29567	218.0	165.4	-3473	26094
	6	81	96	121.5	144	15	22.5	26094	158.0	79.1	-1780	24314
	6	96	112	144	168	16	24	24314	158.0	79.1	-1898	22416
DEPTH OF DISCHG: 45.4%												

## SZUSZCZEWICZ AND PALMA

Table 5.2-4 — Electrical Energy, Nominal 14 Day Mission Capability  
3 Batteries 8em Alpha 90° (Minimum Sun)

	Power Mode	Rev Start	Rev End	Time Start	Time End	Rev	Time	Initial Cap.	Avg. Load	Batt Net Load	Cap	Final Cap
	#	#	#	h	h	#	h	Wh	W	W	Wh	Wh
Mission 1	1	0	16	0	24	16	24	61560	145.0	66.04	-1585	59975
	6	16	18	24	27	2	3	59975	158.0	79.1	-237	59738
	2,3,4	18	186	27	280	168	252	59738	218.0	165.4	-41681	18057
	6	186	188	280	282	2	3	18057	158.0	79.1	-237	17820
	6	188	206	282	309	18	27	17820	158.0	79.1	-2136	15684
	Total Elapsed Time 12.9 DAY, Depth of Dischg: 74.5%											
Mission 2	1	0	16	0	24	16	24	61560	145.0	66.04	-1585	59975
	6	16	19	24	28.5	3	4.5	59975	158.0	79.1	-356	59619
	2,3,4	19	197	28.5	295.5	178	267	59619	218.0	165.4	-41681	17938
	6	197	200	295.5	300	3	4.5	17938	158.0	79.1	-356	17582
	6	200	218	300	327	18	27	17582	158.0	79.1	-2136	15447
	Total Elapsed Time 13.0 DAY, Depth of Dischg: 74.9%											
Mission 3	1	0	16	0	24	16	24	61560	145.0	66.04	-1586	59975
	6	16	22	24	33	6	9	59975	158.0	79.1	-712	59263
	2,3,4	22	73	33	109.5	51	76.5	59263	218.0	165.4	-12653	46610
	5	73	79	109.5	118.5	6	9	46610	173.7	94.8	-853	45757
	2,3,4	79	130	118.5	195	51	76.5	45757	218.0	165.4	-12653	33104
	5	130	136	195	204	6	9	33104	173.7	94.8	-853	32250
	2,3,4	136	188	204	282	52	78	32250	218.0	165.4	-12907	19349
	6	188	199	282	298.5	11	16.5	19349	158.0	79.1	-1305	18044
	6	199	217	298.5	325.5	18	27	18044	158.0	79.1	-2136	15908
Total Elapsed Time 13.6 DAY, Depth of Dischg: 74.2%												
Mission 4	1	0	16	0	24	16	24	61560	145.0	66.04	-1586	59975
	6	16	22	24	33	6	9	59975	158.0	79.1	-712	59263
	2,3,4	22	71	33	106.5	49	73.5	59263	218.0	165.4	-12157	47106
	5	71	82	106.5	123	11	16.5	47106	173.7	94.8	-1564	45542
	2,3,4	82	131	123	196.5	49	73.5	45542	218.0	165.4	-12157	33385
	5	131	142	196.5	213	11	16.5	33385	173.7	94.8	-1564	31821
	2,3,4	142	192	213	288	50	75	31821	218.0	165.4	-12405	19416
	6	192	208	288	312	16	24	19416	158.0	79.1	-1898	17518
	6	208	226	312	339	18	27	17518	158.0	79.1	-2136	15382
Total Elapsed Time 14.1 DAY, Depth of Dischg: 75.0%												

Table 5.3-1 — LASSII MICROCATS Summary of Specifications

1. COMMAND RATES:	250 bps and 1 kbps for TDRSS
2. COMMAND CAPABILITY:	24 redundant, 16 bit serial words; 217 redundant discrete or relay driver commands; 512 in orbit programmable stored commands; 6 timers, usable for delay commands.
3. TELEMETRY RATES:	Real time or memory dump — 256 and 8192 bps
4. STORED EXPERIMENT and TELEMETRY TRANSPORT DUMP RATE:	1.3 Mbps maximum
5. TELEMETRY FORMATS:	3 selectable preprogrammable formats plus in-orbit programmable capability
6. TELEMETRY CAPABILITY:	Retrieval interface units: 768 redundant inputs usable for analog or discrete bilevel; 192 inputs usable for serial digital, each word 8 bits. Special Retrieval Interface units: 128 redundant inputs usable for bipolar or unipolar analog or discrete bilevel; 16 inputs usable for serial digital, each word 12 bits.
7. TELEMETRY MEMORY:	8 K words, each word 22 bits long consisting of 16 bits of data and 6 bits of error correcting code
8. TRANSPORT RECORDER RATES:	134 and 268 kbps
9. TRANSPORT STORAGE:	$1.7 \times 10^9$ bits for each of two transports

### 5.3.1 Combined Telemetry and Command Subsystem

The LASSII Telemetry and Command subsystem, as shown in Fig. 5.3-1, is implemented by augmenting existing flight hardware. Figure 5.3-2 illustrates the existing MICROCATS Command and Telemetry system along with the interfaces which are added (in dashed lines) to implement the LASSII MICROCATS subsystem.

#### MICROCATS Functions

MICROCATS combines both telemetry and command functions under the control of a single microcomputer with the capability to select a wide range of sampling formats for telemetry data acquisition. These formats are both predetermined and frozen into control PROM for onboard use and determined dynamically after launch and uplink loaded into the MICROCATS memory unit.

Table 5.3-2 — LASSII MICROCATS Weight (lb) and Dimensions (in.)

Units	Weight	Length	Width	Depth
RIU-1-2-6-7	10.7	8.0	7.0	6.7
RIU-3-4	16.7	8.7	7.0	10.9
RIU-5	4.5	8.0	7.0	2.50
MCU-1-2	7.0	9.0	8.0	5.5
MMU-1-2	5.0	4.0	8.0	5.5
SRIU-1-2	2.0	8.0	7.0	1.4
PRE MOD	3.5	8.0	7.0	2.50
TAPE RECORDER 1-2	21.5	7.0	13.0	9.0

Table 5.3-3 — LASSII T&amp;C Power Consumption (W)

<b>RIU</b>	
STAND BY	1.7
DATA RATE OF 256 words per second	1.8
TOTAL RIU'S STAND BY	12
<b>SRIU</b>	
STAND BY	0.2
DATA RATE OF 4096 words per second	
RECORD MODE	5.1
TOTAL RIU'S STAND BY	0.4
<b>MCU</b>	
STAND BY	1.2
DATA RATE OF 8196 bits per second	5.6
DATA RATE OF 626144 bits per second	
RECORD MODE ONLY	20
<b>MMU</b>	
STAND BY	0.5
STORE RATE OF ONE SAMPLE every 3.2 seconds	1.3
READ MODE	1.8
<b>PRE MOD</b>	0.25
<b>TAPE RECORDER</b>	
STAND BY	0.25
RECORD MODE	9.1
REPRODUCE MODE	41.2

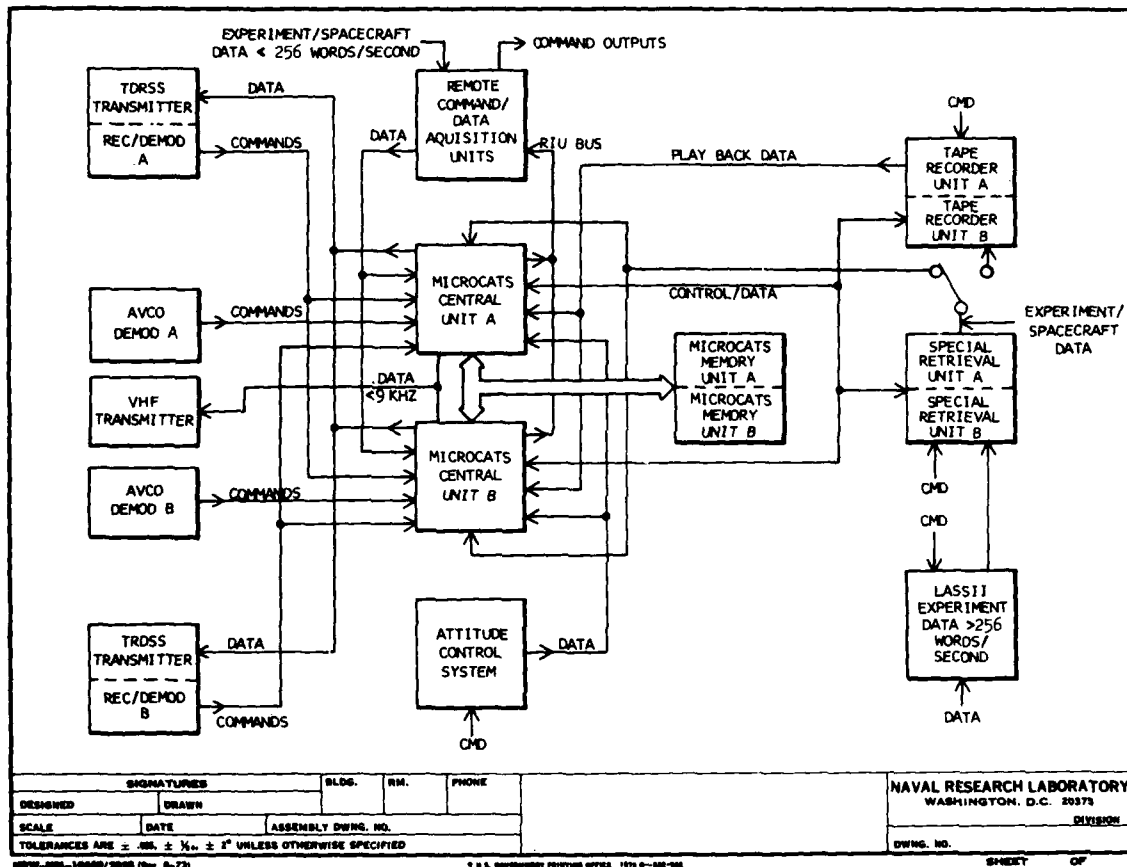


Fig. 5.3-1 — LASSII MICROCATS functional block diagram

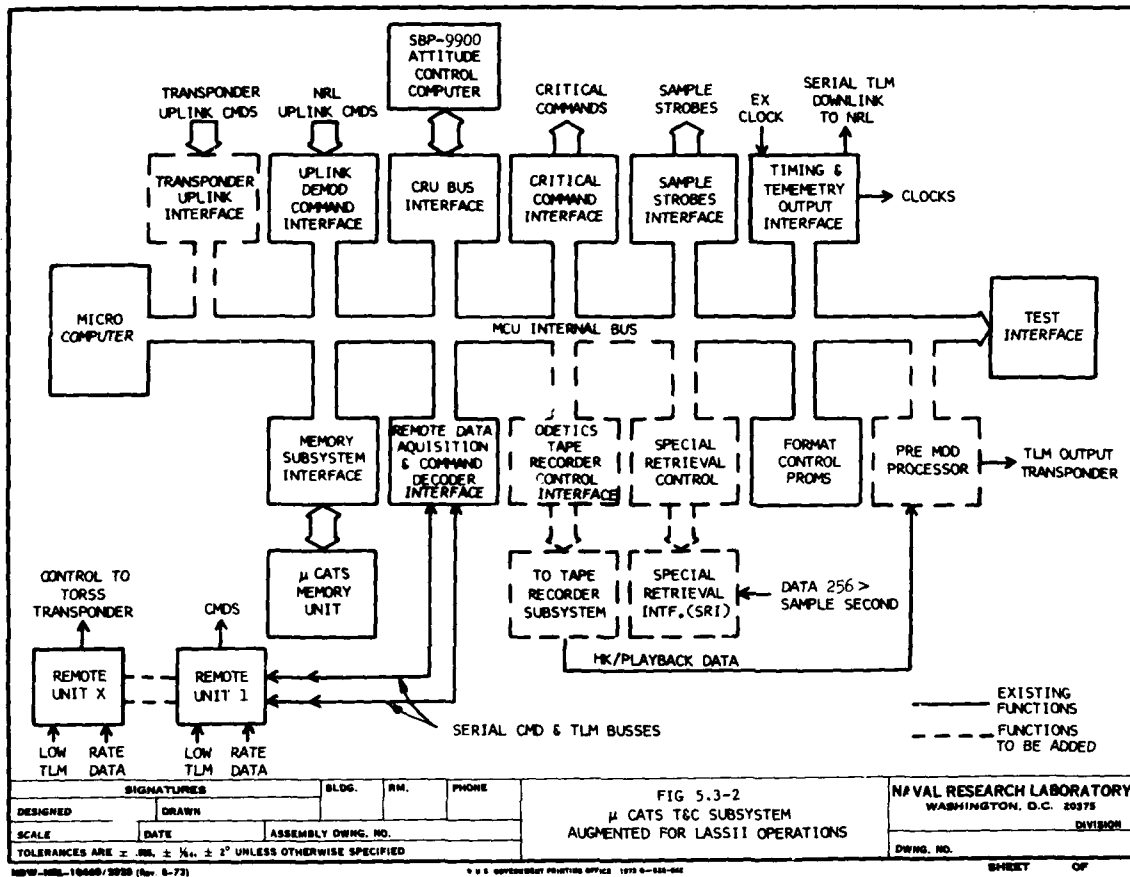


Fig. 5.3-2 — MICROCATS subsystem augmented for LASSII operations

**Interfaces** — MICROCATS provides one or more bidirectional links to the Texas Instruments SBP 9900 microcomputer. This bidirectional interface allows uplink loading of data base information and uplink control of Attitude Control System (ACS) modes. This interface also allows the ACS computer to request MICROCATS to acquire information relating to its sensors or to request MICROCATS to send control commands to the ACS functions.

MICROCATS provides a special 64 critical command output interface which is executed directly from the MICROCATS central unit not requiring bus transmission, or remote unit operation. These commands are normally used for satellite reconfiguration and other essential functions requiring a maximum of reliability.

MICROCATS provides a sample strobe interface for control of experiments and synchronization with the data acquisition sampling operation.

The MICROCATS memory unit provides the processing of deferred commands and/or the storage of a small amount of telemetry data for later transmission. This memory also allows uplinking of dynamic telemetry formats.

MICROCATS contains two interfaces which provide the serial bus interconnect between the MICROCATS central unit (MCU) and all MICROCATS remote data acquisition and command decoder units. The distributed serial bus interconnect architecture for remotes allows efficient distribution of MICROCATS remotes on both the rotor and stator segments of the LASSII satellite requiring a minimum number of interconnects across slip-ring interfaces.

*New MICROCATS Functions* — Three new interfaces are provided to MICROCATS to expand its capability for high rate data acquisition and encoding and add an additional uplink interface. The first of these, the Special Retrieval Interface (SRI) allows direct control by the MICROCATS microcomputer. The second is for control of the two ODETICS 5000 tape recorders. With this interface, the MICROCATS computer controls data recording and playback. A third interface allows an additional uplink command interface.

MICROCATS has an architecture very similar to most ground computer systems. This architecture allows the addition and change of interfaces with a minimum impact on the remainder of the system. By concentrating all possible functions in firmware rather than in hardware, it is possible to augment or redirect MICROCATS functions with a minimum of hardware redesign.

Interfaces are packaged one function per physical interface (where packaging efficiency permits). This allows the addition of new functions and interfaces by the addition of physical hardware interface boards to the MICROCATS mainframe package. The control store and variable store reserve in MICROCATS allows the addition of the tape recorder function and Special Retrieval Interface function with no major hardware changes to the control subsystem of MICROCATS. Table 5.3-4 details the telemetry rates.

Table 5.3-4 — LASSII Telemetry Rates

1. RECORD MODE - RETRIEVAL - CLOCK	262,144 Hz or 3.814 MHz
2. RECORDER CLOCK	268,865.6 Hz
3. WORD RATE - 8 BITS	$3.05175 \times 10^{-5}$ s
4. LINE RATE - 128 WORDS	$3.90625 \times 10^{-4}$ s
5. LINES PER SECOND	256 lines
6. WORDS PER SECOND	32,768 words
7. MAXIMUM RETRIEVAL TIME DATA < 256HZ	$7.3 \times 10^{-5}$ s
8. MAXIMUM RETRIEVAL TIME DATA > 256HZ	$2.0 \times 10^{-5}$ s
9. TELEMETRY FORMAT	256 bps 8196 bps
10. RECORDER PLAYBACK FORMAT	1.3 MHz
11. SYNCHRONIZATION TIME	$3.90625 \times 10^{-4}$ s

#### Telemetry Control Functions

The LASSII telemetry data acquisition process focuses around two primary functions. The first function, and that which dominates the telemetry rate problem, is that of acquiring high rate data from several of the LASSII experiments. Currently 14 different experiment sources require an aggregate

sampling rate of 210,944 bps. The remaining LASSII experiment packages have an additional 174 data sources which provide a low rate sampling aggregate of 21,280 bps. It is assumed that the number of sources and aggregate bit rates will change; however, it is assumed that the distribution between high rate and low rate experiment data is likely to remain at these ratios.

To most efficiently address this wide range of data acquisition functions the LASSII Telemetry and Command system has been divided into two data acquisition segments. The conventional MICROCATS telemetry function will accommodate the wide range of addresses required to perform the low rate experiment sampling. Existing format control techniques within MICROCATS will allow the sub-commutation necessary to access all 174 low rate experiment sources resulting in an aggregate low rate data acquisition of approximately 25 kbps.

*Special Retrieval Interface* — A new Special Retrieval Interface (SRI) has been added to the MICROCATS system to perform the high data rate experiment sampling function. Currently 14 addresses are required to specify the format for approximately 210 kbps of experiment data. The relatively low number of addresses required to sample this high rate data allows the construction of a simple high rate data acquisition scheme. The SRI design is PROM controlled and therefore allows a large amount of flexibility in format encoding.

#### Command and Control Functions

The command and control functions of the LASSII MICROCATS are illustrated in Fig. 5.3-3. LASSII is capable of receiving and processing commands from two sources, commands relayed via the TDRSS satellite and direct uplink commands from NRL ground stations.

Once a command has been decoded from either of the uplink sources, MICROCATS will determine if it is to be executed immediately or if it is to be loaded into the MICROCATS memory for deferred (indirect) execution.

If the command is of the immediate type, it will next be determined if it is a command to be relayed to its destination via a remote command decoding unit, or if the command will be executed via a direct link to either the Attitude Control computer, the Special Retrieval Interface, or as a critical command.

For commands executed through remote command decoders, two classes of commands are possible, discrete (single bit assertion commands) or serial data commands. Serial data commands allow the transmission of 16 bits of serial data to the selected command address.

Sixty-four critical commands are provided by MICROCATS. These commands represent the shortest hardware path through MICROCATS and are normally used for execution of configuration change or redundancy control commands.

The interface between the MICROCATS central unit and the Special Retrieval Interface is a direct command link that allows immediate control of SRI microcode.

The direct computer to computer link between MICROCATS and the Attitude Control Computer allows direct transmission of attitude control commands to that subsystem. This command link will also allow the immediate transferral of data base information from the ground to the Attitude Control System computer.

MICROCATS command formats allow the encoding of commands which are received and stored in the command system memory to be retrieved later at specified time intervals for delayed execution in modes similar to immediate uplink commands.



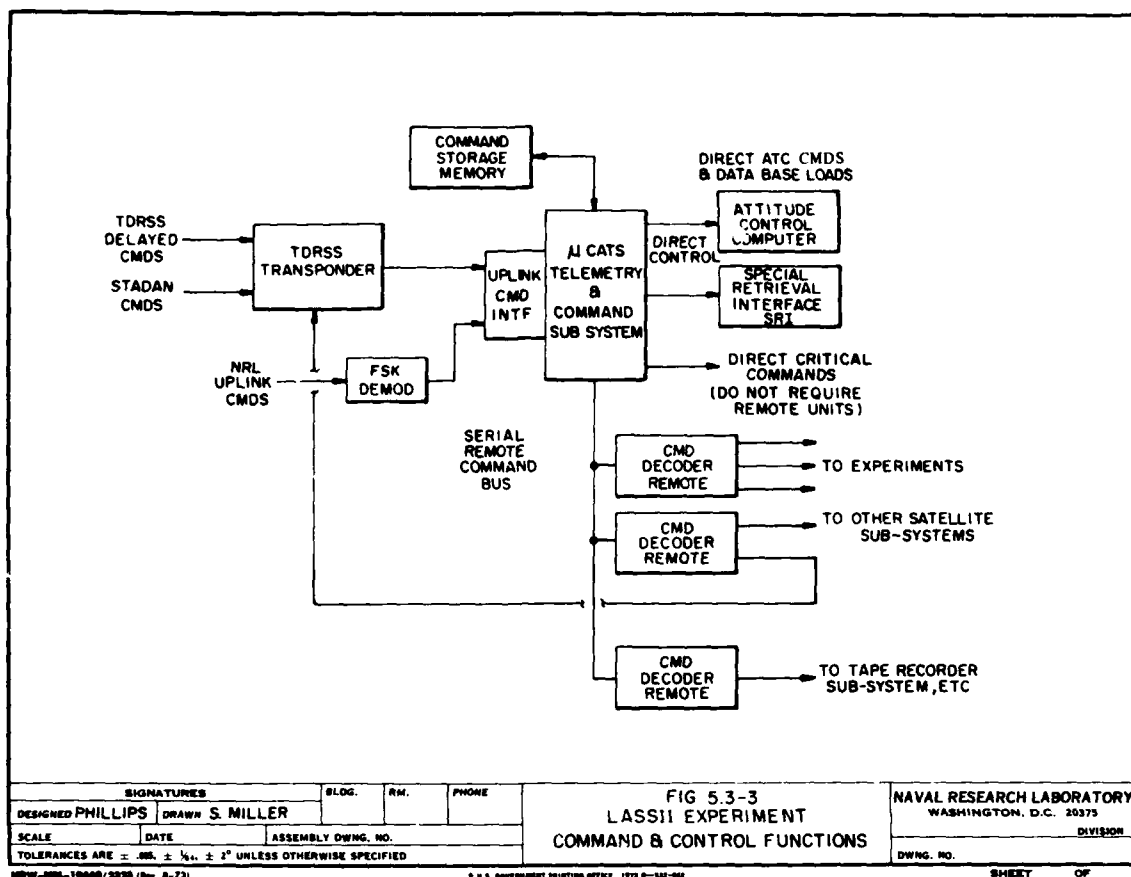


Fig. 5.3-3 — LASSII experiment command and control functions

As all command processing and decoding is firmware controlled within MICROCATS, new command types can be defined and implemented in the LASSII spacecraft with a minimum of hardware changes.

### 5.3.2 Experiment Interfacing

The LASSII spacecraft contains a nucleus of 15 separate scientific experiments. By dividing sampling requirements by rates, such that low data rate accessing is defined as any data point which requires sampling at less than 256 samples per second and high rate data sampling as any process requiring sampling rates in excess of that, a clear functional distribution evolves. Of the 15 experiments, only 6 require high data rate servicing. To service all high data rate experiments requires 14 data addresses. These 14 data addresses account for approximately 231 kbps of data sampling bandwidth. All 15 experiments require low data rate sampling with approximately 172 low rate addresses required for approximately 24.9 kbps of sample rate.

It is desirable to minimize the number of data and bus lines required to effect data transfer in the LASSII satellite because of the distribution of experiments in both the rotor and stator. The number of lines crossing the rotor-stator interface is minimized as these lines must be implemented with slip-rings. The LASSII experiment interconnect will require only 4 lines to accomplish all low rate data acquisition activities and approximately 20 lines to accomplish all high data rate transmission.

Figure 5.3-4 illustrates the experiment interface with the telemetry data acquisition function. As seen in the left of Fig. 5.3-4 the number of lines required to cross the spinning interface for the low-speed data acquisition function is represented by two pair of twisted serial buses. This serial bus interfaces with MICROCATS remote units in the proximity of each of the experiments allowing the relatively higher number of experiment to remote unit interconnects to occur over short distances. The MICROCATS remote units also allow transmission of both discrete and serial command information directly to the experiments by relaying this information from the MICROCATS central unit (again using the serial bus interconnect).

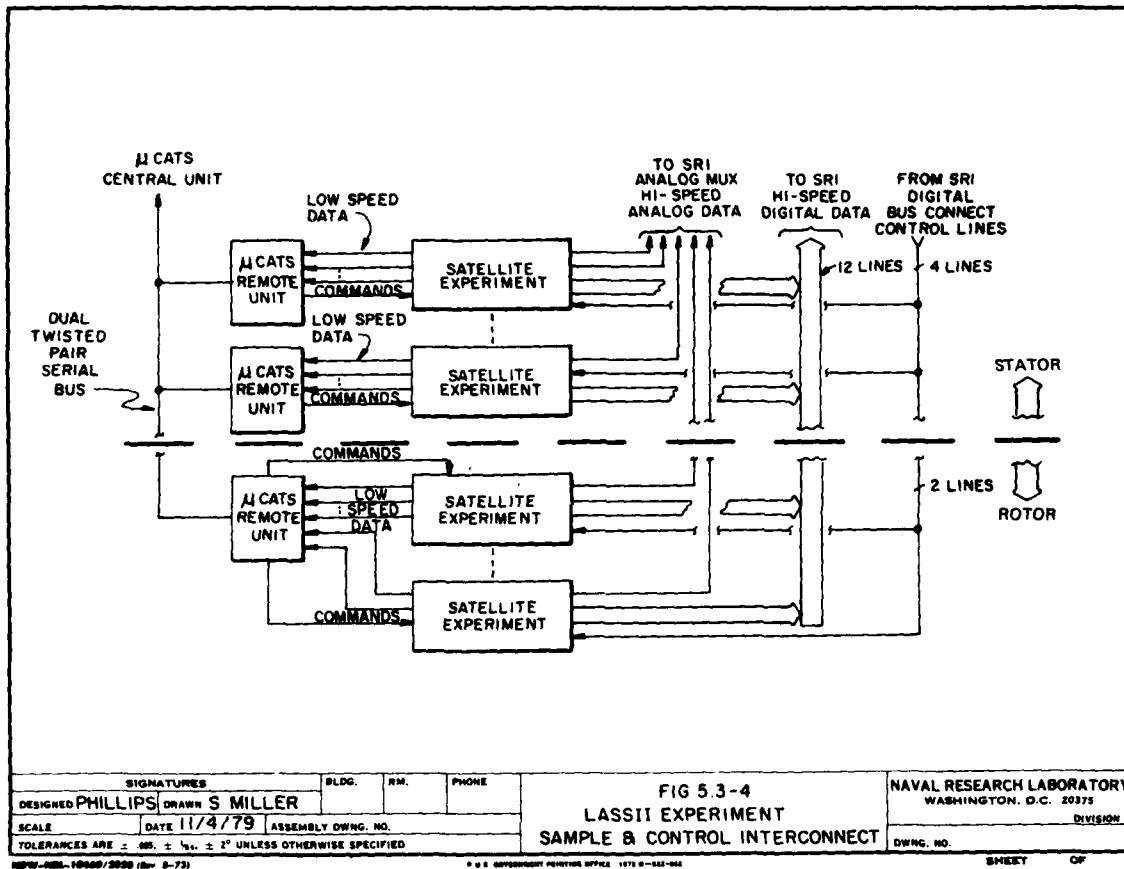


Fig. 5.3-4 — LASSII experiment sample and control interconnect

The high-speed data acquisition function is represented on the right of Fig. 5.3-4. Illustrated are both the analog and the digital data inputs. Analog sample points will be transmitted directly from their origin in the satellite experiment to the analog input multiplexer in the Special Retrieval Interface. Currently less than eight of these high-speed analog lines have been defined for the LASSII experiment complement. High-speed analog lines require no addressing information be transferred to the experiment as these lines are selected internally in the SRI.

High-speed digital data requires address information from the SRI to the satellite experiments. If the number of high-speed direct digital inputs remains at its current small figure, the SRI will provide

individual address select lines to each experiment address capable of sourcing high-speed digital data. The satellite experiments need only monitor the address select line (which can also be used as a power strobe) and, when active, place its digital data on the high-speed tri-state digital data bus. If the number of high-speed digital channels is to increase past 4, 4 to 16 line decoders will be interfaced at each satellite experiment to decode a 4-bit binary code to select a local address. In either of these techniques, only 4 address lines and 8 data lines will be required to interface the high-speed digital data with the Special Retrieval Interface. No hand-shaking protocol will be required for this digital data transmission (timing will be performed under SRI microcode control). The satellite need only tri-state its data upon recognizing its address select line assertion and must disconnect from the bus when its address selection is deactivated.

In summary, LASSII MICROCATS takes advantage of the fact that high-rate data are sourced from only a few experiment addresses which allows a simple high-speed data transfer path for high-rate experiment data. The more conventional low-rate sampling requirements are spread across a relatively large number of experiment addresses and can be accommodated by the flexibility and low to medium sampling rate capability existing in MICROCATS.

#### LASSII Experiment Format

A simulated LASSII format has been written. Included in the format are experiment data, house-keeping data, page/line counters, and sync words. The format was sized, with the  $P^3$  and E-field experiments operating in the high data rate mode, for 100 min. The  $P^3$  experiment uses 137,216 bps and the E-Field uses 36,868 bps. A total of 1,572,864,000 bits are accumulated in one orbit if all experiments are operated in the high data rate mode for 100 min. The format printout is available in a separate document.

#### User Telemetry Interface

The RIU retrieves four types of data as per NASA Remote Interface Specification (GSFCS-714-11) and Remote Interface Unit User Guide (GSFCS-700-54). The types of data which may be acquired, by NASA spec, are analog unipolar, passive analog, bilevel, and serial digital. The RIU also acquires analog bipolar and analog unipolar with five different input voltage ranges. Details are given in Table 5.3-5. Retrieved data are sent to MICROCATS and subsequently to the TDRSS transmitter or the tape recorder. MICROCATS controls the acquisition of data via the Supervisory Bus and the distribution of acquired data that have been transferred to the Reply Bus.

Table 5.3-5 — Telemetry Characteristics (per multiplexer)

Input Signal Type	Available Channels	Input Voltage Range (Vdc)	Maximum Source Impedance (k $\Omega$ )	Channel Input Impedance (M $\Omega$ )	Comments
Analog	0-63	0 to +5.1	5	Multiplexer ON > 1	Special enable available on Channels 0-15
Passive Analog	16-31	0 to +5.1	5	Multiplexer OFF > 10	1 mA $\pm$ 0.5% Current Source
Bilevel	0-63 in groups of 8	"1" = +3.5 to +1.5 "0" = -1.0 to +1.5	5		8 channels sampled sequentially, 256 kHz
Serial Digital	0-15	"1" = +2.4 to +1.5 "0" = -1.0 to +1.5	0.5		DATA-8 bits; CLOCK-256 kHz ENABLE-1 bit
Analog Unipolar	0-8	0 to +5 0 to +10	5 0 to 1000 Multiplexer	INPUT BIAS ON > 100 OFF > 100	CURRENT 100 nA
Analog Bipolar	0-8	$\pm$ 2.5 $\pm$ 5.1 $\pm$ 10	5 0 to 1000		

The RIU selects the input to be sampled, power strobes appropriate circuitry for processing, formatting, and transmission to MICROCATS over the Reply Bus.

### User Command Interface

The RIU also accepts commands via the Supervisory Bus and relays the commands to the spacecraft user. Each RIU has 63 channels available for discrete command distribution and 8 for serial digital command distribution. The RIU decodes which two types are to be performed from the command messages on the Supervisory Bus. The command messages also define the spacecraft user circuit address.

The RIU performs two spacecraft user functions in response to a discrete command message:

1. It closes one of 63 switches that are internal to the RIU, providing a selected output interface circuit with a dedicated path to RIU signal ground.
2. While this switch is closed, the RIU transmits a +28 V pulse on one of three outputs which appears for any command in the groups as shown:

62 lines-----Switch Closure to Signal Ground  
                   +28 V Pulse Bus  
 2 lines-----Channels 2 to 62 even only  
 2 lines-----Channels 1 to 47 odd only  
 2 lines-----Channels 47 to 63 odd only

The two functions may be used in any of several ways, depending upon the electrical connection of the user.

### Serial Digital

The RIU transmits four signals in response to a serial digital command message. The four signals are:

1. A switch closure to RIU signal ground (ENABLE).
2. A 16-bit command word (DATA).
3. A gated 256 kHz pulse train of 16 bits (CLOCK).
4. A positive pulse after the 16 bits (EXCUTE).

#### 5.3.3 Tape Recording Subsystem

A redundant tape recording system is provided with the LASSII MICROCATS to be used for storing experiment and housekeeping data. The tape unit selected is the ODETICS 5000. This tape recorder provides a total storage capability of  $1.67 \times 10^9$  bits per tape.

The ODETICS 5000 requires that MICROCATS format the data with 320 bit gaps for every 12,480 bits of data. A memory storage system has been designed to accomplish this.

When it is desired to play back the tape recorder, the commands will put the recorder in the proper mode and clock the data out at a rate of 1.3312 Mbps. Since the complete reel of data may not be able to be read out due to a constraint imposed by the TDRSS, the recorder will be stopped, then

rewound to a predetermined point. When the tape recorder is started again for a data dump, a logic circuit will not allow data to be transmitted until the point is reached where the preceding data were interrupted.

The bit rate as presented to the input of the interface unit is 262,144 bps. The bit rate out of the interface unit into the tape recorder is 268,865.6411 bps.

Several data recording speeds are selectable by the user with different recording time capacities. Current versions of the ODETICS 5000 allow recording rates of 134, 268, or 1331 kbps record rate. The playback rate is 1.3 Mbps. The 1.3 Mbps playback rate is appropriate for TDRSS relay satellite operations in the single access mode.

The ODETICS 5000 records only in the forward direction and plays back only in the reverse direction. This imposes a data organization constraint on MICROCATS such that synchronization patterns, frame counters, etc. are recorded backwards, so that during playback time these data items appear in the right sequence.

The two tape recorders included in the tape recording subsystem are to be configured such that one operates as a cold spare, not being called into operation unless failure is detected on the other unit. The tape recording subsystem will receive its control information directly from a MICROCATS remote command unit.

The ODETICS 5000 requires a precisely controlled clock waveform input to control its recording sequence. This clock will be generated externally by MICROCATS and will also be used to drive the serial data transfer from the Special Retrieval Interface to the tape recording system during recording operations.

Note that during dump (reproduce) operations, the ODETICS 5000 degaps tape records internally. This permits the reproduction of data directly into the TDRSS transponder without the need for tape degapping operations.

#### 5.3.4 Attitude Control Computer Interface

MICROCATS provides one or more interfaces which couple directly to a Texas Instruments ruggedized SBP 9900 microcomputer. This processor was chosen for spacecraft functions because of its  $I^2L$  technology and high-reliability fabrication techniques. It is a monolithic 16-bit computer on a single chip, and it possesses functions such as vectored interrupts and hardware multiply/divide. It also provides fourth generation architecture functions such as work space register files allowing extreme operating efficiencies in real time environments. This processor is currently being used at NRL for attitude control applications.

The interface between MICROCATS and the SBP 9900 is implemented by a direct interface on the MICROCATS bus, communicating with a seven-wire interface to the Communications Register Unit (CRU) interface on the SBP 9900. The CRU bus on the SBP 9900 allows efficient bidirectional 16-bit communications between the two subsystems using a minimum number of wires, interface circuitry, and protocol conventions. The interface allows bidirectional 16-bit data transfers coordinated by service requests on the MICROCATS end of the interface and SBP 9900 interrupts on the 9900 end of the interface.

All communications between the two processors are implemented with this seven-wire interface. All data content is specified by firmware in the two processors. This interfacing technique allows the same hardware interface to be used for any number of data transfer functions between the two processors.

Uplink control of the attitude control system can be accomplished directly by sending commands to MICROCATS addressed for transfer to the Attitude Control Computer. This same uplink transfer capability can be used for data base and other operational information loads from the ground to the Attitude Control Computer.

A particular advantage of having the Attitude Control Computer directly interfaced to the MICROCATS occurs by allowing the Attitude Control Computer to request MICROCATS to perform its data acquisition and command execution functions. These requests by the Attitude Control Computer are time interleaved with normal telemetry operations on its data acquisition and command buses. By use of this technique, I/O operations can be performed almost entirely by existing MICROCATS components.

As the MICROCATS to SBP 9900 interface is self contained on a single interface board, more than one of these interfaces can be implemented for use on LASSII spacecraft should the need arise for additional computer control in any of the LASSII applications.

## 5.4 Attitude Control System

### 5.4.1 Requirements

#### Attitude Control Requirements

The current LASSII mission supports 15 core experiments. When experiments are in progress the rotor scans at a nominal rate of 3 rpm (scan rates are selectable from 0 to 20 rpm) and maintains its axis normal to the orbit plane. Concurrently the stator is three-axis stabilized with the ram face oriented perpendicularly to the velocity vector. The stator is torqued at a rate of one revolution per orbit to maintain a locally vertical reference.

Since the ACS requirements are driven by the Ion Drift Meter (IDM) experiment, a review of ACS requirements was made with IDM experimenter participation. It was determined that the ACS requirements in Table 5.4-1 would adequately support the IDM experiment and still be consistent with the remaining instrument needs.

Table 5.4-1 — ACS Requirements

#### Attitude Measurement

Roll	$\pm 1.0^\circ$
Pitch and Yaw	$\pm 0.5^\circ$

(See text for  $\pm 0.20^\circ$  capability)

#### Attitude Stability

Maximum Rate, All Axes	$\pm 0.4^\circ/\text{min}$
Control, All Axes	$\pm 1.0^\circ$

#### Orbit Control Requirements

The LASSII Spacecraft is to be deployed from the Space Shuttle Orbiter. While the Orbiter remains on station, LASSII will be placed in predefined positions relative to the Orbiter to permit phased measurements of ionospheric characteristics by experiments on board both LASSII and the Shuttle. At the conclusion of the experiment LASSII will be maneuvered to return to the vicinity of

the Orbiter where the spacecraft is retrieved (using the remote manipulator system (RMS)) and returned to Earth.

The normal duration of a manned Orbiter mission is considered to be 7 days. Of this period, the first and last days are required for prerelease and retrieval operations, respectively. This leaves 5 days for experimentation and Orbit maneuvers. (As previously noted, missions up to 30 days can be accommodated in the current design.)

Two types of LASSII missions have thus far been defined. These are known as the Tandem Orbit Mission and the Continuous Overflight Mission.

#### Tandem Orbit Mission

The Tandem Orbit Mission consists of placing the LASSII spacecraft coorbital with the Shuttle Orbiter but lagging in position by a specified amount. Hohmann maneuvers can establish several different lag positions in a given mission. With the Orbiter in a 90-min parking orbit (148.2 nmi circular) LASSII may be directed typically to 5, 10, and 20 min lag positions. The spacecraft fuel capacity is sized to achieve a maximum  $180^\circ$  phase separation between Orbiter and spacecraft (i.e., 5, 15, 45 min lag positions).

For purposes of fuel budget calculations experiment observation time at each of these lag positions is assumed equal and maximized for a given mission. Successive positions in the Tandem Orbit Mission are achieved through in-plane  $\Delta V$  burns along the velocity vector occurring at identical positions in the orbit.

Figure 5.4-1 illustrates the procedure used to achieve successive lag positions in the Tandem Orbit Mission.

For example, with the Orbiter in a 90-min orbit, if it is desired to place the payload at the 5-min lag position, a burn into a 91-min transfer orbit will achieve the desired spacing in five laps of the payload.

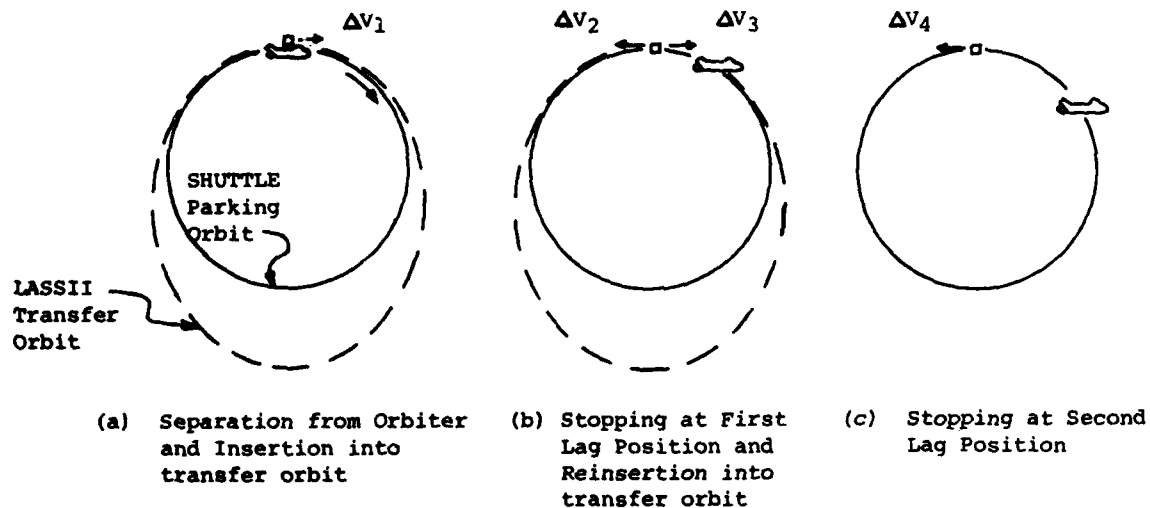


Fig. 5.4-1 — Tangential maneuvers for Tandem Orbit Mission

When the required laps have been completed the payload executes a stopping maneuver  $\Delta V_2$  which is equal in magnitude to  $\Delta V_1$  but opposite to the velocity vector. The payload is again coorbital with the Orbiter but lags by the requisite spacing as shown in Fig. 5.4-1(b). After completing the experimental phase the payload executes orbit change and stopping maneuvers  $\Delta V_3$  and  $\Delta V_4$  for transfer to the next lag position.

Return of the payload to the vicinity of the Shuttle Orbiter for retrieval is accomplished in a similar maneuver. Since the payload must now make up for the cumulative phase lag previously introduced, the payload is inserted into a transfer orbit with period shorter than the Orbiter period. When, after an integral number of orbits, the payload returns to the vicinity of the Orbiter, a stopping maneuver is executed making the two vehicles again coorbital. The payload is then in position to begin retrieval maneuvers.

### Continuous Overflight Mission

The Continuous Overflight Mission differs from the Tandem Orbit Mission in that the LASSII payload is not coorbital with the Shuttle during the on-station experiment phase but moves in an elliptic orbit relative to the Orbiter with a period equal to the Orbiter period.

The desired relative motion is achieved by the payload executing a radial (Crocco) maneuver which causes its orbit to deviate from that of the Shuttle Orbiter as shown in Fig. 5.4-2(a). The radial spacecraft maneuver does not alter the orbit period, so that the relative orbit between the two is a stationary ellipse as shown in Fig. 5.4-2(b).

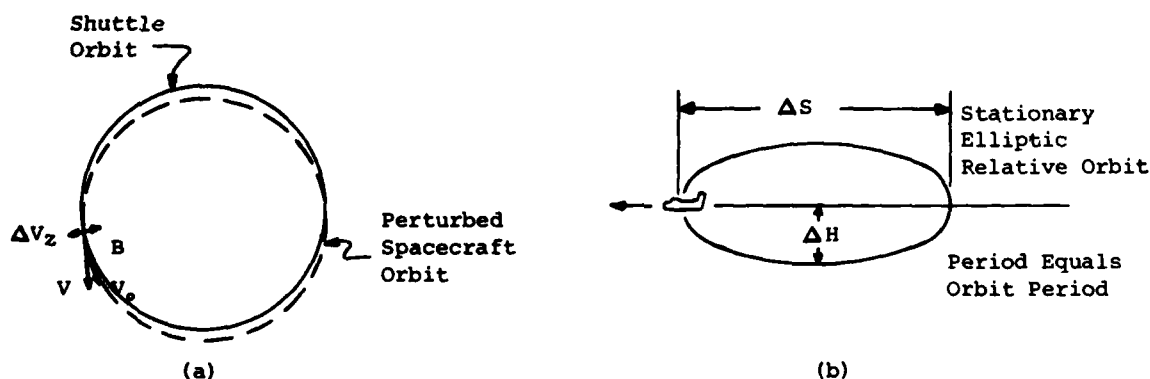


Fig. 5.4-2 — Radial (Crocco) maneuver for Continuous Overflight Mission

Many LASSII missions require continuous overflight rather than tandem operations with a possible scenario involving the Shuttle in a 160 nmi altitude circular parking orbit for the duration of the Continuous Overflight Mission. The amplitude of the radial burn  $\Delta V_z$  might typically be adjusted to provide an altitude deviation  $\Delta H$  of  $\pm 25$  nmi relative to the orbiter. The maximum altitude deviation anticipated for a given Continuous Overflight Mission is  $\pm 50$  nmi.

Performance of a Continuous Overflight Mission assumes that the spacecraft maneuvers once into a particular relative elliptic orbit and all experiment data are taken without further spacecraft maneuvering. At the conclusion of ionospheric observations the spacecraft executes an equal but directionally opposite radial maneuver when returning to the vicinity of the Shuttle. This maneuver again makes the spacecraft coorbital with the manned vehicle, and retrieval operations can then be initiated.



#### 5.4.2 ACS Configuration

A number of different approaches were examined for implementing an attitude control system for the LASSII spacecraft. Three separate approaches to attitude control were considered. These were rotor stabilization, bias momentum stabilization, and MMS zero momentum stabilization. A comparison of the three alternative ACS approaches led to the selection of the bias momentum technique.

The bias momentum approach incorporates a momentum wheel with integral IR horizon scanner for improved gyroscopic stiffness and attitude reference. Two such units are provided for full redundancy although ACS will function with just one scan wheel operating. Momentum wheels are mounted on the stator with spin axes parallel to the rotor shaft axis. The rotor, which has two separate drums attached through a common shaft, supplements the wheel momentum for increased stiffness.

The momentum wheel provides control in two axes. The third axis is stabilized by addition of a reaction wheel. Wheel momentum dumping is performed by  $N_2H_4$  thrusting.

Aside from the improved gyroscopic stiffness, the primary advantages of the approach lie with its greater pointing accuracy and potential growth capability for handling future missions. With this configuration the rotor payload may be reduced in weight considerably thereby relieving load requirements on the rotating mechanical assembly.

#### 5.4.3 ACS Implementation

The attitude control system of the LASSII spacecraft provides for the following functions:

- Attitude Control — Maintain stator RAM face perpendicular to velocity vector within specified rate and position tolerances.
- Spin Axis Control — Control and monitor rotor spin rate and maintain spin axis perpendicular to orbit plane. Damp spin axis oscillations. Rotor spin rate to be determined by experiment scan requirements.
- Precision  $\Delta V$  Burn Control — Orient and maintain spacecraft attitude for in-track, radial, or cross track maneuvers. Included is measurement and integration of sensed acceleration (velocity metering) and stored command capability.
- Wheel Momentum Unloading using thruster pulsing.
- Compensation for Aerodynamic Effects — Provide automatic pulse torquing regime to counter aerodynamic torquing and drag perturbations. Computer software includes atmosphere and spacecraft models and accepts orbit ephemeris updates and operator inserted trims.
- Attitude Reference — Provide telemetered measurements of spacecraft orientation and rates plus TDRSS position determinations to support LASSII experiments.
- Stator/Rotor Interface — Provide Rotating Mechanical Assembly (RMA) including electrical power and signal paths between rotor and stator.
- Shuttle Deployment — Facilitate rapid deployment, orbit transfer, and retrieval of the vehicle.

Resistance to disturbances affecting spacecraft attitude is provided by:

- Pitch Momentum Wheel. Either one or two wheels may be used. Total momentum capability is 30 to 50 ft-lb-s. Provides stabilization in roll/yaw.
- Rotor Momentum. Inertia of spinning double rotor section provides additional gyroscopic stiffness with pitch axis momentum of 30.5 ft-lb-s.
- Pitch/Roll Reaction Wheel. Wheel mounted with axis along z axis, provides stabilization in pitch/roll.

The sensing elements used as attitude reference are as follows:

- IR Horizon Scanners. Two sensors are required for redundancy. An option exists for having the IR scanners integral with the pitch momentum wheel or as independent scanners. Integral scanners offer potential savings in power and eliminate two rotating components. The disadvantage is that the pitch wheel chosen may not have sufficient capability in a future application thereby necessitating scan wheel redesign costs. With independent scanners the pitch wheel may be upgraded without effecting the Earth sensors, thereby offering greater design flexibility and potential cost savings. IR accuracy of  $0.1^\circ$  may be expected by use of available products.
- Coarse Sun Sensor. This is a  $360^\circ$  f.o.v. 5 eye Adcole mounted on the stator section.
- Fine Sun Sensor. Precision two-axis static sun sensor mounted on the stator section provides attitude reference in roll and yaw.
- Magnetometer. Provides three-axis attitude reference by measurement of Earth magnetic field components in conjunction with ground processing of data with field model.
- Three-Axis Accelerator Package. For  $\Delta V$  control and drag measurements.
- Rate Integrating Gyro. Two-axis unit provides short-term attitude reference in pitch and yaw. Used for pitch axis slew of stator for radial and negative in-track orientation maneuvers, yaw axis slew for cross track burns. Gyro updates by IR and Fine Sun Sensors. Also used for retrieval operations together with magnetometer and 5 eye.

A block diagram of the ACS is given in Fig. 5.4-3. A weight and power analysis is provided in Table 5.4-2.

The operations performed by the ACS begin with deployment of the spacecraft from the STS. After LASSII has been deployed the ACS will, under initial ground command, acquire its desired mission orientation, begin rotor operation, and activate the control wheels. Upon completion of attitude acquisition and stabilization the spacecraft is available to begin large  $\Delta V$  burns in support of mission requirements.

When the LASSII spacecraft is in an operations phase, the ACS will maintain the attitude required. When the wheel momentum builds up to a predetermined level and when thrusting is permitted (i.e., during either a mission lull in which experiments are nonoperational or during a low-altitude operation when thrusting is required) the ACS will initiate momentum dumping using the thrusters, maintain attitude, and terminate momentum dumping in preparation for experiment reactivation.

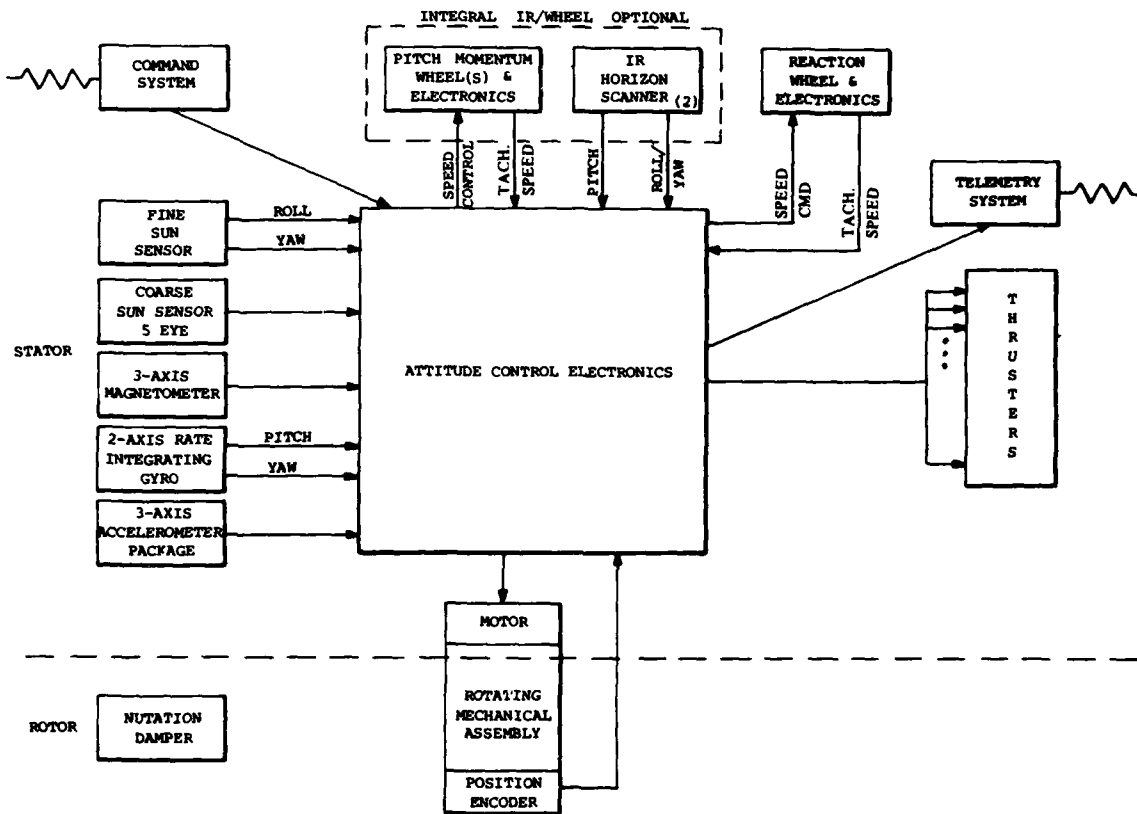


Fig. 5.4-3 - ACS

Table 5.4-2—ACS Weight and Power

Component	Weight (lb)	Peak PWR (W)	AVG PWR (W)	Total Mission PWR Estimate (%)	Total Average Power (W)
Attitude Control Electronics	12	10	10	100	10
Momentum Wheel and Electronics	78	88	8	95	7.6
IR Scanners	9	12	12	95	11.4
Reaction Wheel and Electronics	12	5	2	95	1.9
RMA	38	46	15	95	14.25
Fine Sun Sensor	4	1	1	95	0.95
Coarse Sun Sensor	3	1	1	100	1
Magnetometer	1	1	1	100	1
RIG	3	6	6	100	6
Accelerometer	3	1	1	95	0.95
RCS	RCS Budget	20	15	1	0.15
Total	163		72		55.2
Potential Savings with Integral IR/Momentum Wheel	38		5		4.75
Total	125		67		50.45

The accelerometers will be used to precisely control  $\Delta V$  burns and to measure atmospheric drag so that appropriate action can be taken to restore the spacecraft orbit with a minimum of ground interaction.

The ACS will also accomplish the functions of rendezvous and retrieval. The rendezvous operation will be initiated by ground command. The information on the orbit will be processed on the ground and the required spacecraft maneuvers sent to the ACS. The ACS will perform the commanded maneuvers required to place LASSII in an orbit for convenient STS retrieval.

When the spacecraft is sufficiently close to the Orbiter the ACS will be placed in a minimal power mode that will consist of: Rotor stopped, Momentum and Reaction Wheel off, IR, and fine sun sensor off. Attitudes rates will be minimized by using RIG outputs updated by coarse sun sensor and magnetometer.

Retrieval will be accomplished by the manned Orbiter approaching LASSII and grappling the powered down spacecraft with the remote manipulator system. All spacecraft systems are turned off when stored in the cargo bay.

#### 5.4.4 Disturbance Analysis

To size the bias momentum stabilized attitude control system it was necessary to evaluate the order of magnitude of the various disturbances affecting wheel momentum buildup.

In the absence of thruster firings a spacecraft will continue in an elliptic orbit with Earth center as perifocus. Disturbances to the wheel spin axis attitude will come from the following sources:

- (1) Orbit precession
- (2) Aerodynamic torques
- (3) Residual magnetic moments
- (4) Solar radiation
- (5) Gravity gradient

Estimates of the aerodynamic disturbance torque as a function of altitude for the current LASSII spacecraft configuration are presented in Table 5.4-3. The range of altitude covers the operational extremes of anticipated LASSII missions.

Table 5.4-3 — Aerodynamic Torque as a Function of Altitude

Altitude (nmi)	Density $\rho$ (slugs/ft <sup>3</sup> )	Velocity, $V$ (ft/s)	$1/2 C_D A_l$ (ft <sup>2</sup> )	Aerodynamic Torque, (ft-lb)
210	$10 \times 10^{-15}$	25004	53	$3.3 \times 10^{-4}$
200	$14 \times 10^{-15}$	25074	53	$4.7 \times 10^{-4}$
180	$30 \times 10^{-15}$	25214	53	$1.0 \times 10^{-3}$
160	$70 \times 10^{-15}$	25354	53	$2.3 \times 10^{-3}$
140	$160 \times 10^{-15}$	25495	53	$5.5 \times 10^{-3}$
120	$300 \times 10^{-15}$	25637	53	$1.0 \times 10^{-2}$
110	$600 \times 10^{-15}$	25708	53	$2.1 \times 10^{-2}$

All of the estimated disturbance torques acting to precess the spacecraft momentum axis are summarized in Table 5.4-4. Clearly the predominant disturbance is aerodynamic at all positions in orbit. In light of this, particular care is given to minimizing the displacement between center of pressure and center of mass. This requirement becomes even more significant for measurements that are made at the lower altitude extremes (below 140 nmi).

Table 5.4-4 — Momentum Axis Attitude Disturbance Summary

Source	Disturbance Torque (ft-lb)
Earth Oblateness	$1.1 \times 10^{-4}$
Aerodynamic	$3.3 \times 10^{-4}$ @ 210 nmi $2.3 \times 10^{-3}$ @ 160 nmi $2.1 \times 10^{-2}$ @ 110 nmi
Residual Magnetic	$2.0 \times 10^{-6}$
Solar Radiation	$1.9 \times 10^{-6}$
Gravity Gradient	nil

#### 5.4.5 Angular Momentum Sizing of Reaction and Momentum Wheels

Wheel sizing is primarily determined by the magnitude of the environmental disturbance torques. As determined in the previous section, the dominant disturbance torque is due to aerodynamic pressure unbalance. This unbalance produces torque components along both the roll and pitch axes. Because the ram face is always pointed into the wind both disturbance components will be unidirectional in the rotating local vertical frame and tend to cause a steady increase in wheel momentum buildup over time. The magnitude of torque increases as the lower altitude extreme of 110 nmi is approached and this is the predominant factor in sizing the momentum wheel.

Table 5.4-5 shows the relationship of altitude and required pitch momentum for a 0.4 deg/min spin axis precession.

Table 5.4-5 — Required Pitch Wheel Momentum as a Function of Altitude  
To Limit Spin Axis Precession to 0.4°/min Without Counteractive Torquing

Altitude (nmi)	Max Disturbance Torque, $T_z$ (ft-lb)	Max Allowable Precession Rate, $\phi$ (rad/s)	Total Momentum $H_T = T_z/\phi$ (ft-lb-s)	Rotor Momentum $H_R$ (ft-lb-s)	Req'd Wheel Momentum $H_w = H_T - H_R$ (ft-lb-s)
210	0.00044	$1.16 \times 10^{-4}$	3.8	30.5	—
200	0.00048	$1.16 \times 10^{-4}$	4.1	30.5	—
180	0.00111	$1.16 \times 10^{-4}$	9.6	30.5	—
160	0.00241	$1.16 \times 10^{-4}$	20.8	30.5	—
140	0.00453	$1.16 \times 10^{-4}$	39.0	30.5	8.5
120	0.00880	$1.16 \times 10^{-4}$	75.9	30.5	45.4
110	0.01670	$1.16 \times 10^{-4}$	144.0	30.5	113.5

By interpolation we see that the rotor momentum alone is sufficient to stabilize against the maximum disturbance torque down to an altitude of 150 nmi. Below 150 nmi additional momentum along the pitch axis is required to limit precession rates to the specified allowable maximum of 0.4°/min. Wheel momentum size is driven by the maximum aerodynamic disturbance and rises rapidly as perigee altitude decreases. Without counteractive thrusting to balance against the peak aerodynamic torques, a momentum wheel of 113.5 ft-lb-s would be required to limit precession to 0.4°/min at 110 nmi altitude.

The required wheel size can be reduced if thrusting in a direction to oppose the aerodynamic torque at altitudes below 140 nmi is permitted. Assuming two 0.2 lbf BOL attitude jets each at 20 inch moment arms provides a control torque of 0.67 ft-lb. Comparing to the peak disturbance torque of 0.0167 ft-lb at 110 nmi, a maximum 2.5% pulse duty cycle at BOL would be required to counterbalance aerodynamic disturbances. The duty cycle would increase to a maximum of 7.5% as delivered thrust decreases with fuel depletion. Since the LASSII spacecraft is required to enter the region of atmosphere below 120 nmi altitude it will not be possible to eliminate thruster pulsing during orbits for data acquisition. In this case perigee  $\Delta V$  is needed to counter the significant drag at these altitudes in order to preserve the orbit relative to the shuttle. Since pulsing is required at lower altitudes to compensate for drag forces, pulsing will also be permitted to reduce required wheel momentum. Dumping of wheel momentum, when possible, will be executed at intervals selected to have minimum impact on data acquisition.

#### 5.4.6 Thruster Sizing Considerations

Thrusters for the LASSII spacecraft were selected to perform the following functions:

- Three-axis attitude control of stator section
- Wheel momentum unloading

- Counteractive thrusting against aerodynamic torque
- Aerodynamic drag compensation
- Large  $\Delta V$  orbit transfer maneuvers
- Acquisition/reacquisition precession maneuvers
- Spacecraft retrieval operations

Monopropellant hydrazine  $N_2H_4$  at an ISP of 225 lb-s/lb is assumed. The fuel system is  $N_2$  pressurized at 250 psi with a 3:1 blowdown ratio so that engine thrust at EOL is one third that at BOL.

Selection of thrusters is strongly influenced by qualification data, performance history, production cost, and reliability considerations in addition to functional size requirement. For these reasons hydrazine jets with BOL thrust levels of 0.2 lbf and 5.0 lbf are preferred to support the LASSII mission.

#### **Counteractive Thrusting Against Aerodynamic Torque**

The maximum aerodynamic torque acting on the spacecraft occurs at 110 nmi altitude and is oriented along the  $z$  axis. The magnitude of this component has previously been calculated to be 0.0166 ft-lb. Two 0.2 lbf BOL attitude control jets, each at 20 inch moment arms provide a control torque of 0.67 ft-lb, more than adequate to counterbalance the disturbance. The pulse duty cycle is 2.5% at BOL and rises to 7.5% for EOL.

To preserve the spacecraft orbit, thrusting along the  $x$ -axis when in the lower orbit extremes will be required to compensate for aerodynamic drag. This may be accomplished by firing the 0.2 lb or 5 lb thrusters. Thrusters will be fired in pairs to provide pure translation. When firing the smaller thrusters, the maximum duty cycle is 9.4% at BOL, and increases to 28.2% at EOL. Using a pair of 5 lb thrusters, maximum duty cycle is 0.37% BOL and 1.12% EOL.

#### **Large $\Delta V$ Orbit Transfer Maneuvers**

For purposes of approximate sizing and illustration it is assumed that for any single  $\Delta V$  burn a maximum fuel consumption of 100 lb is permitted. If maneuvers are restricted to a maximum 20 deg burn arc to approximate impulsive thrusting, then for a 90 min orbit the delivered thrust must exceed 75 lbf.

The most convenient available engine meeting this requirement delivers 150 lb thrust BOL. Two qualified thrusters are available in this size. With a 3:1 blowdown system EOL thrust falls to 50 lb. As this condition is approached the allowable fuel consumption per burn may be somewhat reduced.

#### **Acquisition/Requisition Precession Maneuvers**

The spacecraft must have the capability of reorienting the pitch axis without turning off the momentum wheel or stopping rotor spin. Such requirements may occur during acquisition or reacquisition of an orbit attitude.

To precess about yaw, two 0.2 lbf jets are fired providing a precession rate of 1.20 deg/s BOL.

To precess about roll either 0.2 or 5.0 lbf jet pairs may be fired providing precession rates of 0.53 or 13.35 deg/s, respectively.

#### **Retrieval Operations**

Retrieval operations are concerned with the minimum angle and displacement correction capability to place the spacecraft at the proper attitude and position for grappling by the RMS.

The spacecraft will be driven to the vicinity of the Orbiter in a momentum stabilized condition. By use of a pair of 0.2 lbf thrusters, velocity may be controlled to better than  $0.25 \times 10^{-3}$  fps. Attitude is controlled to  $\pm 1.0$  deg.

When the spacecraft arrives at the vicinity of the Orbiter, wheel and rotor speed is removed. Attitude thrusting is then performed by using the rate integrating gyros for reference. Sun sensor and magnetometer are used to update the gyro. Attitude and velocity are controlled to the same precision as in the momentum stabilized condition except for errors introduced by the magnetometer and gyro bias drift.

Spacecraft translation is to be achieved by jets oriented on the +X axis. Non +X displacement is obtained by orienting the spacecraft X-axis in the direction of desired motion and pulsing. Obviously the LASSII spacecraft cannot be completely driven to the retrieval point since reorientation must cease when the arm is extended. The spacecraft will be driven as close as practical to the manned Orbiter with the astronauts providing the final maneuvers of Shuttle and arm to achieve retrieval.

#### 5.4.7 Thruster Configuration

The thruster configuration for the LASSII spacecraft is indicated in Fig. 5.4-4. There are twelve 0.2 lb thrusters, four 5 lb thrusters, and a single 150 lb main engine. All thrusters are mounted on the rear side of the spacecraft opposite the ram face and grouped in clusters designated A-D.

The functional role of the 0.2 lb engines is to provide attitude and small velocity corrections. The functions are as to jet combinations in Table 5.4-6.

The 5 lb engines are utilized for medium size maneuvers and stabilization during large disturbances occurring at low altitudes or during main engine firing. In the event of a main engine failure the 5 lb engines may be used to retrieve the spacecraft.

Table 5.4-7 presents a thruster function matrix indicating how each spacecraft ACS function is to be controlled.

#### 5.4.8 Mission Analysis

##### Continuous Overflight Mission

Requirements for the continuous overflight mission have been discussed in Section 5.4.1. In this section we present results for two overflight missions with  $\Delta H$  of 25 and 50 nmi.

The continuous overflight mission is initiated by execution of a radial burn to obtain a stationary elliptic orbit relative to the Shuttle as shown in Fig. 5.4-2. The radial burn may be performed in stages on successive orbits to approximate an impulsive perturbation. Staged burns must be performed at identical points in the satellite orbit.

Continuous overflight missions are designed to measure ionosphere properties at different altitude levels. We assume STS Orbiter operation at 160 nmi. Mission 1 requires transfer of the LASSII spacecraft to a  $135 \times 185$  nmi orbit.

Table 5.4-8 presents a summary of the Mission 1 essentials. It includes the mission parameters, burn requirements, available observation time, and fuel budget.

Mission 2, with LASSII in a  $110 \times 210$  nmi orbit, is similarly analyzed in Table 5.4-9.



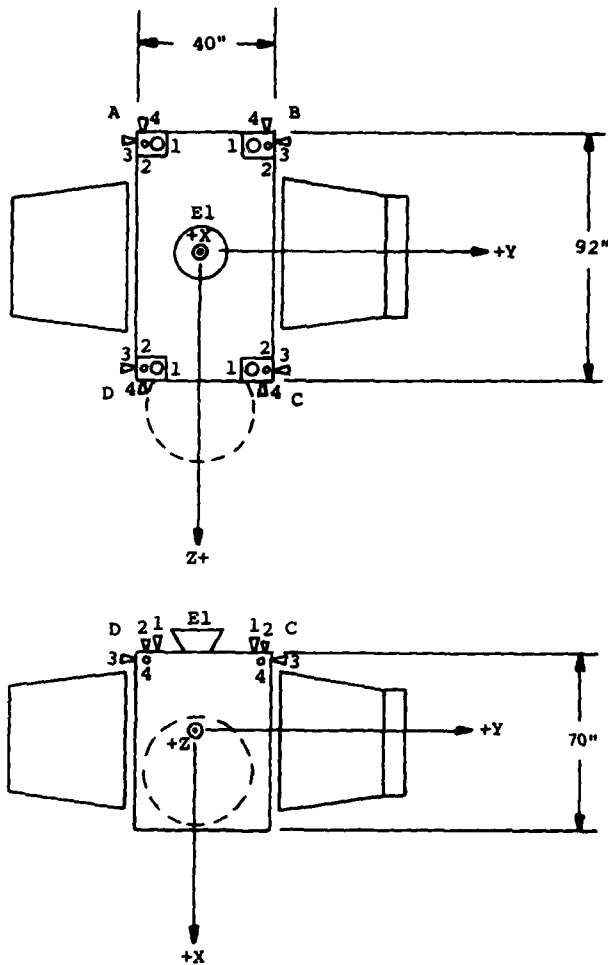


Fig. 5.4-4 — LASSII thruster configuration

Table 5.4-6 — Functional Role of Small (0.2 lbf) Thrusters

Function	Primary	Backup	Reorientation
+ROLL	A3,C3	B4,D4	
-ROLL	B3,D3	A4,C4	
+PITCH	C2,D2	A4,B4	
-PITCH	A2,B2	C4,D4	
+YAW	A2,D2	B3,C3	
-YAW	B2,C2	A3,D3	
+X	A2,C2	B2,D2	
-X	A2,C2	B2,D2	180° about pitch
+Z	A2,C2	B2,D2	-90° about pitch
-Z	A2,C2	B2,D2	+90° about pitch
+Y	A2,C2	B2,D2	90° ROLL, then +90° about pitch
-Y	A2,C2	B2,D2	90° ROLL, then -90° about pitch

Table 5.4-7 — Thruster Function Matrix

Function		0.2 lb Engines												5 lb Engines				150 lb Engine
		A2	A3	A4	B2	B3	B4	C2	C3	C4	D2	D3	D4	A1	B1	C1	D1	E1
Attitude Control																		
Roll	P			X			X			X			X					
	B				X			X			X			X				
Pitch	P	X			X			X			X							
	B			X			X			X				X				
Yaw	P	X			X			X			X							
	B		X			X			X			X						
Translation Small ΔV																		
Small	P	X						X										
	B				X					X								
Med	P													X		X		
	B														X		X	
Large ΔV																		
	P																	X
	B													X	X	X	X	
Momentum Unloading		P	X		X													
	B								X			X						
Drag Compensation																		
	P	X						X										
	OR													X		X		
	B				X						X							
	OR														X		X	
Stab. During Main Engine Thrusting														X	X	X	X	
Precession Maneuvers																		
Yaw slew	+					X						X						
	-		X						X									
Roll slew	+	X									X							
	OR													X			X	
	-				X			X										
	OR														X	X		
Retrieval		X	X	X	X	X	X	X	X	X	X	X	X	X	X	X	X	X

P - primary  
B - backup

Table 5.4-8 — Mission 1 Summary

Mission 1 Continuous Overflight Mission: 160 ± 25 nmi							
Payload WT	3062 lb						
Orbit Parameters	Size: 135 × 185 nmi	Semi-Major Axis: 3603.923 nmi					
	Period: 90.44525 min	$\Delta H$ 25 nmi					
	ECCEN: 0.006937	$\Delta S$ 100 nmi					
Major $\Delta V$ Burns	Type	Rev	$\Delta V$ (fps)	$\Delta Fuel$ (lb)	Burn Time (s)	Burn Arc (deg)	
	Insertion Burn	Radial	16	+175.9	73.5	114	7.6
	Return Burn	Radial	94	-175.9	71.7	119	7.9
Time on Station	78 Orbits						
Fuel Budget	<u>Velocity Change Req't's</u>			$\Delta V$	$\Delta Fuel$		
	Insertion Burn			175.9 fps	73.5 lb		
	Return Burn			175.9 fps	71.7 lb		
	Trim Allowance				<u>14.5 lb</u>		
					159.7 lb		
	<u>ACS Req't's</u>						
	Oblateness Prec.				0.2 lb		
	Aerodynamic Torque				3.5 lb		
	Aerodynamic Drag				18.0 lb		
	Main Engine Misalignment				2.1 lb		
	Momentum Unloading				15.0 lb		
	ACQ/REACQ Maneuvers				2.0 lb		
	Attitude Control				<u>10.0 lb</u>		
					50.8 lb		
	<u>Retrieval Operations</u>						
	$\Delta V$ Adjust				20.0 lb		
	Attitude Adjust				<u>2.0 lb</u>		
					22.0 lb		
	Total Fuel Req'd				232.5 lb		
	Fuel Surplus (PAD)				517.5 lb		
	Total Fuel On-Board				750.0 lb		

Table 5.4-9 — Mission 2 Summary

Mission 2 Continuous Overflight Mission: 160 ± 50 nmi								
Payload WT	3062 lb							
Orbit Parameters	Size: 110 × 210 nmi		Semi-Major Axis: 3603.923 nmi					
	Period: 90.44525 min		ΔH 50 nmi					
	ECCEN: 0.013874		ΔS 200 nmi					
Major ΔV Burns	Type	Rev	ΔV (fps)	ΔFuel (lb)	Burn Time (s)	Burn Arc (deg)		
	<u>Insertion</u>							
	Burn 1	Radial	16	+175.9	73.5	114	7.6	
	Burn 2	Radial	17	+175.9	71.7	119	7.9	
	<u>Return</u>							
	Burn 1	Radial	93	-175.9	70.0	125	8.3	
	Burn 2	Radial	94	-175.9	68.4	132	8.8	
Time on Station	76 Orbits							
Fuel Budget	<u>Velocity Change Req't's</u>			ΔV	ΔFuel			
	Insertion Burns			351.7 fps	145.2 lb			
	Return Burns			351.8 fps	138.4 lb			
	Trim Allowance				28.4 lb			
					<hr/> 312.0 lb			
	<u>ACS Req't's</u>							
	Oblateness Prec.				0.2 lb			
	Aerodynamic Torque				11.0 lb			
	Aerodynamic Drag				42.0 lb			
	Main Engine Misalignment				8.4 lb			
	Momentum Unloading				25.0 lb			
	ACQ/REACQ Maneuvers				2.0 lb			
	Attitude Control				15.0 lb			
					<hr/> 103.6 lb			
	<u>Retrieval Operations</u>							
	ΔV Adjust				20.0 lb			
	Attitude Adjust				2.0 lb			
					<hr/> 22.0 lb			
		Total Fuel Req'd				437.6 lb		
		Fuel Surplus (Pad)				312.4 lb		
		Total Fuel On-Board				750.0 lb		

Both overflight missions provide approximately 4.8 days on station for ionospheric measurements. Mission 2 requires 205 lb additional fuel, three-fourths of which is due to the larger  $\Delta V$  transfer burns required and the remainder used to compensate for higher aerodynamic effects. Both overflight missions are accomplished with ample fuel reserves.

#### Tandem Orbit Mission

Requirements for the tandem orbit mission have been described in Section 5.4.1. In this section we shall determine the mission specifics of two particular tandem orbit missions. The first of these involves the spacecraft stopping at 5, 10, and 20 min lag positions with respect to the orbiter. The

second mission accumulates data with separations of 5, 15, and 45 min between spacecraft and Orbiter. In each case both satellite and Shuttle are in 90-min circular orbits during data acquisition periods. The required orbit altitude is 148.2 nmi.

*Mission 3: 5, 10, 20 Minute Lag Points* — To achieve a 5-min separation between LASSII and the Orbiter an in-plane maneuver  $\Delta V_1$  is executed to place the spacecraft in a 91-min transfer orbit as shown in Fig. 5.4-5. After five orbits have elapsed a second maneuver  $\Delta V_2$  equal but opposite to the first returns the spacecraft to the 90-min orbit but at the desired lag with respect to the Shuttle.

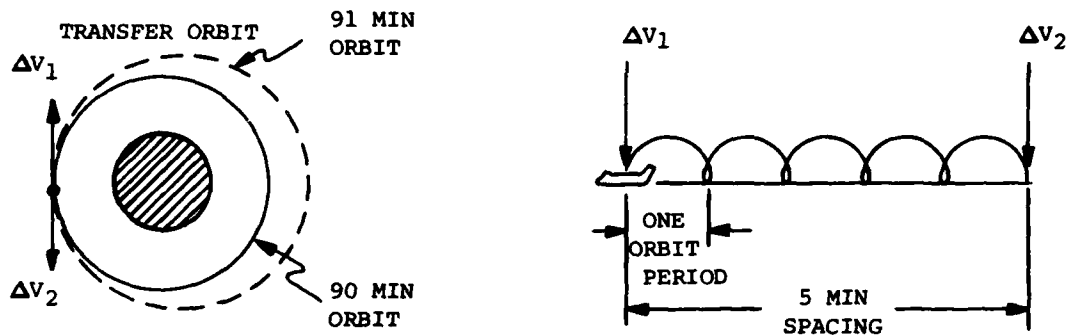


Fig. 5.4-5 — Tandem orbit transfer

Transfer to the 10-min lag position requires an additional 5-min separation and is achieved in five orbits by reinserting into the 91-min transfer orbit.

Transfer to the 20-min lag position, requiring an additional 10-min in separation, to be accomplished in five orbits requires insertion into a 92-min transfer orbit.

The final sets of maneuvers are associated with returning the spacecraft to the vicinity of the Shuttle. Ten orbits are permitted to achieve the return. The increase in permitted lap time is required to limit the total fuel requirements. Under this premise, the spacecraft must close the gap, between it and the Shuttle, at a rate of 2 min per revolution. This requires that the spacecraft be placed in an 88-min transfer orbit.

Twenty-five orbits are required for positioning of the spacecraft. This leaves 55 orbits for experiment observation, or 18-1/3 orbits at each observation point.

Table 5.4-10 presents a summary of the Mission 3 essentials.

*Mission 4: 5, 15, 45 Minute Lag Points* — The mission is similar to the previous one except for the increased separation, at the 2nd and 3rd data positions, between Shuttle Orbiter and the LASSII spacecraft.

The mission is designed with the objective of spending a minimum of 13 orbits at each of the three observation points. This leaves 2-1/2 days or 40 orbits for maneuvering between orbit stations.

Table 5.4-10 Mission 3 Summary

Mission 3 Tandem Orbit Mission: 5, 10, 20 minute Lag Points							
Payload WT	3062 lb						
Orbit Parameters	Satellite On Station Size: 148.16 nmi Circular      Semi-Major Axis: 3592.085 nmi Period: 90.0 min ECCEN: 0						
Major $\Delta$ Burns	In-Track Maneuver	REV	Transfer Orbit Period (min)	$\Delta V$ (fps)	$\Delta$ Fuel (lb)	Burn Time (s)	Burn Axis (deg)
Transfer to 5 min Lag Point							
	$\Delta V_1$	16	91	+92.7	39.0	60	4.0
	$\Delta V_2$	21		-92.7	38.5	61	4.1
Transfer to 10 min Lag Point							
	$\Delta V_3$	39	91	+92.7	38.0	62	4.2
	$\Delta V_4$	44		-92.7	37.5	64	4.3
Transfer to 20 min Lag Point							
	$\Delta V_5$	62	92	+184.0	73.0	132	8.8
	$\Delta V_6$	67		-184.0	71.2	139	9.3
Transfer Back to Shuttle							
	$\Delta V_7$	86	88	-192.4	72.5	155	10.3
	$\Delta V_8$	96		+192.4	70.6	165	11.0
Time On Station	18 Orbits at 5 min Lag Point 18 Orbits at 10 min Lag Point 19 Orbits at 20 min Lag Point						
Fuel Budget	Velocity Change Reqt's				$\Delta V$	$\Delta$ Fuel	
	Transfer to 5 min Lag PT				185.4 fps	77.5 lb	
	Transfer to 10 min Lag PT				185.4	75.5	
	Transfer to 20 min Lag PT				368.0	144.2	
	Return to Shuttle				384.8	143.1	
						<u>440.3 lb</u>	
	ACS Reqt's						
	Oblateness Prec					0.2	
	Aerodynamic Torque					7.2	
	Aerodynamic Drag					22.6	
	Main Engine Misalignment					7.5	
	Momentum Unloading					20.0	
	Acq/Reacq Maneuvers					2.0	
	Attitude Control					<u>10.0</u>	
						69.5 lb	
	Retrieval Operations						
	$\Delta V$ Adjust					20.0	
	Attitude Adjust					<u>2.0</u>	
						22.0 lb	
	Total Fuel Req'd					531.8 lb	
	Fuel Surplus (PAD)					218.2 lb	
	Total Fuel On Board					750.0 lb	

The following operations schedule was found to yield an acceptable fuel requirement.

Maneuver	No. of orbits permitted
Shuttle separation to 5 min lag point	5
5 min lag point to 15 min lag point	10
15 min lag point to 45 min lag point	10
Return to Shuttle	15

The last maneuver, which is the most expensive in terms of fuel usage, has been allowed the greater proportion of time available in order to reduce overall fuel requirements.

The first two maneuvers require injection into a 91 min transfer orbit and the latter two maneuvers use a 93 min transfer orbit.  $\Delta V$  and fuel requirements plus other pertinent mission parameters to accomplish Mission 4 are given in Table 5.4-11.

## 5.5 Radio Frequency (RF) System

An RF system is required to provide a means of transferring data to and from the orbiting LASSII spacecraft. To conserve prime spacecraft power, several operating modes are required. These modes will interface with the NASA Tracking and Data Relay Satellite Systems (TDRSS) and the NRL Tracking Facility at Blossom Point, Maryland.

### 5.5.1 Requirements

There are basically four modes required for returning data from LASSII:

(1) A low data rate mode operating through TDRSS multiple access. This mode is used as a low-power condition where only essential health status of the spacecraft and ranging information are required. This is the initial mode of operation when LASSII is first separated from the Shuttle, and is typically used during research orbits.

(2) A medium data rate mode through TDRSS multiple access. This mode is used when maneuvers are being executed. Ranging is also required in this mode.

(3) A high data rate through TDRSS to allow a normal playback of  $6 \times 10^9$  bits of recorded data per day. Since each TRDSS single access system can support only two spacecraft at a time, utilization of this system must be minimized. Real-time telemetry data are required during recorder playback, but there is no requirement for ranging.

(4) A survival mode is required which can be operated at the medium or low data rate. This is required in an event which requires nearly complete dc power shutdown. Spacecraft location is also required during this period.

During all of the above modes provision must be made for sending commands to the LASSII spacecraft.

## SZUSZCZEWICZ AND PALMA

Table 5.4-11 Mission 4 Summary

Mission 4 Tandem Orbit Mission: 5, 15, 45 minute Lag Points							
Payload WT	3062 lb						
Orbit Parameters	Satellite On Station Size: 148.16 nmi Circular      Semimajor Axis: 3592.085 nmi Period: 90.0 min ECCEN: 0						
Major $\Delta$ Burns	In-Track Maneuver	REV	Transfer Orbit Period (min)	$\Delta V$ (fps)	$\Delta$ Fuel (lb)	Burn Time (s)	Burn Arc (deg)
Transfer to 5 min Lag Point							
	$\Delta V_1$	16	91	+92.7	39.0	60	4.0
	$\Delta V_2$	21		-92.7	38.5	61	4.1
Transfer to 15 min Lag Point							
	$\Delta V_3$	34	91	+92.7	38.0	62	4.2
	$\Delta V_4$	44		-92.7	37.5	64	4.3
Transfer to 45 min Lag Point							
	$\Delta V_5$	57	93	+273.1	107.7	198	13.2
	$\Delta V_6$	67		-273.1	103.8	216	14.4
Transfer Back to Shuttle							
	$\Delta V_7$	81	93	+273.1	99.8	237	15.8
	$\Delta V_8$	96		-273.1	96.1	265	17.7
Time on Station	13 Orbits at 5 min Lag Point 13 Orbits at 15 min Lag Point 14 Orbits at 45 min Lag Point						
Fuel Budget	Velocity Change Reqt's				$\Delta V$	$\Delta$ Fuel	
	Transfer to 5 min Lag PT				185.4 fps	77.5 lb	
	Transfer to 15 min Lag PT				185.4	75.5	
	Transfer to 45 min Lag PT				546.2	211.5	
	Return to Shuttle				546.2	195.9	
						560.4 lb	
	ACS Reqt's						
	Oblateness Prec					0.2	
	Aerodynamic Torque					7.2	
	Aerodynamic Drag					22.6	
	Main Engine Misalignment					10.3	
	Momentum Unloading					20.0	
	Acq/Reacq Maneuvers					2.0	
	Attitude Control					10.0	
						72.3 lb	
	Retrieval Operations						
	$\Delta V$ Adjust					20.0	
	Attitude Adjust					2.0	
						22.0 lb	
	Total Fuel Req'd					654.7 lb	
	Fuel Surplus (PAD)					95.3 lb	
	Total Fuel On Board					750.0 lb	



### 5.5.2 System Implementation

To satisfy the requirements of the different operating modes each may be considered separately.

Implementation of the low data rate mode requires an omnidirectional antenna system. Figure 5.5-1 shows TDRSS multiple access return link performance of data rate versus antenna gain for transmitter power outputs of 2 and 4 W.

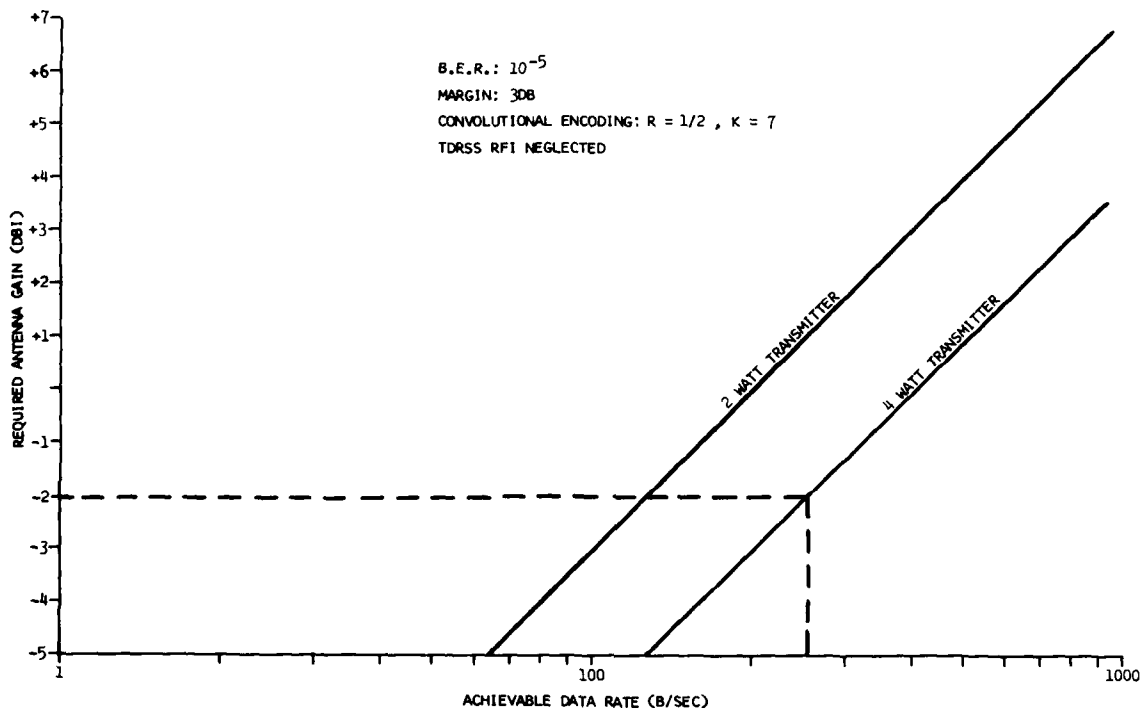


Fig. 5.5-1 — Multiple access return link performance

As seen from the graph a data rate of 256 bps can be achieved with an antenna gain of  $-2$  dBi and a 4 W transmitter. This size transmitter represents the maximum desired in terms of dc power consumption. The system will perform with the indicated BER of  $10^{-5}$  down to  $-5$  dBi antenna gain with no link margin.

Forward link performance through the omni antenna may be seen from Fig. 5.5-2. This also shows a nominal bit rate of 250 bps with  $-1.5$  dBi antenna gain and system operation to  $-4.5$  dBi with no margin.

An additional 10 dB of margin may be obtained during critical times such as initial separation from the Shuttle by requesting single access support for the multiple access frequency.

The low data rate hardware is described below.

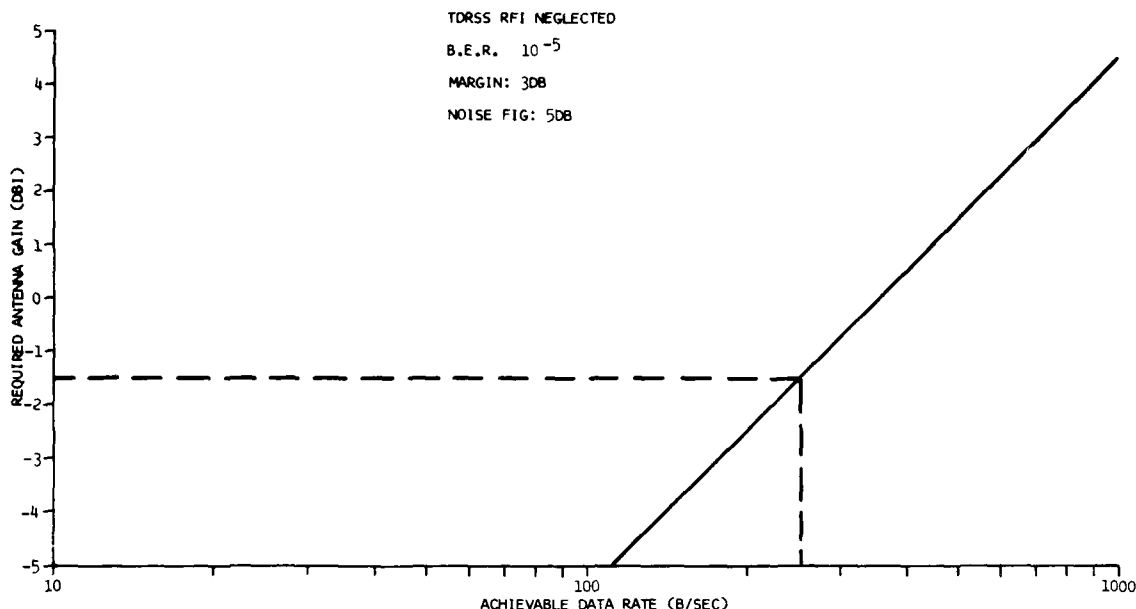


Fig. 5.5-2 — Multiple access forward link performance

#### (1) Multiple Access (MA) S-Band Transponder

This unit consists of a receiver, command detector, 5 W transmitter, and diplexer. The receiver is fixed-tuned to the MA forward link frequency of 2106.4 MHz. The transmitter is fixed-tuned to the MA return link frequency of 2287.5 MHz.

The transponder performs the following functions:

- (a) It receives and detects digital command signals which are modulo-2 added to the TDRSS pseudo-noise (PN) short spectrum-spreading code. The combination is phase-modulated on the suppressed-carrier, S-band, forward link transmitted by the relay satellite. The Self-Command Detector delivers the digital command data bit stream, the clock timing signal and an "in-lock" signal to MICROCATS.
- (b) It transmits telemetered data from MICROCATS as two independent digital data streams which are biphas-modulated in quadrature on the return link signal as a Staggered-Quadrature-Phase-Shift-Keyed (SQPSK) suppressed-carrier signal. These independent data streams are called the Q-Channel and I-Channel and are set for a power ratio of 4:1 so that the 5 W output is divided 4 W for Q-Channel (telemetry data) and 1 W for I-Channel (ranging data).
- (c) It turns around ranging signals by synchronizing the reference state in the return link PN spreading code with the reference state in the forward link code.
- (d) It phaselocks the transmitted return link carrier to the received forward link carrier in the precise ratio of 240/221 to provide doppler range rate data at the ground station. In the suppressed-carrier coherent mode, the receiver detector synthesizes the frequency to drive the transmitter. In the noncoherent mode, the return link carrier is not coherent with the forward link carrier but is derived from a stable crystal oscillator.

- (e) It responds to commands from MICROCATS to control configuration.
- (f) It provides self-monitoring status signals to MICROCATS for remote monitoring by way of the return link to Earth.

## (2) S-Band Omni Antenna Array

This antenna array consists of top-mounted and bottom-mounted antennas, power divider, and cables. The individual antenna pattern amplitude and phase will be adjusted to maximize the spherical coverage so that contact may be made with the spacecraft regardless of attitude. Since this antenna is entirely passive, it consumes no primary dc power.

Implementation of the high data rate mode through the S-Band Single Access (SSA) system requires considerable antenna gain and transmitter power. Sufficient antenna gain may be obtained from a parabolic dish mounted on LASSII; however, this approach presents problems associated with the mechanical steering of the antenna and effects on spacecraft stabilization. The LASSII approach utilizes a hemispherically shaped electronically steered array that can have its beam steered over the solid angle covered by the hemisphere.

Figure 5.5-3 shows the SSA link performance of the data rate versus antenna gain for transmitter power of 20 W. At the 20-inch radius (18 dBi gain) 1.6 Mbps can be transmitted with 3 dB margin.

The forward link is required to accept a data rate of 1 kbps. Figure 5.5-4 shows that data rates in excess of 100 kbps can be achieved with the 18 dBi gain ESSA antenna.

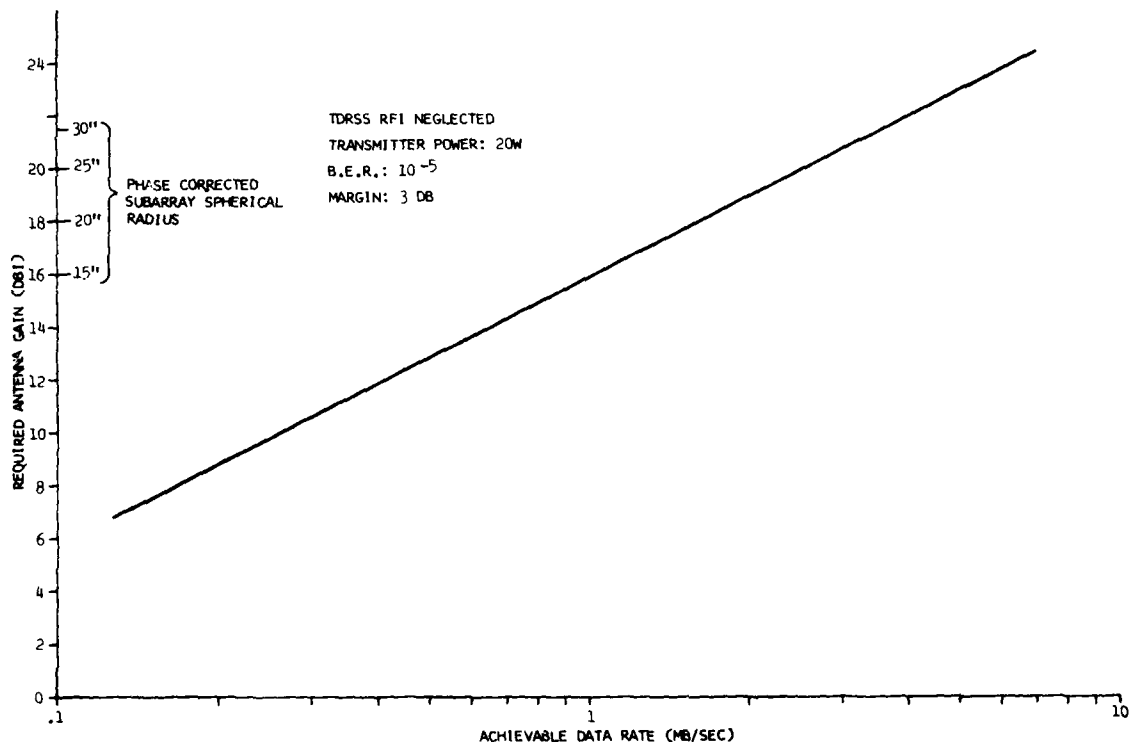


Fig. 5.5-3 — Single access return link performance

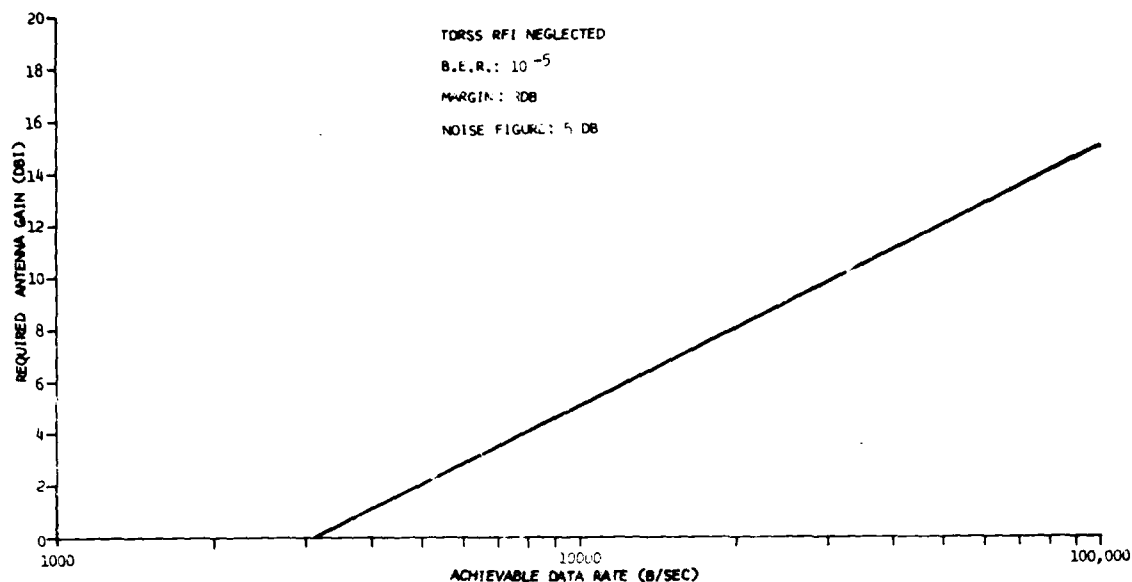


Fig. 5.5-4 — Single access forward link performance

The high data rate hardware consists of the following:

(1) *Single Access S-Band Transponder*. This unit is nearly identical to the MA transponder except that it is tuned to a pair of frequencies assigned to the single access system and operates at a power output of 2.5 W. The unit is BPSK modulated directly by convolution encoded and interleaved tape recorder and housekeeping data.

(2) *S-Band Power Amplifier*. This solid-state amplifier requires 2.5 W of drive power and is used to boost the SSA signal to the level required for recorder playback data.

(3) *S-Band Electronically Switched Spherical Array (ESSA)*. This antenna is designed specifically to operate with TDRSS. It is a fixed-mounted, electronically steered array which can generate a beam with a specified minimum gain in any direction within the required solid angle. It can be programmed to scan the entire hemisphere in less than 1 second, determine the direction of the forward link signal, and point the beam in that direction. Or it can point the beam on command.

It can also produce up to four independent beams with gain reduced by  $10 \log N$ , where  $N$  is the number of beams. An omnidirectional mode is also available; however, to conserve dc power (the ESSA is estimated to consume 15 W when operating), a separate omni system is incorporated for LAS-SII.

The ESSA consists of three major components:

- (a) A number of radiating elements over a roughly hemispherical shape, configured so that the beam coverage can be obtained over the required solid angle without mechanical motion.
- (b) A feed and switch manifold for selection of a discrete number of elements, which causes a beam to be formed in a predetermined direction.
- (c) A microprocessor which drives the switching network from digital input commands.

Implementation of the medium data rate is accomplished through the multiple access TDRSS by adding the 18 dBi gain of the ESSA to the MA Transponder. From Fig. 5.5-5 it can be seen that data rates up to 25 kbps can be transmitted with 3 dB margin. It has been determined that a bit rate of 8192 bps will suffice for this requirement and will have excess margin.

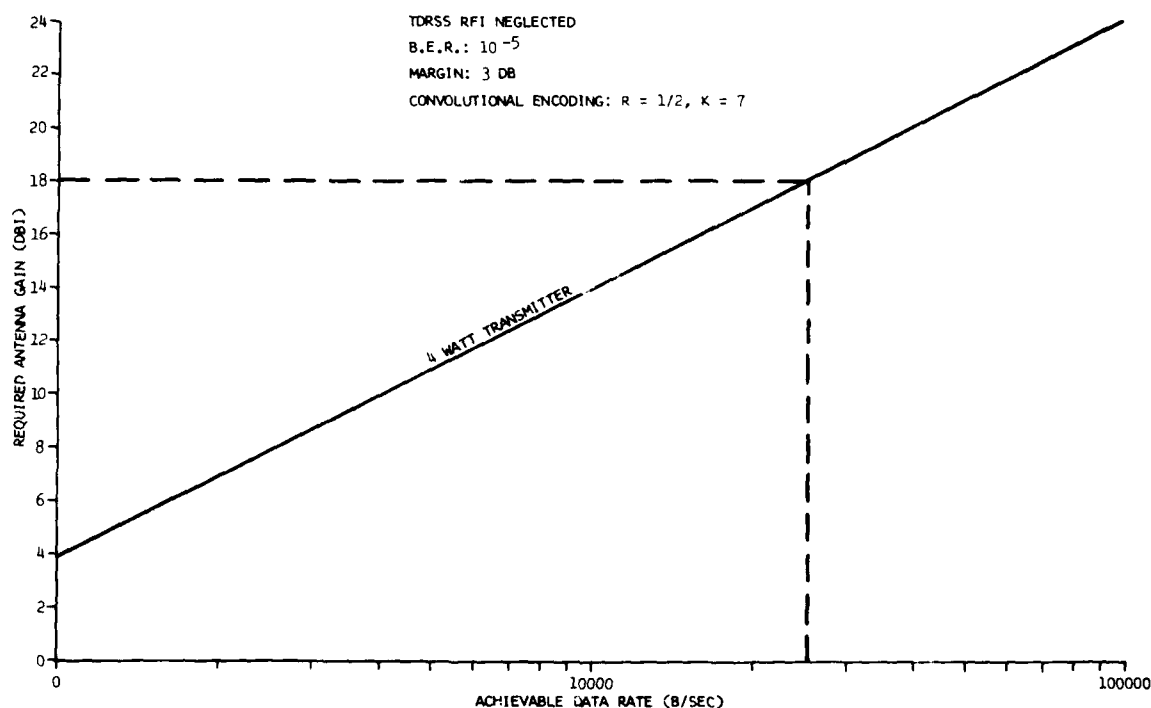


Fig. 5.5-5 — Multiple access return link

The survival mode is implemented by switching to a VHF system which has a very low dc power drain. This will allow housekeeping data to be received during the relatively short passes over Blossom Point. NRL has considerable experience with these systems and no problems are anticipated in receiving data at 8.192 kbps from LASSII or from the 1 kbps command system.

For passes with elevation angles greater than 81 deg the angular velocity exceeds the 9 deg/s available from the 48 ft tracking antenna at Blossom Point. This can be overcome by switching from autotrack to manual mode on the infrequent high passes and anticipating the azimuth changes. Since there is considerable link margin available this should present no problem.

Spacecraft location during this mode will be made by NAVSPASUR, assuming inclination is appropriate.

The survival mode hardware consists of the following:

(1) *VHF Transmitter.* This unit is similar to those used on previous NRL spacecraft. It is phase modulated by the NRZ-L digital data stream. Pre-mod filtering is employed to narrow the transmitted bandwidth.

(2) *VHF Receiver.* This unit is also similar to those used on previous NRL spacecraft. It accepts an amplitude modulated RF signal and outputs a detected audio waveform to the command system. This receiver employs a highly selective crystal filter preselector to greatly reduce front-end interference.

(3) *VHF Omni Antenna Array.* This antenna array consists of four quarter-wave monopoles on top of the spacecraft fed as crossed dipoles in phase quadrature. This type of array has been used on many previous NRL spacecraft.

The entire RF system is shown in Fig. 5.5-6. In addition to the major components described previously there are miscellaneous items such as hybrids, switches, and cables which are used to interconnect the various major components.

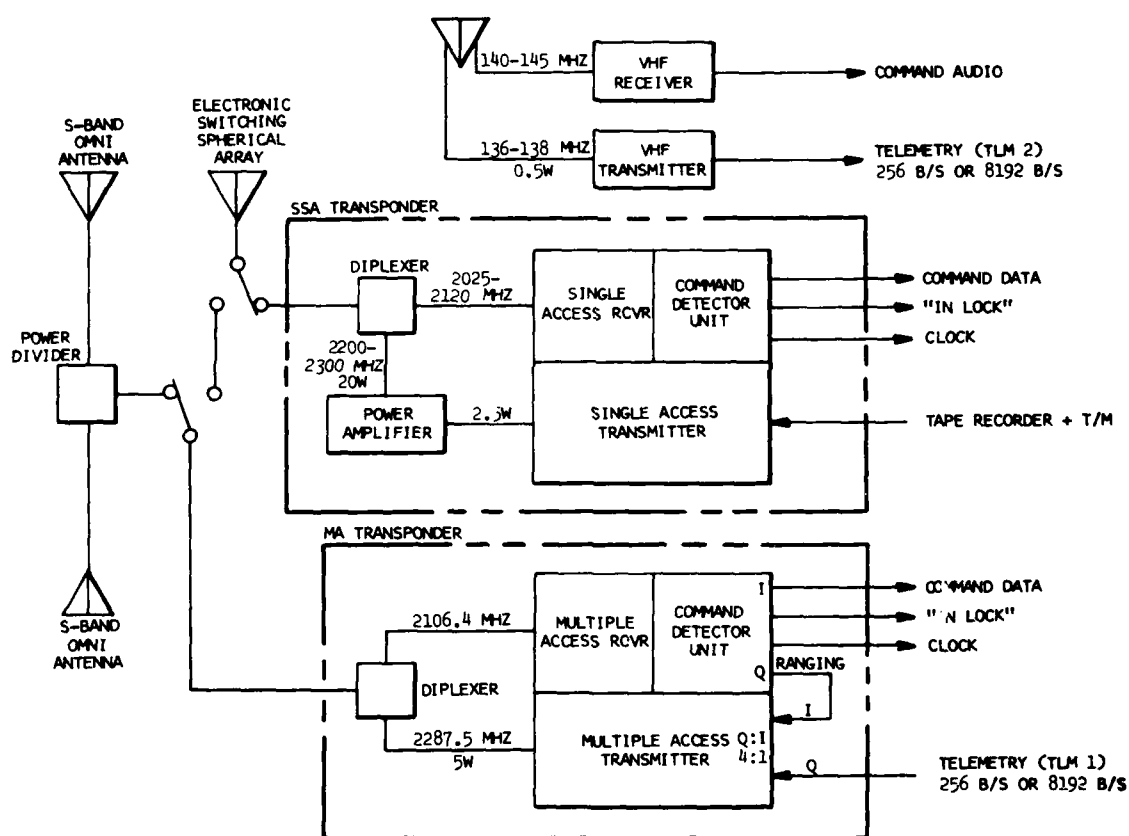


Fig. 5.5-6 — LASSII RF system diagram

### 5.5.3 Link Calculations

Detailed link calculations are shown in Tables 5.5.3-1 through 5.5.3-7.

Table 5.5.3-1 — TDRSS Multiple Access Forward Link  
Omni Antenna (-1 dBi) — 250 bps

Data		Carrier Acquisitions
$P_T$	43.0 dBm (TDRSS Handbook)	43.0
$G_{TDRSS}$	23.0 dBi (TDRSS Handbook)	23.0
$L_{RF}$	-1.0 dB (TDRSS Handbook)	-1.0
$L_{Transponder}$	-1.0 dB (TDRSS Handbook)	-1.0
$L_{PATH}$	-191.8 dB (Max Range)	-191.8
$L_{POL}$	-0.5 dB (TRDSS Handbook)	-0.5
$L_{UQPSK}$	-0.5 dB (TDRSS Handbook)	-0.5
$L_{DEMOD}$	-1.5 dB (TDRSS Handbook)	
$L_{PN}$	-1.0 dB (TDRSS Handbook)	
$G_R$	-1.0 dBi (Omni)	-1.0
Data Rate	-24.0 dB · Hz (250 bps)	Prec -129.8*
$E_b$	-156.3 dB/Hz	
$N_o$	-(-169.7) dB/Hz (5dB NF + 150°K TA)	
$E_b/N_o$	13.4 dB	
Req'd $E_b/N_o$	9.9 dB BER $10^{-5}$	
Margin	3.5 dB	

\*Receiver carrier acquisition thresholds in diplexer -135.5 dBm

Table 5.5.3-2 — TDRSS Multiple Access Return Link Low  
Power (5.0 W)-Omni (-1 dBi)-256 bps

$P_T$	36.0 dBm (4.0 W 0-Channel)
$G_T$	-1.0 dBi (Omni)
$L_{PATH}$	-192.5 dB (Max. Range)
$L_{POL}$	-1.0 dB (TDRSS Handbook)
$G_{TDRSS}$	28.0 dB (TDRSS Handbook)
$L_{TRANSPONDER}$	-2.0 dB (TDRSS Handbook)
$L_{DEMOD}$	-1.5 dB (TDRSS Handbook)
$L_{PN}$	-1.0 dB (TDRSS Handbook)
$L_{BEAMFORMING}$	-0.5 dB (TDRSS Handbook)
Data Rate	-24.0 dB · Hz (256 bps)
$E_b$	-159.5 dB/Hz
$N_o$	-(-168.3) dB/Hz (TDRSS Handbook)
$E_b/N_o$	8.8 dB
Req'd $E_b/N_o$	-4.7 dB R = 1/2, k = 7 Coding; $10^{-5}$ BER
Margin	4.1 dB

Table 5.5.3-3 — TDRSS Multiple Access Forward Link  
ESSA Antenna (18 dBi) — 1 kbps

Data		Carrier Acquisitions	
$P_T$	43.0 dBm	(TDRSS Handbook)	43.0
$G_{TDRSS}$	23.0 dBi	(TDRSS Handbook)	23.0
$L_{RF}$	-1.0 dB	(TDRSS Handbook)	-1.0
$L_{Transponder}$	-1.0 dB	(TDRSS Handbook)	-1.0
$L_{PATH}$	-191.8 dB	(Max Range)	-191.8
$L_{POL}$	-0.5 dB	(TDRSS Handbook)	-0.5
$L_{SQPSK}$	-0.5 dB	(TDRSS Handbook)	-0.5
$L_{DEMOD}$	-1.5 dB	(TDRSS Handbook)	
$L_{PN}$	-1.0 dB	(TDRSS Handbook)	
$G_R$	18.0 dB	(ESSA)	18.0
Data Rate	-30.0 dB · Hz	(10 kbps) — Max. Avail. on MA	*Prec. -110.8
$E_b$	-143.3 dB/Hz		
$N_o$	-(-169.7) dB/Hz	(5 dBNF + $T_A$ (150°K))	
$E_b/N_o$	26.4 dB		
Req'd $E_b/N_o$	9.9 dB	BER $10^{-5}$	
Margin	16.5 dB		

\*Receiver carrier acquisition thresholds in to diplexer -135.5 dBm

Table 5.5.3-4 — TDRSS Multiple Access Return Link Low  
Power (5.0 W)-ESSA (18 dBi)-8.192 kbps

$P_T$	36.0 dBm	(4.0W Q Channel)
$G_T$	18.0 dBi	(20'' Radius Array)
$L_{PATH}$	-192.5 dB	(Max. Range)
$L_{POL}$	-1.0 dB	(TDRSS Handbook)
$G_{TDRSS}$	28.0 dBi	(TDRSS Handbook)
$L_{TRANSPONDER}$	-2.0 dB	(TDRSS Handbook)
$L_{DEMOD}$	-1.5 dB	(TDRSS Handbook)
$L_{PN}$	-1.0 dB	(TDRSS Handbook)
$L_{BEAMFORMING}$	-0.5 dB	(TDRSS Handbook)
Data Rate	-39.1 dB · Hz	(8.192 kbps)
$E_b$	-155.6 dB/Hz	
$N_o$	-(-168.3) dB/Hz	(TDRSS Handbook)
$E_b/N_o$	12.7 dB	
Req'd $E_b/N_o$	4.7 dB	$R = 1/2$ , $K = 7$ Coding; $10^{-5}$ BER
Margin	8.0 dB	



Table 5.5.3-5 — TDRSS Single Access Forward Link  
(ESSA + 18 dBi) 1 kbps

Data			Carrier Acquisitions
$P_T$	41.6 dBm	(TDRSS Handbook)	41.6
$L_{RF}$	-2.0 dB	(TDRSS Handbook)	-2.0
$G_{TDRSS}$	35.4 dBi	(TDRSS Handbook)	35.4
$L_{TRANSPONDER}$	-1.0 dB	(TDRSS Handbook)	-1.0
$L_{POINTING}$	-0.5 dB	(TDRSS Handbook)	-0.5
$L_{PATH}$	-191.8 dB	(Max Range)	-191.8
$L_{POL}$	-0.5 dB	(TDRSS Handbook)	-0.5
$L_{SQPSK}$	-0.5 dB	(TDRSS Handbook)	-0.5
$L_{DEMOD}$	-1.5 dB	(TDRSS Handbook)	
$L_{PN}$	-1.0 dB	(TDRSS Handbook)	
$G_R$	18.0 dB	ESSA	18.0
Data Rate	-30.0 dB · Hz		*Prec. -101.3
$E_b$	-133.8 dB/Hz		
$N_o$	-(-169.7) dB/Hz	(5dB NF + 150°K TA)	
$E_b/N_o$	35.9 dB		
Req'd $E_b/N_o$	9.9 dB	BER $10^{-5}$	
Margin	26.0 dB		

\*Receiver carrier acquisition thresholds into diplexer -135.5 dBm

Table 5.5.3-6 — TDRSS Single Access (S-Band) Return Link  
High Power (20 W) — ESSA (18 dBi) — 1.3 Mbps

$P_T$	43.0 dBm	(20 W)
$G_T$	18.0 dBi	(20' Radius Array)
$L_{PATH}$	-192.5 dB	(Max Range)
$L_{POINTING}$	-0.5 dB	(TDRSS Handbook)
$L_{POL}$	-0.5 dB	(TDRSS Handbook)
$G_{TDRSS}$	36.0 dB	(TDRSS Handbook)
$L_{TRANSPONDER}$	-2.0 dB	(TDRSS Handbook)
$L_{DEMOD}$	-1.5 dB	(TDRSS Handbook)
Data Rate	-61.2 dB · Hz	(1.33 Mbps)
$E_b$	-161.2 dB/Hz	
$N_o$	-(-170.9) dB/Hz	
$E_b/N_o$	9.7 dB	
Req'd $E_b/N_o$	-4.1 dB	R = 1/3, K = 7 Coding; $10^{-5}$ BER
Margin	5.0 dB	

NOTE: Actual bit rate is 3.99 Mbps.

Information rate is 1.33 Mbps and includes tape recorder  
playback data plus housekeeping.

Table 5.5.3-7 — VHF Links to Blossom Point

Down		Up	
$P_T$	27.0 dBm (.5W)	$P_T$	54.5 dBm
$G_T$	-10.0 dB	$G_T$	23.0 dBi (48')
$L_{PATH}$	-141.0 dB (0°, 160 nmi)	$L_{PATH}$	-139.0 dB (5°, 160 nmi)
$G_R$	23.0 dBi (48')	$G_R$	-8.0 dBi (95°)
$L_{FIL}$	-3.4 dB		
$G_{PA1}$	+16.0 dB	Prec.	-69.5 dBm
$L_{FIL}$	-0.5 dB	Rcvr Sens.	-(-97.0) dBm
$G_{PA2}$	+16.0 dB	Margin	27.5 dB
$L_{CABLE}$	-8.0 dB		
Prec.	-80.9 dB		
Date Rate	-39.1 dB · Hz		
$E_b$	-120.0 dB/Hz		
$N_b$	-(-145.7) dB/Hz		
$E_b/N_b$	25.7 dB		
Req'd	-10.6 dB BER $10^{-6}$		
Margin	15.1 dB		

#### 5.5.4 Power Density Considerations

Due to international agreements the power density of the S-Band RF signal impinging on Earth must be kept below the following specified levels:

- A. Elevation of user  $\leq 5$  deg,  $-151$  dBW/4 kHz/m<sup>2</sup>
- B. Elevation of User  $> 5$  deg;  $\leq 25$  deg,  
 $[-151 + (\theta - 5)/2]$  dBW/4 kHz/m<sup>2</sup>  
 where  $\theta$  = elevation angle
- C. Elevation of user  $> 25$  deg;  
 $-141$  dBW/4 kHz/m<sup>2</sup>

The power spectrum of a signal phase-modulated by a random NRZ-L waveform is shown in Fig. 5.5-7. Considering the illumination of Earth as depicted in Fig. 5.5-8, and the antenna pattern of Fig. 5.5-9, calculations have been made for values of power density at various elevation angles and orbit altitudes of 140, 250 and 600 nmi. Table 5.5-1 documents this. Positive margins exist for all angles except near 5 deg elevation at the lowest altitude. This indicates that transmission would have to be terminated approximately 1 deg sooner on the antenna pattern. By terminating transmission when Earth's horizon intercepts an angle of approximately 12 deg off antenna boresight, the transmission time is reduced from what would be available for horizon-to-horizon coverage.

A worst case analysis was done to determine the minimum number of degrees per orbit during which the LASSII satellite would have communication with TDRSS. Communication was assumed possible if the line from LASSII to TDRSS was above the Earth horizon by delta degrees, with the program being run for delta of 12 and 32 deg. Calculations were made for orbital height above Earth's surface of 140, 250, and 600 nmi. The orbit was inclined with the equatorial plane at an angle of 28.5, 57, and 90 deg for each orbital altitude. A circular orbit was assumed.

The calculation was done for two TDRSS satellites 130 deg from each other. For these satellites a 24-hour Earth synchronous orbit with 0-deg inclination was assumed.

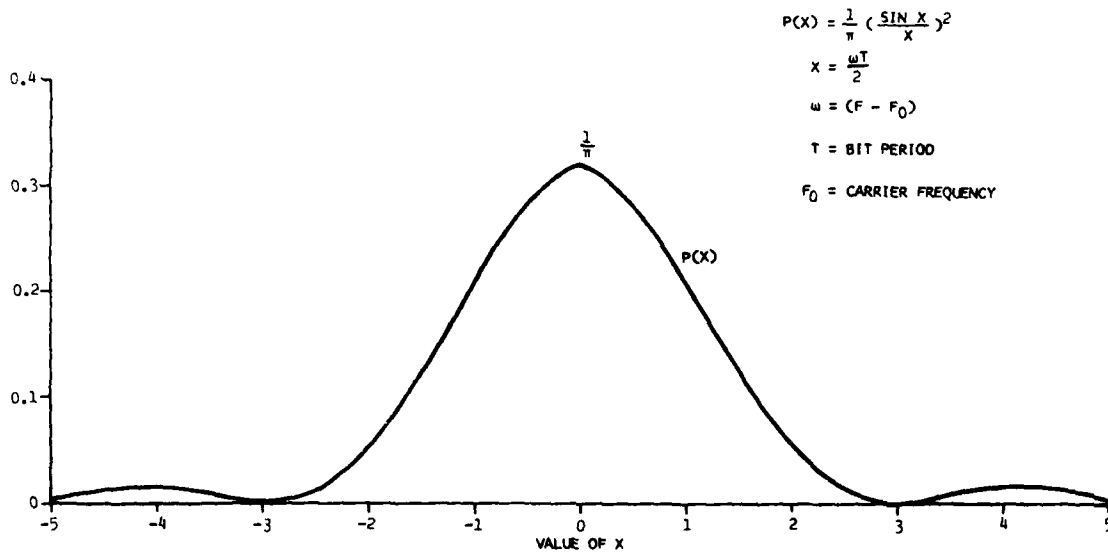


Fig. 5.5-7 — Power spectrum of NRZ-L

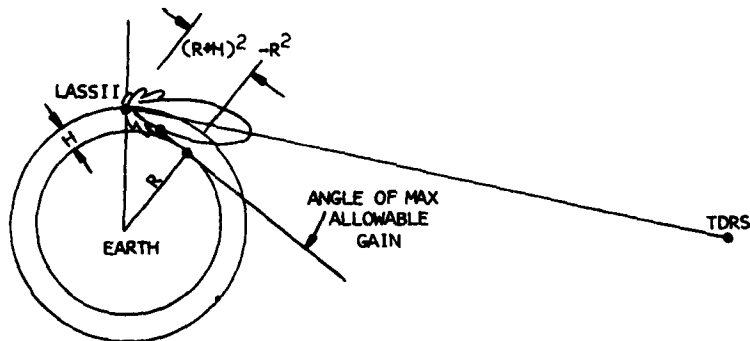


Fig. 5.5-8 — LASSII illumination of Earth's surface

82

Table 5.5-1 — Maximum Power Density in 4 kHz Bandwidth on Earth's Surface (BPSK NRZ-L 20-W Transmitter/ESSA)

Elevation Angle (deg)	Angle Off Boresight (deg)	Trans. Power Spectral Density (dBW/4 kHz)	Antenna Gain Envelope (dBi)	Path Spreading Loss (dBm <sup>2</sup> )	Power Density (dBW/4 kHz/m <sup>2</sup> )	Max. Power Density Allowed (dBW/4 kHz/m <sup>2</sup> )	Margin (dB)
<b>140 nmi</b>							
0	12.0	-17.0	+23	-136.3	-151.0	-151.0	0
5	12.8	↑	+5	-133.7	-150.2	-151.0	-0.8
10	14.9		-2.0	-131.3	-150.3	-148.5	1.8
25	25.4		-5.0	-126.1	-148.1	-141.0	7.1
40	38.6		-9.0	-122.9	-148.9	↑	7.9
60	57.3		-13.5	-120.5	-151.0		10.0
80	76.4	↓	-17.0	-119.4	-153.4	↓	12.4
90	86.0		-18.0	-119.3	-154.3		13.3
<b>250 nmi</b>							
0	11	-17.0	+3.0	-138.9	-152.9	-151.0	1.9
5	11.6	↑	+2.5	-136.9	-151.4	-151.0	0.4
10	13.2		-1.5	-135.1	-153.6	-148.5	5.1
25	22.1		-4.0	-130.7	-151.7	-141.0	10.7
40	34.2		-9.0	-127.8	-153.8	↑	12.8
60	52.0		-14.0	-125.5	-156.5		15.5
80	70.5	↓	16.5	-124.4	-157.9	↓	16.9
90	79.8		-16.5	-124.3	-157.8		16.8
<b>600 nmi</b>							
0	10.5	-17.0	+7.0	-142.9	-152.9	-151.0	1.9
5	10.9	↑	+6.0	-141.6	-152.6	-151.0	1.6
10	11.9		+2.5	-140.4	-154.9	-148.5	6.4
25	18.4		-2.5	-137.3	-156.8	-141.0	15.8
40	28.2		-6.5	-134.9	-158.4	↑	17.4
60	43.7		-12.5	-132.9	-162.4		21.4
80	60.4	↓	-16.5	-132.0	-165.5	↓	24.5
90	68.9		-17.5	-131.9	-166.4		25.4

LASSII was stepped around the orbit with time increments equivalent to steps of 1 deg. Each TDRSS satellite was advanced a proportional amount in inertial space. The vector to TDRSS from LASSII was determined and compared to the vector to Earth center. If *either* angle (between the two vectors) was greater than delta degrees above the horizon, a counter was incremented (i.e., LASSII could see *at least one of the relay satellites*). In this matter the number of degrees per orbit where communication was possible was counted. An orbit class was specified by height and inclination. After an orbit had been "counted" the count was stored and the longitude of equator crossing was shifted 3 deg with respect to TDRSS. After the equator crossing longitude has been stepped a total of 180 deg the "worst case" for that class was printed out. Table 5.5-2 shows the minimum coverage time per orbit for the various orbit parameters discussed above.

The total time required for playback at 1.33 Mbps (1.7 Gb storage capacity) is 0.36 hour (21.3 min) for delta of 12 deg. Due to TDRSS scheduling it may be necessary to spread this period over more than one orbit. It is concluded then that at least 0.31 hour (18.6 min) worst case excess coverage time is available per orbit for tape recorder dump and still meet the power density requirements.

Table 5.5-2 — Min. Number of Degree/Orbit and Minutes/Orbit Where Communication Is Possible

Flight (mi)	Inclination (deg)	Angle Above Line to Horizon $\Delta = 12$		Angle Above Line to Horizon $\Delta = 32$	
		deg/orbit	min/orbit	deg/orbit	min/orbit
140	28.5°	293	73	248	62
	57°	282	70	210	52
	90°	160	40	41	10
250	28.5°	303	79	262	68
	57	292	76	230	60
	90	179	47	85	22
600	28.5°	325	97	280	83
	57	313	93	271	81
	90	263	78	136	40

Since the omni antenna is radiating toward Earth at all times when the low data rate mode is used, it is necessary to examine the power density on Earth's surface from this antenna. Information transmitted in the low data rate mode (telemetry and ranging) is modulo - 2 added asynchronously to approximately 3 Mbps chip rate spread spectrum signal. From the previous analysis it was determined that the maximum power density in a 4 kHz bandwidth was 28.8 dB below the total transmitted power. Table 5.5-3 shows the power density at Earth's surface. From the values shown it is concluded that the power density numbers are not exceeded.

During medium data rate transmission power of 5 W is fed into the ESSA antenna. Since both the I- and Q-channels are spread spectrum at approximately 3 Mbps chip rate, the maximum power in the 4 kHz bandwidth is 28.8 dB down from the 5 W output or -21.8 dBW/4 kHz. As a result the maximum allowable gain toward Earth's horizon is 6.5 dB higher than with the high-power transmitter. Figure 5.5-9 shows that this occurs at 11 deg off boresight.

Values for power density (Table 5.5-4) show that a positive margin exists if transmission is terminated when the boresight of the antenna is 11 deg above the horizon. Coverage times would be nearly identical to those given in Table 5.5-2 for the high data rate mode.

#### 5.5.5 TDRSS RFI Considerations

During operation of TDRSS it is expected that ground-based radars will interfere with the return link signal transmitted through TDRSS. Studies show that degradations on the order of 0.7 dB for the MA channel and 2.8 dB for the SSA channels may be experienced. These values have not been included in the link analyses shown in Section 5.3.3 but must be included as more information becomes available from NASA.

#### 5.6 Thermal Protection System

The preliminary thermal design developed for LASSII will satisfy the thermal requirements for both the free flyer portion of the mission as well as the period of time in which the spacecraft is in the cargo bay of the Shuttle.

Table 5.5-3 — Maximum Power Density in 4 kHz Bandwidth on Earth's Surface  
(SQPSK NRZ-L 5-W Transmitter)

Elevation Angle (deg)	Angle from +Z Axis (deg)	Trans. Power Spectral Density (dBW/4 kHz)	Antenna Gain (dBi)	Path Spreading Loss (dBm <sup>2</sup> )	Power Density (dBW/4 kHz/m <sup>2</sup> )	Max. Power Density Allowed (dBW/4 kHz/m <sup>2</sup> )	Margin (dB)
140 nmi							
0	106.0	-21.8	-3	-136.3	-161.1	-151.0	10.1
5	106.8	↑	-3	-133.7	-158.5	-151.0	7.5
10	108.9	↑	-2	-131.3	-155.1	-148.5	6.6
25	119.4	↑	-1	-126.1	-148.9	-141.0	7.9
40	132.6	↑	0	-122.9	-144.7	↑	3.7
60	151.3	↑	0	-120.5	-142.3	↑	1.3
80	170.4	↓	0	-119.4	-141.2	↓	0.2
90	180.0	-21.8	0	-119.3	-141.1	-141.0	0.1
250 nmi							
0	111.2	-21.8	-2	-138.9	-162.7	-151.0	11.7
5	111.8	↑	-2	-136.9	-160.7	-151.0	9.7
10	113.4	↑	-2	-135.1	-158.9	-148.5	10.4
25	122.3	↑	-1	-130.7	-153.5	-141.0	12.5
40	134.4	↑	0	-127.8	-149.6	↑	8.6
60	152.2	↑	0	-125.5	-147.3	↑	6.3
80	170.7	↓	0	-124.4	-146.2	↓	5.2
90	180.0	-21.8	0	-124.3	-146.1	-141.0	5.1
600 nmi							
0	121.6	-21.8	-1	-142.9	-165.7	-151.0	14.7
5	122.0	↑	-1	-141.6	-164.4	-151.0	13.4
10	123.0	↑	-1	-140.4	-163.2	-148.5	14.7
25	129.5	↑	0	-137.3	-159.1	-141.0	18.1
40	139.3	↑	0	-134.9	-156.7	↑	15.7
60	154.8	↑	0	-132.9	-154.7	↑	13.7
80	171.5	↓	0	-132.0	-153.8	↓	12.8
90	180.0	-21.8	0	-131.9	-153.7	-141.0	12.7

Table 5.5-4 — Maximum Power Density in 4 kHz Bandwidth on Earth's Surface  
(SQPSK NRZ-L 5-W Transmitter/ESSA)

Elevation Angle (deg)	Angle Off Boresight (deg)	Trans. Power Spectral Density (dBW/4 kHz)	Antenna Gain (dBi)	Path Spreading Loss (dBm <sup>2</sup> )	Power Density (dBW/4 kHz/m <sup>2</sup> )	Max. Power Density Allowed (dBW/4 kHz/m <sup>2</sup> )	Margin (dB)
140 nmi							
0	11.0	↑ -21.8	6.5	-136.3	-151.6	-151.0	0.6
5	11.8		2.0	-133.7	-153.5	-151.0	2.5
10	13.9		-4.0	-131.3	-157.1	-148.5	8.6
25	24.4		-5.0	-126.1	-152.9	-141.0	11.9
40	37.6		-9.0	-122.9	-153.7		12.7
60	56.3		-13.5	-120.5	-155.8		14.8
80	75.4		-17.0	-119.4	-158.2		17.2
90	85.0	↓ -21.8	-18.0	-119.3	-159.1	-141.0	18.1
250 nmi							
0	11.0	↑ -21.8	6.5	-138.9	-154.2	-151.0	3.2
5	11.6		2.5	-136.9	-156.2	-151.0	5.2
10	13.2		-1.5	-135.1	-158.4	-148.5	9.9
25	22.1		-4.0	-130.7	-156.5	-141.0	15.5
40	34.2		-9.0	-127.8	-158.6		17.6
60	52.0		-14.0	-125.5	-161.3		20.3
80	70.5		-16.5	-124.4	-162.7		21.7
90	79.8	↓ -21.8	-16.5	-124.3	-162.6	-141.0	21.6
600 nmi							
0	11.0	↑ -21.8	6.5	-142.9	-158.2	-151.0	7.2
5	11.4		4.0	-141.6	-159.4	-151.0	8.4
10	12.4		0	-140.4	-162.2	-148.5	13.7
25	18.9		-2.5	-137.3	-161.6	-141.0	20.6
40	28.7		-6.5	-134.9	-163.2		22.2
60	44.2		-12.5	-132.9	-167.2		26.2
80	60.9		-16.5	-132.0	-170.3		29.3
90	69.4	↓ -21.8	-17.5	-131.9	-171.2	-140.0	30.2

### 5.6.1 Summary

The thermal subsystems on LASSII will utilize a 40 by 92 in. radiator located on the anti-RAM side of the spacecraft as the primary heat rejection surface (see Fig. 5.6-1). The location chosen for the radiator has the required heat rejection area and does not interfere with the design of the scientifically important RAM surface of the spacecraft. The power being dissipated internal to the main body of the spacecraft, as well as any heat flow(s) into the spacecraft through the gold coated multilayer insulation blankets, will be transferred to this radiator via a heat pipe/liquid loop system that will maintain internal spacecraft temperatures at  $20^\circ \pm 10^\circ\text{C}$ .

The two solar cell array assemblies will be thermally isolated from the main body of the spacecraft and will utilize the octagonal surfaces at the ends of the arrays as heat rejection radiators (see Fig. 5.6-1). These radiators will reject the power being dissipated by the instruments inside the arrays as well as any absorbed fluxes. Heater power will be required to maintain the instruments inside the arrays above their minimum temperature limit in a cold orientation.

An electrically conducting white paint (NASA GSFC NS43C) will be utilized as the low  $\alpha/\epsilon$  coating on all radiators and on selected areas of the exposed gold surface of the MLI blankets.



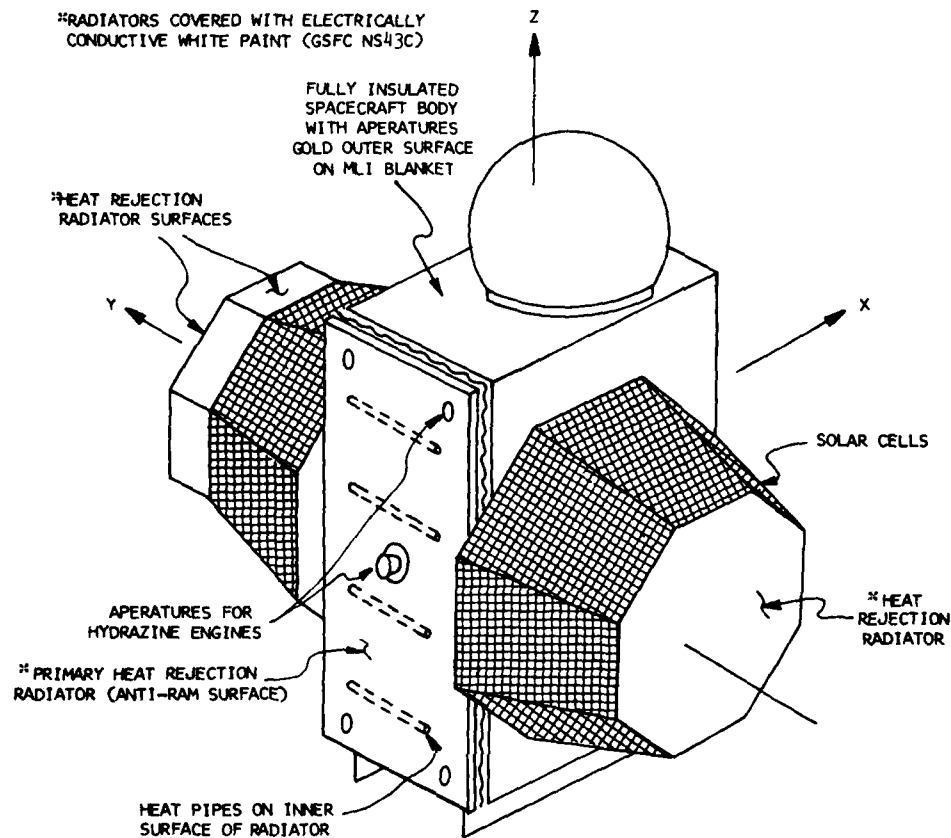


Fig. 5.6-1 — LASSII thermal control radiators

The primary heat rejection radiator will be mounted on low-conductance standoffs, and an MLI blanket will be between the radiator and the spacecraft to thermally isolate it from the adjacent spacecraft structure and the hydrazine system (located inside the payload on the  $-X$  face). The interior of the spacecraft will be thermally coupled to the radiator via a Freon II liquid loop utilizing a variable speed positive displacement pump to control flow rate and internal spacecraft temperature.

This active liquid loop system, developed for Shuttle payloads, will transfer the heat from the warm interior of the spacecraft to the potentially cold radiator without exposing the hydrazine system to the inner surface of the potentially cold radiator.

The liquid loop system is being proposed because the two hydrazine storage tanks and the 150 lbf hydrazine engine with the thermal protection system will block a significant fraction of the view from the inner section of the spacecraft to the inner surface of the radiator. The liquid loop system will transfer the spacecraft heat around the hydrazine system to the cold radiator while maintaining the hydrazine components at interior spacecraft temperature.

The liquid loop system will be used in conjunction with ammonia heat pipes. The heat pipes will mount in holders bonded to the individual equipment decks and to the radiator, and will isothermize these parts of the spacecraft. The (redundant) liquid loop system will be integral with the basic spacecraft support structure on the  $\pm Y$  sides of the spacecraft and will exchange heat with the heat pipes at

AD-A119 078

NAVAL RESEARCH LAB WASHINGTON DC

F/B 20/0

THE LASSII PROGRAM: OBJECTIVES, SPACECRAFT DESIGN, AND MISSION --ETC(U)

JUN 82 E P SZUSZCZEWICZ, R E PALMA

UNCLASSIFIED

NRL-8420

NL

2 2

1 1

1 1

1 1

1 1

1 1

1 1

1 1

1 1

1 1

1 1

1 1

1 1

1 1

1 1

1 1

1 1

1 1

1 1

1 1

1 1

1 1

1 1

1 1

1 1

1 1

1 1

1 1

1 1

1 1

1 1

1 1

1 1

1 1

1 1

1 1

1 1

1 1

1 1

1 1

1 1

1 1

1 1

END  
DATE  
10 82  
DTIC

the  $\pm Y$  edges of the various panels. The heat pipes will all be installed in a horizontal orientation in the spacecraft to permit thermal testing of the payload in a 1 g field, and they will transfer heat between the  $\pm Y$  edge of each panel and the remaining area of the panel. The heat will then be conducted across a bolted interface (filled with RTV or thermal grease) to get into and out of the liquid loop system.

Because the primary heat rejection radiator is thermally isolated from the basic spacecraft support structure, the liquid loop system will have two flexible couplings at the radiator to permit the tubing to mount directly to a vertical edge of the radiator.

The requirement for 10 m<sup>2</sup> of an exposed gold surface on the exterior of the spacecraft has a significant impact on the thermal subsystem. Gold has a large ratio of solar absorptance ( $\alpha = 0.29$ ) to IR emittance ( $\epsilon = 0.02$ ) and can reach high temperatures when exposed to sunlight in space ( $\alpha/\epsilon = 14.5$ ). Assuming an interior spacecraft of 20°C and a maximum solar constant of 1399 W/m<sup>2</sup>, a gold surface could reach 377°C with an effective blanket emittance of 0.02 and 426°C with an effective blanket emittance of 0.01. These high temperatures preclude the use of a kapton substrate which has a maximum (continuous) temperature limit of 288°C. Therefore, gold-coated metallic substrates are being considered for the exposed layer.

Associated with these high surface temperatures is a heat flow into the spacecraft through the MLI blankets. There is also a potential diffusion problem between the gold and its metallic substrate. This diffusion process, sometimes referred to as the "purple plague," is an effect encountered in the electronics industry when gold and aluminum react to form a visible purple material. The formation of the purple material is strongly affected by temperatures as shown in Fig. 5.6-2. For gold coating directly on an aluminum substrate, maximum surface temperature would have to be held to approximately 100° to 150°C.

A technique to reduce the temperature of the sunlit gold surfaces is to use small areas of a low  $\alpha/\epsilon$  material on the sunlit surface in conjunction with a thermally conducting substrate. A candidate coating is an electrically conducting white paint developed by NASA Goddard Space Flight Center and designated an NS43C. Table 5.6-1 summarizes the predicted maximum surface temperature for the gold plus white paint combination as a function of the fraction of the exposed surface covered with the low  $\alpha/\epsilon$  white paint and the effectiveness of the MLI blanket. Greater than 20% of the exposed gold surface would have to be covered with the low  $\alpha/\epsilon$  white paint in order to keep maximum surface temperatures below 150°C. This implies an additional 2 m<sup>2</sup> of exposed surface if 10 m<sup>2</sup> are to remain gold coated. Also shown in Table 5.6-1 are the resulting heat flows through the MLI thermal protection system on the RAM surface of the spacecraft when it is exposed to direct sunlight.

The use of a gold surface which is partially covered with a low  $\alpha/\epsilon$  white paint necessitates the use of a thermally conducting substrate to isothermize the overall surface. Aluminum is a good thermal conductor. However because of the reaction with gold, other substrate materials will be considered. It might also be possible to put a layer of a material such as a palladium or titanium on the aluminum substrate before applying the gold coating so as to separate the two reacting materials. (The substrate material would probably be a foil with a thickness between 0.002 to 0.005 in.). A testing program will be required to prepare and test small samples of any proposed gold/substrate combination at elevated temperatures before designing and fabricating the flight hardware gold surface.

### 5.6.2 Technical Discussion

#### Hot and Cold Orbital Conditions

A simple geometric computer model of LASSII, developed by the structural group at NRL, was utilized in conjunction with the Simplified Shuttle Payload Thermal Analyzer Computer Program

# NRL REPORT 8420

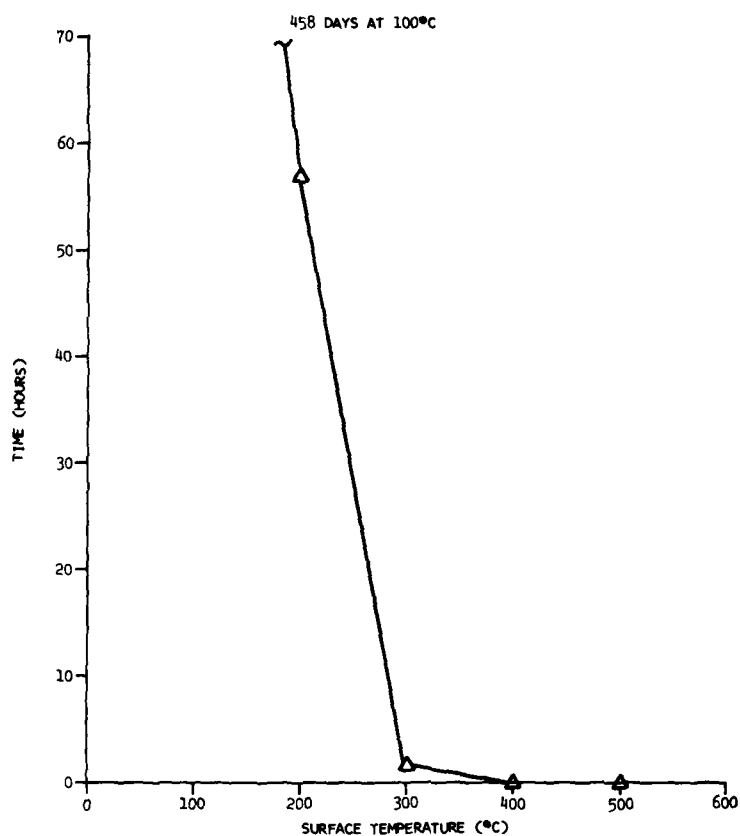


Fig. 5.6-2 — Time to initiation of "Purple Plague" as a function of temperature (gold coating on aluminum)

Table 5.6-1 — Maximum Temperature of External Gold Plated Layer on RAM Surface and Resulting Maximum Heat Flow Through MLI Blanket on the RAM Face

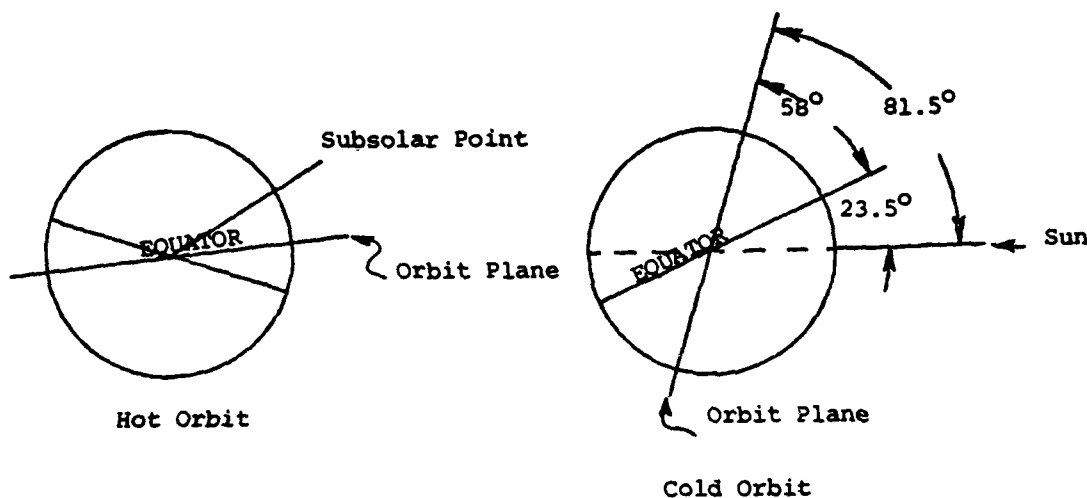
Fraction of Exterior Surface Covered with White Paint	$\epsilon$ (MLI) = 0.02		$\epsilon$ (MLI) = 0.01	
	T (°C)	Q (W)	T (°C)	Q (W)
0.0	377	481	426	322
0.01	345	393	382	248
0.05	265	226	283	129
0.10	210	147	220	80
0.20	148	84	153	21
0.50	65	35	67	18
1.00	4	16	5	8

Assumed Internal Temperature of Spacecraft: 20°C  
 Optical Properties: Gold  $\alpha = 0.29$   $\epsilon = 0.02$   
 White Paint  $\alpha = 0.22$   $\epsilon = 0.90$   
 Area of RAM Surface: 2.374 m<sup>2</sup>  
 Solar Constant: 1399 W/m<sup>2</sup> (max)

(SSPTA) to compute a set of maximum and minimum incident environmental flux intensities on all spacecraft surfaces. Table 5.6-2 summarizes the orbital and environmental parameters utilized to compute the two sets of incident flux intensities. In the assumed hot orbit, LASSII flies directly over the subsolar point and has a 59% suntime orbit with an orbital period of 90 min. In the assumed cold condition, the orbit plane is inclined  $58^\circ$  to the equator and has a minimum separation of  $81.5^\circ$  from the subsolar point. The attitude of LASSII is such that the  $-Z$  face is always viewing the Earth and the  $+X$  surface (the RAM surface) is facing in the direction of flight.

Table 5.6-2 — Orbital and Environmental Parameters  
Used to Define Hot and Cold Orbits

	Hot Orbit	Cold Orbit
Altitude	140 nmi	140 nmi
Solar Constant	450.4 btu/h/ft <sup>2</sup> 1420 W/cm <sup>2</sup>	408.6 btu/h/ft <sup>2</sup> 1288 W/cm <sup>2</sup>
Albedo	0.32	0.28
Earth IR	77.4 btu/h/ft <sup>2</sup>	73.0 btu/h/ft <sup>2</sup>
Orbital Inclination	$28.5^\circ$	$58^\circ$
% Suntime	59%	100%



Figures 5.6-3 and 5.6-4 show the transient environment flux intensities incident on the primary radiator surface for the hot and cold orbits, and Fig. 5.6-5 shows the orbital average heat rejection capability of the radiator for the same hot and cold orbits as a function of radiator temperature. Maximum and minimum spacecraft power dissipation are given in Table 5.6-3. It is apparent that for the maximum spacecraft internal power dissipation of 328 W (during a 25 min transmission period) a radiator temperature of at least  $0^\circ\text{C}$  would be sufficient to reject the power being dissipated. The transient heat gain or loss through the MLI blankets on the main body would have to be added to the spacecraft internal power dissipation to determine the net heat to be rejected by the primary radiator.

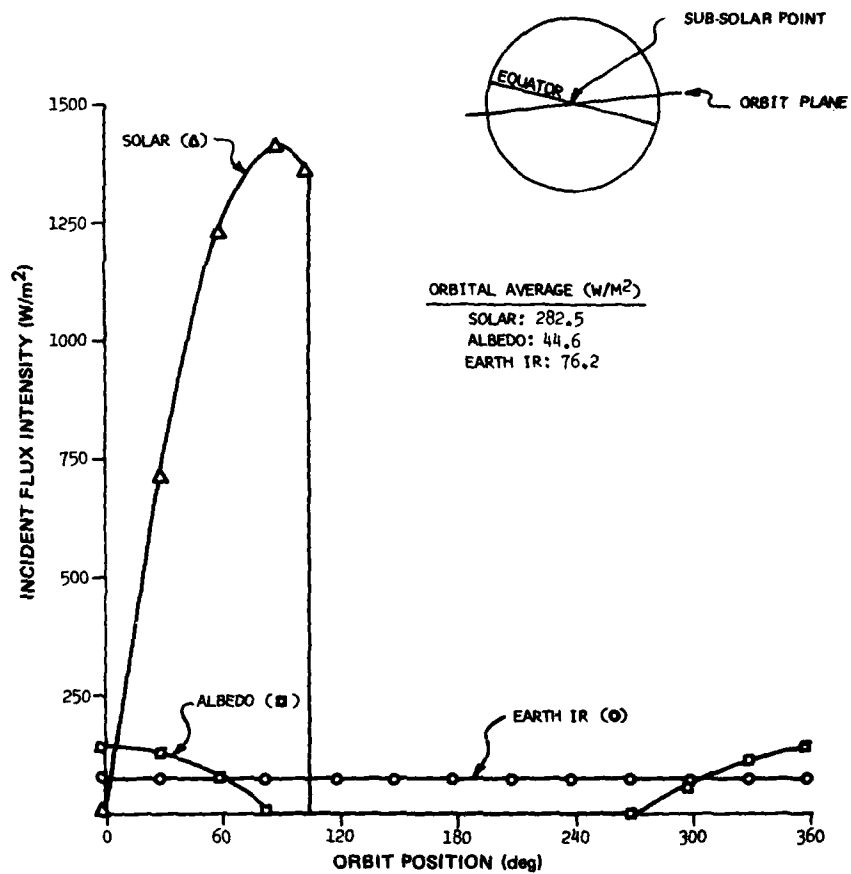


Fig. 5.6-3 — Environmental flux intensities incident on radiator — hot orbit

SZUSZCZEWICZ AND PALMA

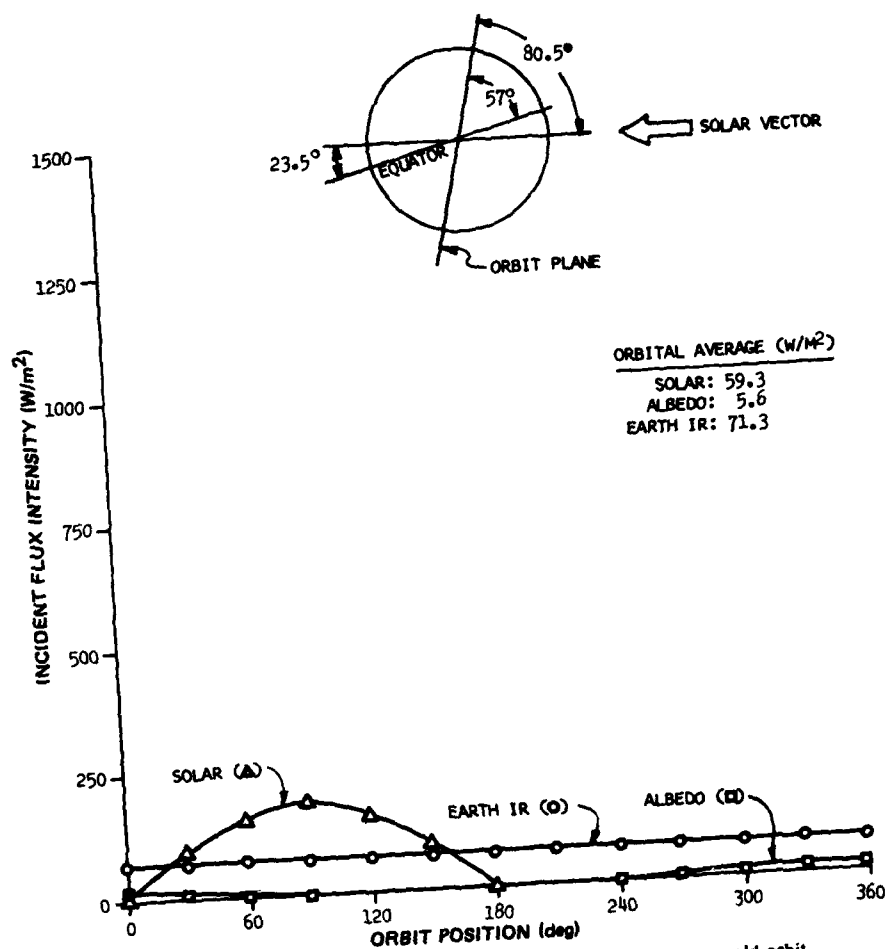


Fig. 5.6-4 — Environmental flux intensities incident on radiator — cold orbit

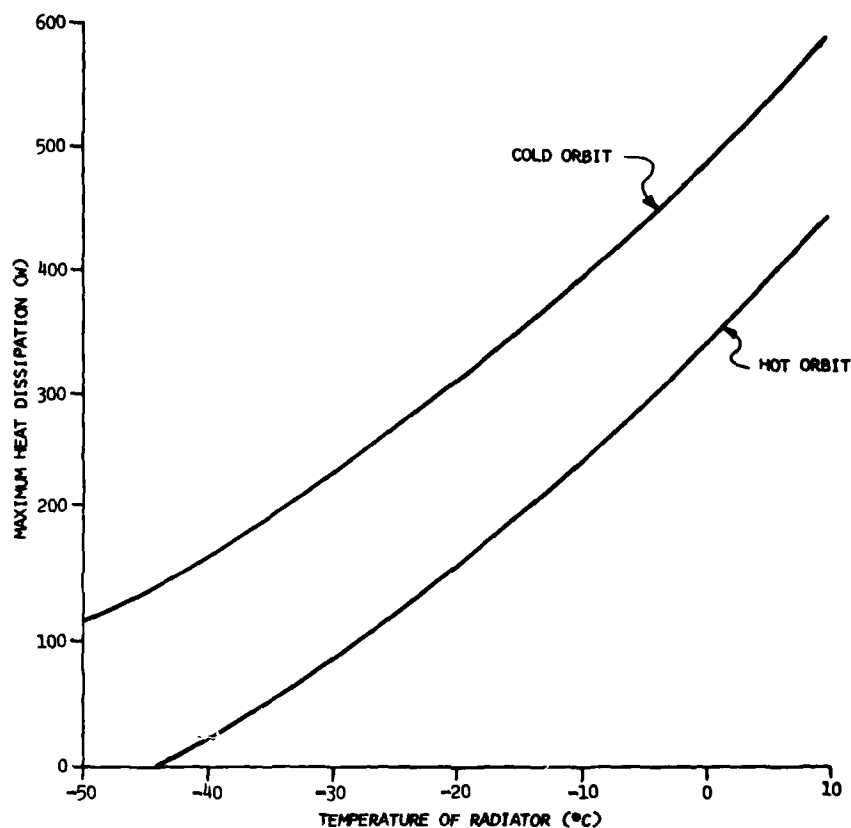


Fig. 5.6-5 — Orbital averaged heat rejection capability of radiator covered with conductive white paint NS43C (.22/.9)

Table 5.6-3 — Maximum and Minimum Power Dissipation (W) in LASSII Used for Thermal Design

Mission Timeline	Location		
	Body	+ Y Array	- Y Array
In Cargo Bay			
Container Closed	15/15	0/0	0/0
Container Open	133/15	160/0	160/0
Attached to Remote Manipulator	273/133	160/0	160/0
Free Flyer	328 <sup>(a)</sup> /66 <sup>(b)</sup>	160/0	160/0

<sup>(a)</sup> During 25.4 min period of data transmission 286 W dissipation internal to S/C during 1 orbit (90 min) (Science Data acquisition).

<sup>(b)</sup> Survival Mode.



As shown in Fig. 5.6-3, the primary heat rejection radiator receives direct sunlight for  $90^\circ$  of the orbit just prior to entering the shadow period. Also, as the orbit-sun angle changes so as to increase the time in shadow, the projected area of the radiator to the incident sunlight increases. This warming effect (radiator in full sun) will tend to automatically compensate for the decrease in interior spacecraft temperature during the following eclipse period. While the radiator is in full sunlight its total heat rejection capability at  $20^\circ\text{C}$  will be approximately 150 W. If the spacecraft power dissipation is higher than this amount there will be a transient warming of the spacecraft until LASSII enters the shadow of the Earth.

### The Hydrazine System

The design for the hydrazine system on LASSII is to mechanically mount the full system onto a single panel on the  $-X$  (anti-RAM) surface in the spacecraft. This panel is separated from the primary heat rejection radiator by a MLI blanket. Because the hydrazine has a minimum design temperature of  $+10^\circ\text{C}$ , thermal coupling of the liquid hydrazine system to the temperature-controlled interior region of LASSII is employed to maintain the hydrazine above  $10^\circ\text{C}$  at all times. The 150 lbf hydrazine engine will be thermally isolated from the interior of the spacecraft because of its high temperature during firing ( $1800^\circ\text{F}$ ), and heaters will be mounted directly on this engine for temperature level control during periods of time when it is not firing.

### Electrical Heaters

LASSII has two solar cell arrays. Because of the potential blockage of sunlight by the main body of the spacecraft, and the TDRSS antenna, only the array not being shadowed will be utilized as the primary (regulated) energy source. The other (shadowed) array will generate unregulated power whenever it is exposed to sunlight, and the TCS will utilize this secondary power source to energize thermal heaters. A three-tier minimum temperature setting for the thermostatically controlled heater will be incorporated in the spacecraft. The first tier of thermostats will be set (approximately) at  $+15^\circ\text{C}$  and will be connected to the unregulated power bus. It will provide temperature level control for the interior of the spacecraft. If the power being generated by the secondary array is insufficient to maintain the spacecraft temperature above  $+15^\circ\text{C}$ , the primary array will be utilized as an energy source to keep the hydrazine temperatures above  $+10^\circ\text{C}$ . The second set of heaters located on the hydrazine system will be powered from regulated bus. It will have a  $+10^\circ\text{C}$  set point. These heaters will be electrically connected to the primary array wherever measured hydrazine temperatures drop to  $+10^\circ\text{C}$  and will dissipate whatever power is necessary to maintain the temperature of the hydrazine system above  $+10^\circ\text{C}$  at all times. The third tier of thermostats will be set at approximately  $-30^\circ\text{C}$  and will be powered by the primary array to provide a minimum spacecraft temperature under adverse conditions. The liquid loop thermal control system will thermally uncouple the radiator from the interior of the spacecraft before any heaters are energized.

### Thermal Control in the Orbiter

The  $2.37\text{ m}^2$  radiator on LASSII will be utilized as the primary heat rejection surface while the payload is stowed in the cargo bay of the Orbiter. LASSII will utilize a separate canister while it is in the Orbiter, and there will be a temperature-controlled plate on the interior of the canister that will be adjacent to and have a direct radiative view of the radiator on LASSII. Figure 5.6-6 shows the heat transfer capability of this thermal control system as a function of the temperatures of the two adjacent plates. The heat being accepted by the canister plate must be rejected to space either via the Orbiter provided liquid loop or by a dedicated radiator/liquid loop system which is a part of the canister design. Table 5.6-4 summarizes the heat rejection capability of a (dedicated) sunlit radiator covered with silverized Teflon as a function of radiator temperature. For 133 W of power dissipation inside LASSII while stowed in the canister, a spacecraft temperature near  $20^\circ\text{C}$  is maintained with a  $10^\circ\text{C}$  canister plate and

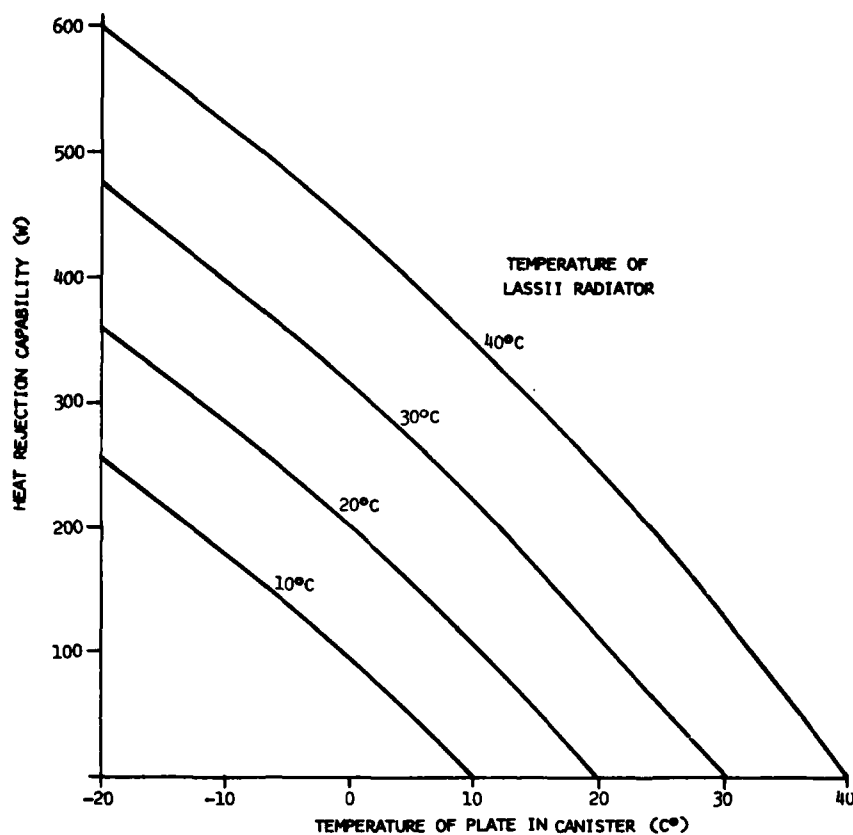


Fig. 5.6-6 — Heat rejection capability of primary radiator on LASSII while stored in canister in cargo bay of Shuttle  
E Radiator = 0.9  
E Canister = 0.9

Table 5.6-4 — Heat Dissipation Capability of Silver Teflon Radiator as a Function of Temperature of Radiator

Temperature (C°)	Heat Dissipation (W/m <sup>2</sup> )
-20	37
-10	67
0	100
10	137
20	178

approximately 1 m<sup>2</sup> of a silverized Teflon covered radiator. Temperature control of the two solar cell array assemblies while inside the canister can also be provided by mounting temperature-controlled plates adjacent to the arrays. The need for these additional cooling plates will be determined after assessing the desirability or feasibility of reorienting the Shuttle prior to opening the canister so as to eliminate any direct solar energy from entering the open canister.

### Thermal Control of the Solar Cell Arrays

The ends of the solar cell arrays have been designed as radiator surfaces for power dissipation of internally mounted instruments as well as any heat leak from the solar cells. The interior surface of the rotating solar cell arrays will be insulated so that the environmental fluxes absorbed by the solar cells can be thermally uncoupled from the radiating surfaces at the ends of the arrays. Heater power will be required on the individual instruments to keep minimum temperatures above acceptable lower limits in selected cold orientations. Table 5.6-5 shows the predicted orbital average temperatures for the solar cells and the interior instrument compartments with conductive white paint as low  $\alpha/\epsilon$  thermal coating. The use of gold on these radiator surfaces would lead to elevated temperatures in the instrument compartments whenever the radiator was in full sun.

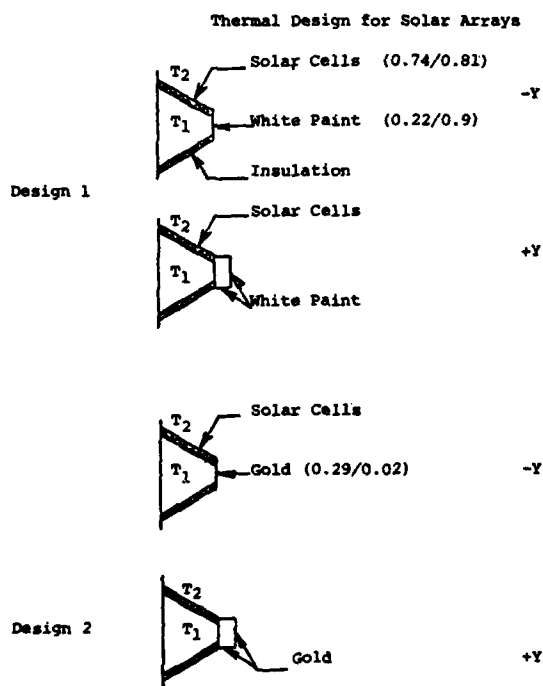


Table 5.6-5 — Thermal Design for Solar Arrays

	Design 1						Design 2					
	Hot Orbit		Cold Orbit				Hot Orbit		Cold Orbit			
			+Y		-Y				+Y		-Y	
			Facing Sun		Facing Sun				Facing Sun		Facing Sun	
T <sub>1</sub> (°C)	+Y	-Y	+Y	-Y	+Y	-Y	+Y	-Y	+Y	-Y	+Y	-Y
T <sub>1</sub> (°C)	-75	-75	-17	-84	-84	14	192	62	375	-63	-63	485
T <sub>2</sub> (°C)	8	8	8	-79	-79	14	8	8	8	-79	-79	14

## 5.7 Structural and Mechanical Configuration

The configuration of the LASSII spacecraft (Fig. 4-1) has been designed to provide maximum flexibility as a scientific platform. The spacecraft consists of a stabilized platform (stator) and a spinning platform (rotor). The stator contains experiments, the attitude control system, the reaction control system, most of the electrical power system, the RF system, and other housekeeping and control systems. The rotor contains the solar arrays and the spinning experiments. NRL/STC drawing number AD-PD-M0001 (Fig. 4-1) shows the overall configuration and experiment locations. The LASSII weight report is shown in Table 5.7-1.

Table 5.7-1 — LASSII Weight Report

1.	Structure	273 lb
2.	Electrical Power System	850 lb
3.	Reaction Control System	124 lb
4.	Attitude Control System	163 lb
5.	Radio Frequency System	105 lb
6.	Telemetry Command System	185 lb
7.	Ordnance	60 lb
8.	Thermal Control System	134 lb
9.	Experiments	212 lb
10.	Consumables	759 lb
11.	Balance Weights	25 lb
12.	Margin	172 lb

Lift-Off Weight                      3062 lb

### LASSII Mechanical Drawings

Fig. 4-1	AD-PD-M0001	Spacecraft Mechanical Configuration
Fig. 5.7-1	AD-PD-M0002	Hydrazine Installation
Fig. 5.7-2	AD-PD-M0003	Pallet Concept

The stator design is a simple box configuration. The box configuration provides a maximum usable volume and a simple structural support system. The stator size was optimized to meet the requirements of the experiments, the rotor, and the antennas. Exterior surfaces will be removable to provide easy access to the interior. Where practical, equipment mounting will be modularized to provide easy removal and replacement. The equipment will be mounted on decks within the body and positioned to provide optimum center of gravity placement for the spacecraft. To meet the gold surface area requirement, foldout panels are installed on the lower surface.

The rotor consists of three segments, a solar array section on either side of the stator and an experiment section. The experiment section mounts to the end of a solar array section. The two solar array sections are mounted to a common shaft and are coupled by a common drive system. Slip rings provide the electrical interface between the rotor and the stator. The support structure for the solar arrays will be alike. The experiments will be mounted according to their desired view angle and to optimize the balance of the rotor.

LASSII will be mounted in the Shuttle Orbiter on its own pallet. The pallet provides environmental protection doors (sunshield) and a thermal protection system (TPS) to protect LASSII when onboard the Orbiter. The Remote Manipulator System (RMS) will be used to deploy and recover LASSII. Appropriate targets will be provided to ensure the correct placement of LASSII in the Shuttle bay for recovery. NRL STC drawing number AD-PD-M0003 illustrates the basic pallet concept.

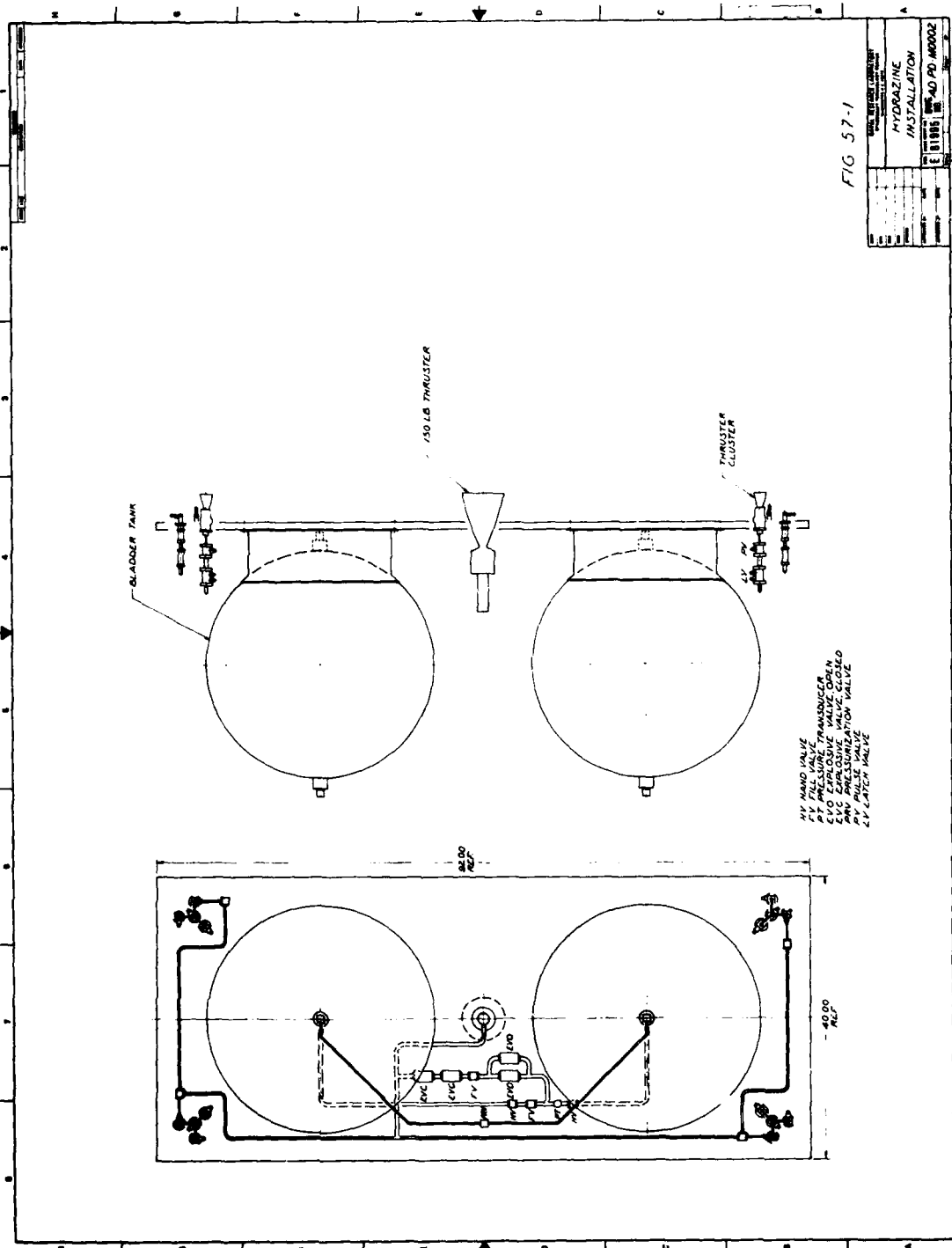


Fig. 57-1 — Hydrazine installation

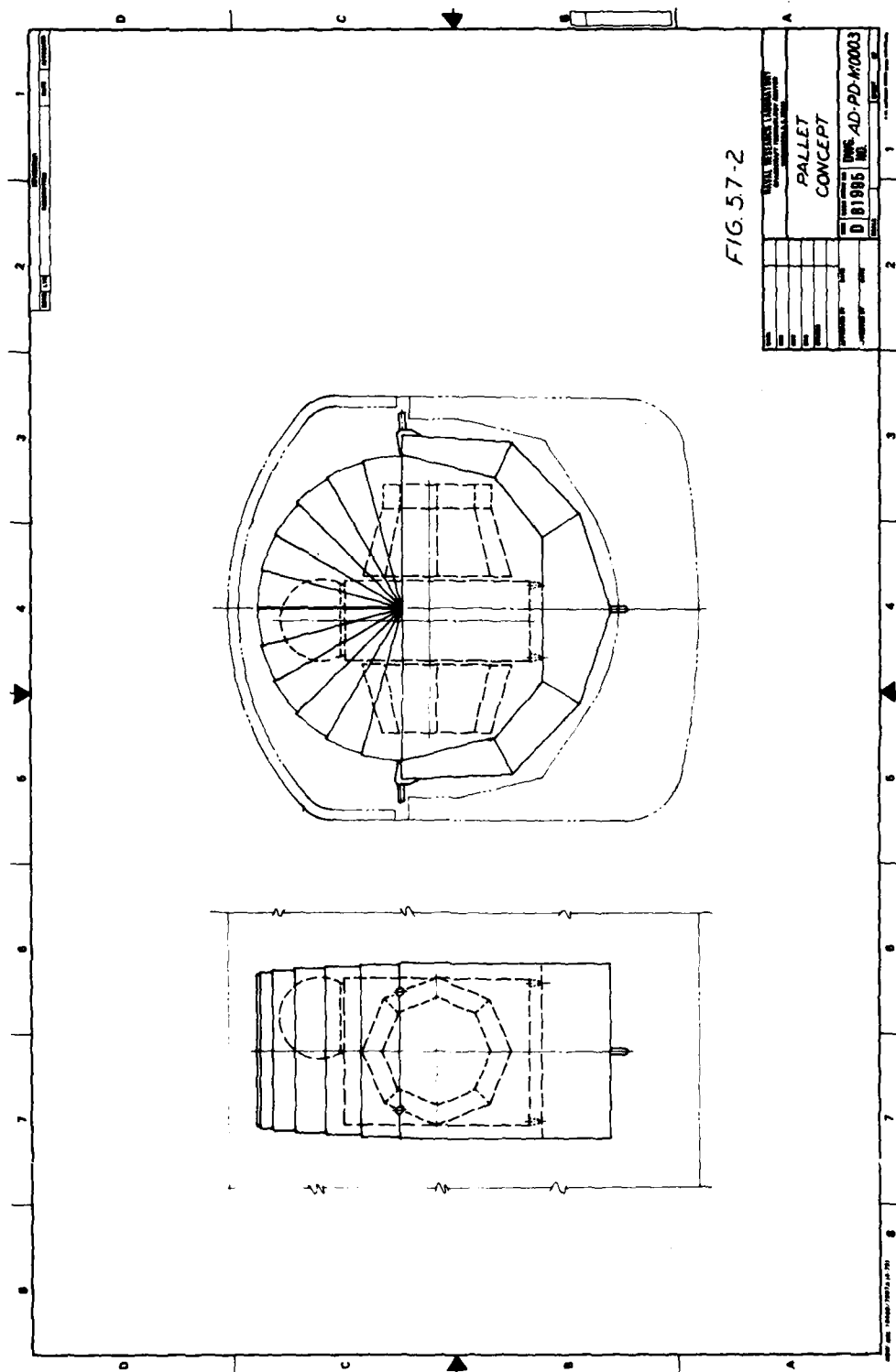


Fig. 5.7-2 — Pallet concept

The basic structure of LASSII will consist of an aluminum framework with aluminum honeycomb panels for exterior surfaces and solar array substrates. The framework will be constructed with extrusions, formed sheetmetal, and machined parts. The framework design will include features to allow incorporation of the thermal protection system. Internal support structure will be provided to support mounting decks and equipment.

Several of the LASSII experiments require sensor covers, booms, and antennas. Because of the limited space within the pallet, the booms and antennas will have to be stowed until after LASSII is separated from the orbiter. The deployable elements will be released by ordnance devices. The elements will have spring-loaded hinge mechanisms to position and lock the elements in place. Prior to the retrieval of LASSII, the deployed elements will be jettisoned. This is more cost effective than designing and qualifying a retrieval mechanism for each element. Sensor covers will be handled according to the requirements of each experiment.

The reaction control system consists of two 32-in. diameter bladdered spherical tanks, a 150-lb hydrazine motor, four 5-lb hydrazine motors, twelve 0.2-lb motors, and associated plumbing and valves. Each tank has a capacity of approximately 415 lb of hydrazine at a 67% fill.

The hydrazine system and its support structure are designed as a modular unit. The unit will form the aft closer of the spacecraft. The 0.2- and 5-lb hydrazine motors will be grouped in four clusters, one at each corner of the module. The clusters are identical and interchangeable. The 150-lb motor is located at approximately the center of the unit. The spacecraft center of gravity will be adjusted to coincide with thrust vector. This modular unit concept allows the hydrazine system to be fabricated and tested independently of the spacecraft. Table 5.7-1 lists the three mechanical drawings included in this document.

## **5.8 Product Assurance and Quality Control**

### **5.8.1 Introduction**

Maximum mission reliability will be achieved through a comprehensive product assurance program implemented throughout design, development, fabrication, and test with the twofold purpose of:

- Maximizing the inherent design reliability of the spacecraft.
- Eliminating/precluding any latent defects from the flight hardware.

This plan defines the product assurance program to be implemented by NRL's Spacecraft Technology Center to achieve this end.

Maximized inherent design reliability will be assured through a thorough reliability analysis program beginning early in the design process and continuing through design finalization. The elements of this reliability analysis program will include system and subsystem trade-off studies, optimized redundancy implementation studies, failure mode and effects analyses (FMEAs), parts selection evaluations, electrical stress analyses, design margin analyses and tests, criticality analyses, reliability predictions, and design reviews.

The elimination of latent defects from flight hardware will be accomplished by inspections and tests beginning at the parts level and continuing throughout hardware fabrication and test at all levels up to and including the spacecraft. This will be initiated by the high-reliability procurement, screening, and destructive physical analysis of the parts, followed by tests and inspections at the module, subsystem, and spacecraft levels.

Precluding the introduction of latent defects in the flight hardware will be accomplished by a stringent set of procedures, reports, and controlling documentation that will assure complete control over spacecraft and subsystem configuration, test, and repair. It will verify that all required actions have been taken.

To assure comparable reliability achievement by procured units and subsystems, NRL/STC will impose the applicable elements of this product assurance program on participating contractors and monitor their compliance.

### 5.8.2 Program Overview

The Product Assurance Plan is based on implementing the NRL/STC design and monitoring techniques and procedures which have been developed on previous spacecraft programs. The key features of this plan are:

#### **Reliability Analysis Program**

This analysis program provides for a controlled iterative implementation of the design analysis and review techniques that identify reliability achievement and enhancement potential. The individual elements of the reliability analysis program as they apply during the conceptual design period and at the subsystem and system levels during detailed design and development are:

*Preliminary Studies and Evaluation* — These early reliability studies will include evaluations of redundancy tradeoffs, preliminary Failure Modes and Effects Analyses (FMEAs) with emphasis on equipment interfaces and redundancy implementations, technology selection, parts selection evaluations, preliminary reliability math models with projections of reliability achievement potential, and a preliminary Spacecraft Single Point Failure Summary (SPFS).

*Subsystem Reliability Analyses* — As design detail becomes available, the reliability analysis will be expanded to include electrical stress analyses, design margin analyses and tests, detailed FMEAs, and reliability predictions. These analyses will be performed only on those circuits that have not been subjected to a previous analysis.

*System Reliability Analysis* — As the unit and subsystem analyses are updated, they will be used to update and refine the spacecraft system level FMEA, SPFS, math model, and reliability prediction to allow for assessment of further reliability improvement.

*Design Review* — Both formal and informal design reviews will be implemented to evaluate the design and verify maximized reliability achievement.

#### **Parts Program**

The parts program describes the techniques and methods by which parts reliability will be maximized relative to factors which affect parts reliability. It covers four major parts activities that make up any high-reliability parts program.

1. Parts selection
2. Parts procurement, qualification, and screening
3. Destructive physical analysis
4. Receiving inspections and tests



### **Component Procurement Program**

This program describes the controls and procedures that will be implemented to assure that procured components are fabricated with a high reliability and will not degrade spacecraft performance. The basic approach described is to require contractors to adhere to the reliability plans and practices that would exist if the item were developed in-house by NRL/STC.

### **In-House Component Processing**

The in-house component fabrication, assembly, test, and repair will be controlled through implementation of the NRL/STC Procedure STC-101, Flight Hardware Fabrication, Test and Repair.

### **System Test Program**

The test program emphasizes integration and acceptance testing. Qualification testing will be performed for specific environmental parameters whenever analyses indicate a less than acceptable design margin. Acceptance tests will consist of verification by analysis and verification by test of the ability of the spacecraft to perform in specified environments.

NRL/STC Procedure STC-101 is the governing document for establishment of more detailed QC procedures to be employed during spacecraft integration and test. The release sheets, subsystem repair action logs, and spacecraft log, along with any discrepancy reports will be maintained by QC throughout the fabrication and test period to assure that the accepted hardware configurations and repair history are known.

### **Failure Reporting and Analysis**

The failure reporting system provides a timely and appropriate evaluation of failures, discrepancies, and/or malfunctions that are directly related to the design and test program. It is a closed-loop system developed by STC for use on previous programs which requires the initiation of a failure report using a Discrepancy Report (DR) and a subsequent failure analysis and corrective action prior to close out.

## **5.9 Orbital Mechanics Analysis**

### *5.9.1 Introduction*

A study was conducted to demonstrate the feasibility of using TDRSS to accomplish the tracking and orbit determination requirements of LASSII and LASSII-Shuttle missions. Both a tandem and an elliptical relative orbit mode were studied. Results of a full-scale simulation of the tandem mode are provided. Figure 5.9-1 describes the tracking geometry of the mission. The coorbital (tandem) mode is shown in Fig. 5.9-2, and the elliptical relative orbit mode is shown in Fig. 5.9-3.

The satellite-to-satellite tracking problem is addressed in Refs. 70, 71, and 72. Specific performance predictions using the TDRSS system are considered in Ref. 71. No previous studies deal with the coorbital tracking problem which is specifically addressed here. Two specific configurations are studied in detail.

### *5.9.2 Tracking Simulation Results*

A full-scale simulation of the tandem mode of operation has been carried out. It is assumed that both Tracking and Data Relay Satellites are operational in a near circular synchronous equatorial orbit 120° apart. A realistic model of the perturbing forces that act on the LASSII/Shuttle pair is used.

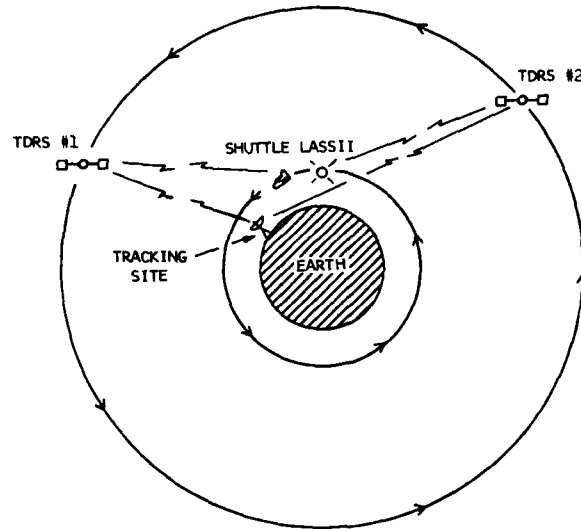


Fig. 5.9-1 — Tracking geometry

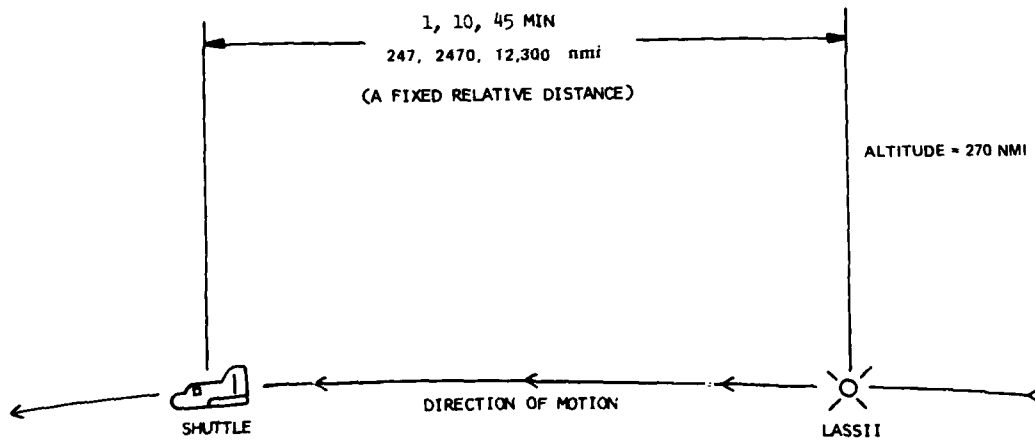


Fig. 5.9-2 — Coorbital (tandem) mode

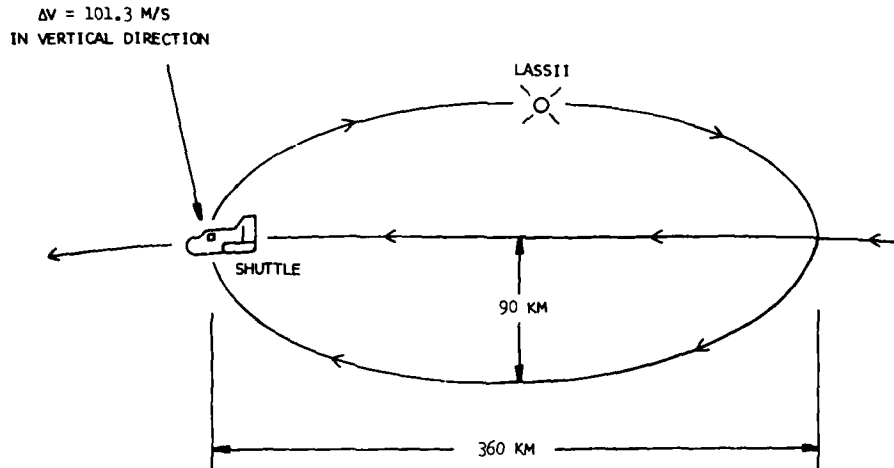


Fig. 5.9-3 — Elliptic relative orbit mode

These include the effects of  $J_2$  (oblateness),  $J_3$ ,  $J_4$  (higher order gravity harmonics), atmospheric drag, and luni-solar effects. The most important disturbing force is atmospheric drag since the area/mass ratios are different for each satellite. The gravitational effects act nearly the same in each satellite pair and thus tend to cancel when studying the relative motion.

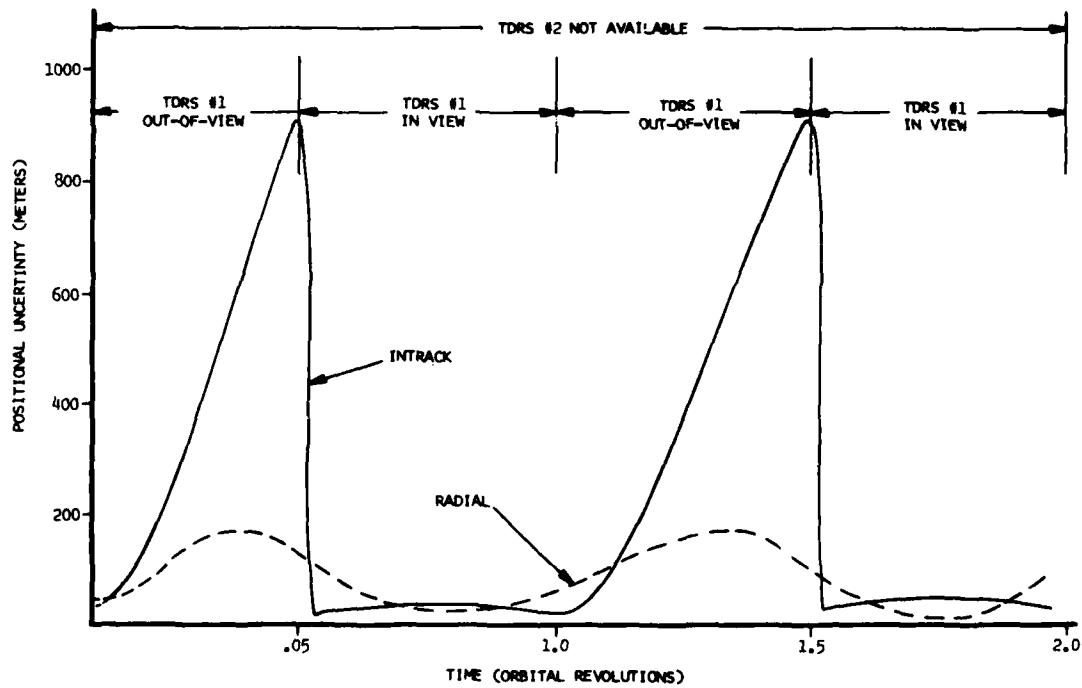
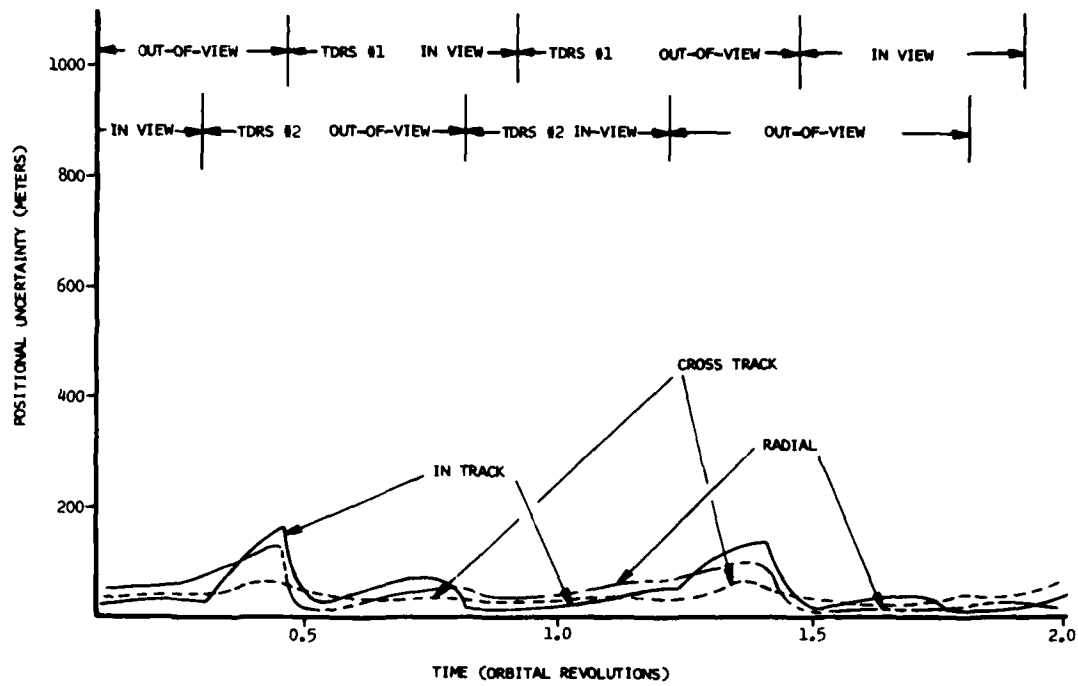
Figure 5.9-4 describes the positional error of all three components of the relative state when tracking data is received from both TDRSSs. A timing error of 20 ns (20 ft) is assumed for the range difference data. Note that two components are in error more than 100 m. The largest error appears to be in the in-track component. This is mainly due to the 10-min period in which the satellite pair is out of view of both tracking satellites. If only one tracking satellite is available, the in-track position error grows to nearly a kilometer as shown in Fig. 5.9-5. In this case the satellite pair is out of view of TDRSS for nearly 45 min. The radial and cross-track error do not grow appreciably during this time period. These errors are largely due to the unpredictable effects of atmospheric drag encountered at the 250 km altitude. They would diminish greatly for a higher altitude satellite pair.

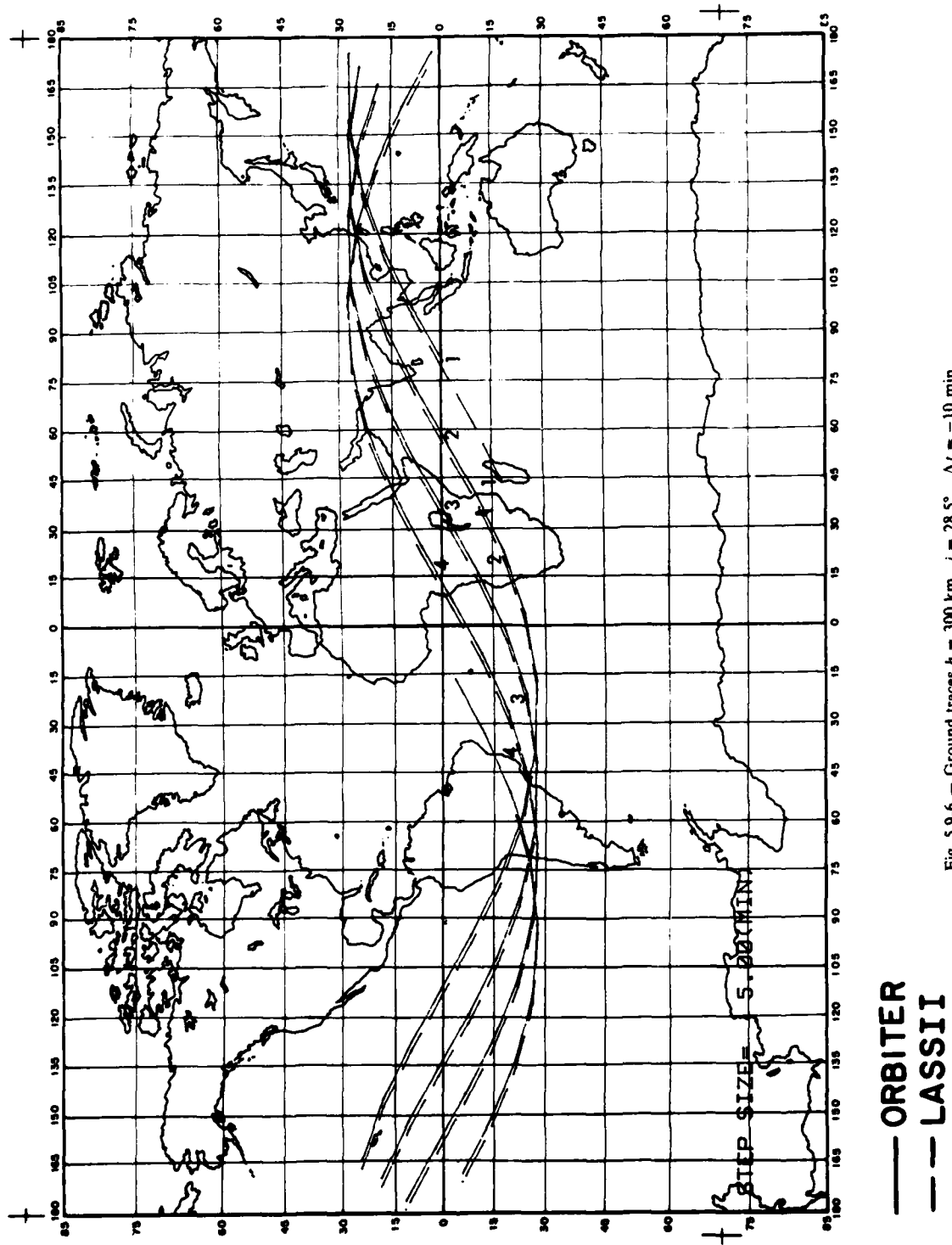
### 5.9.3 Ground Traces

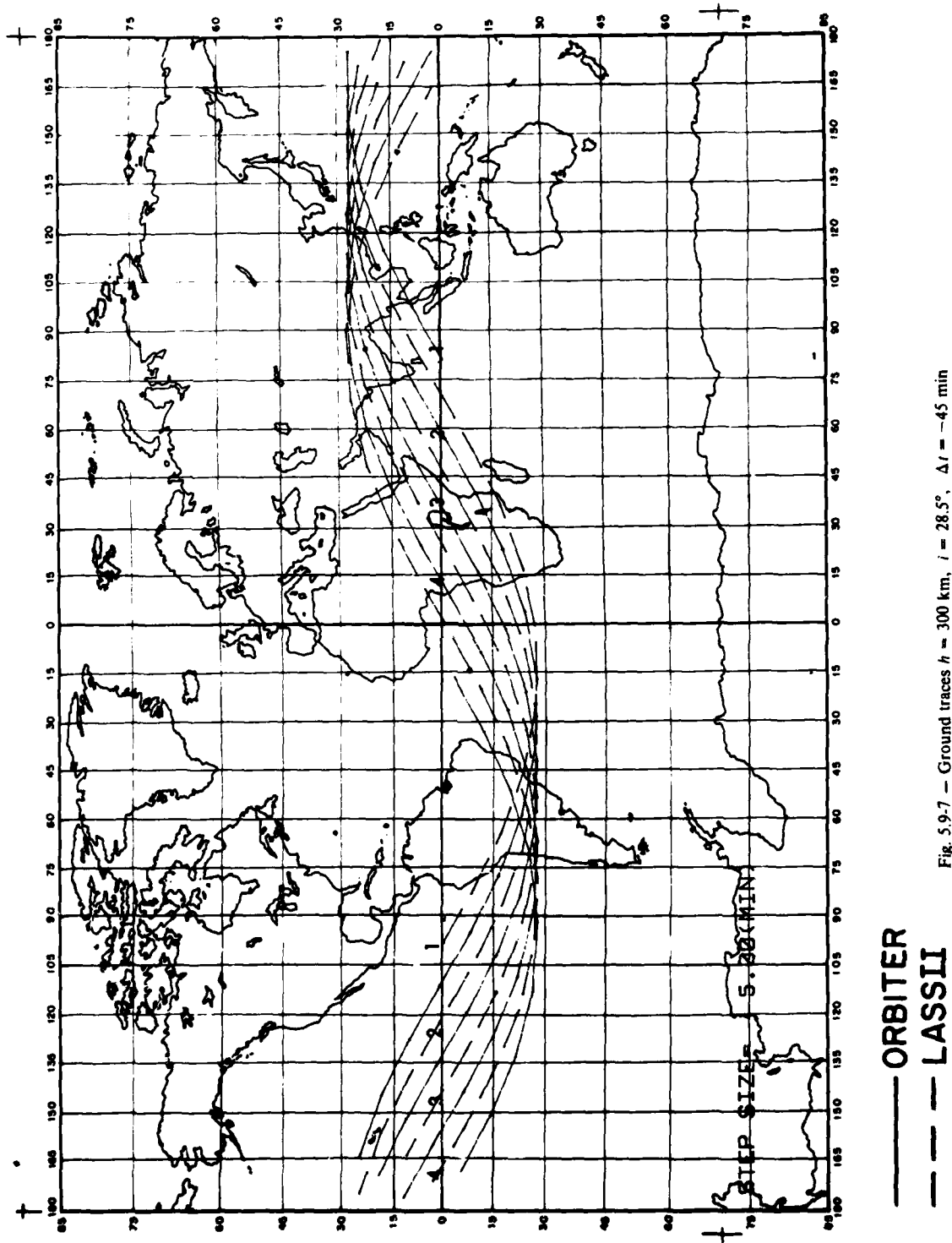
Figures 5.9-6 through 5.9-9 show typical ground traces for the orbiter and LASSII. The inclinations of both are  $28.5^\circ$ . Figures 5.9-6 and 5.9-7 are for altitudes of 300 km and with LASSII located 10 and 45 min, respectively, behind the Shuttle. The beginning of each orbit is numbered for each of the four complete revolutions shown. The slight displacement of the orbits is due to the rotation of the Earth over the 10 to 45 min time displacement. The two orbits coincide in inertial space.

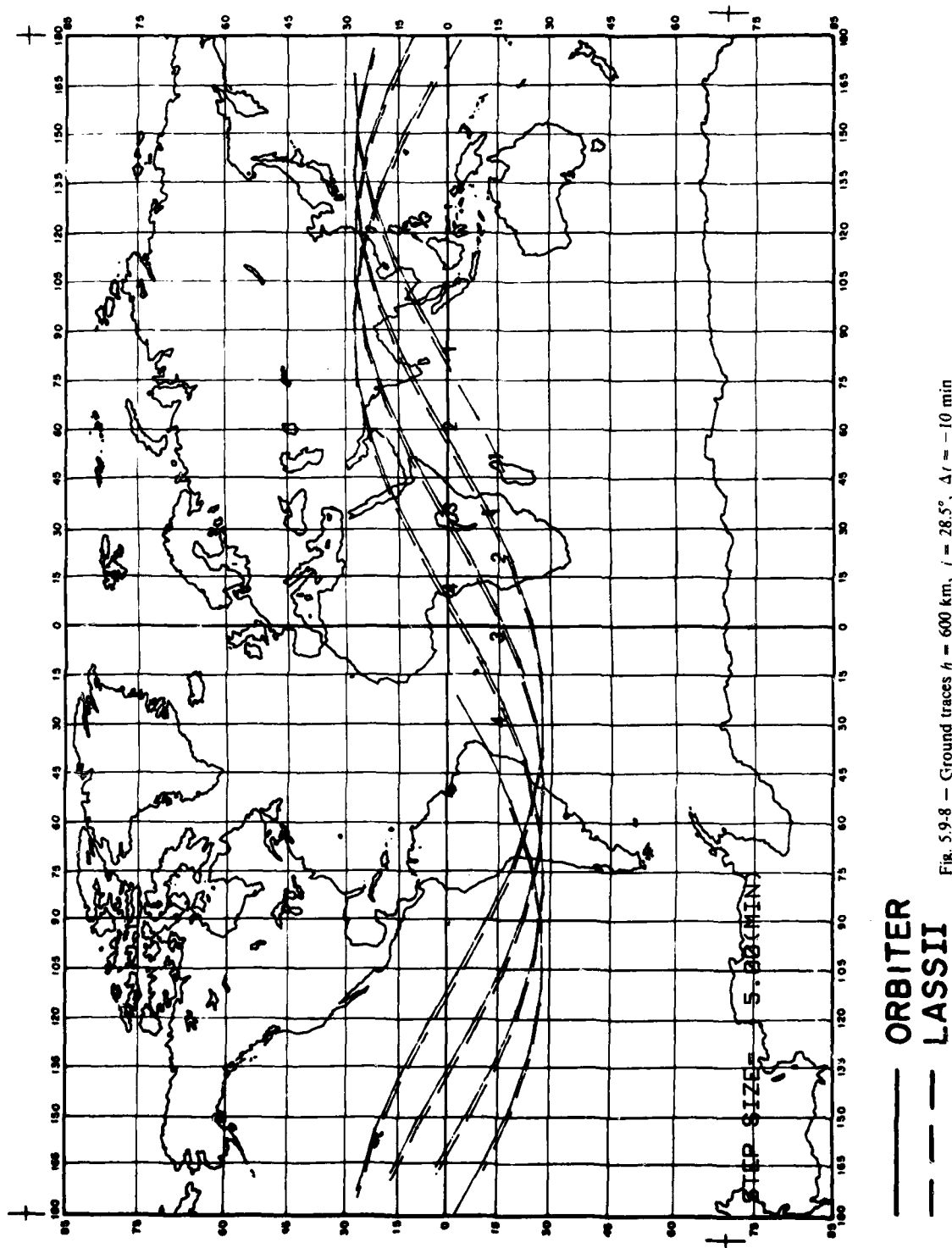
Figures 5.9-8 and 5.9-9 are for altitudes of 600 km but otherwise similar to Fig. 5.9-6 and 5.9-7. The difference in altitudes means the 600 km orbit will have one less revolution per day, and this is exhibited by the slightly wider spacings in latitude.

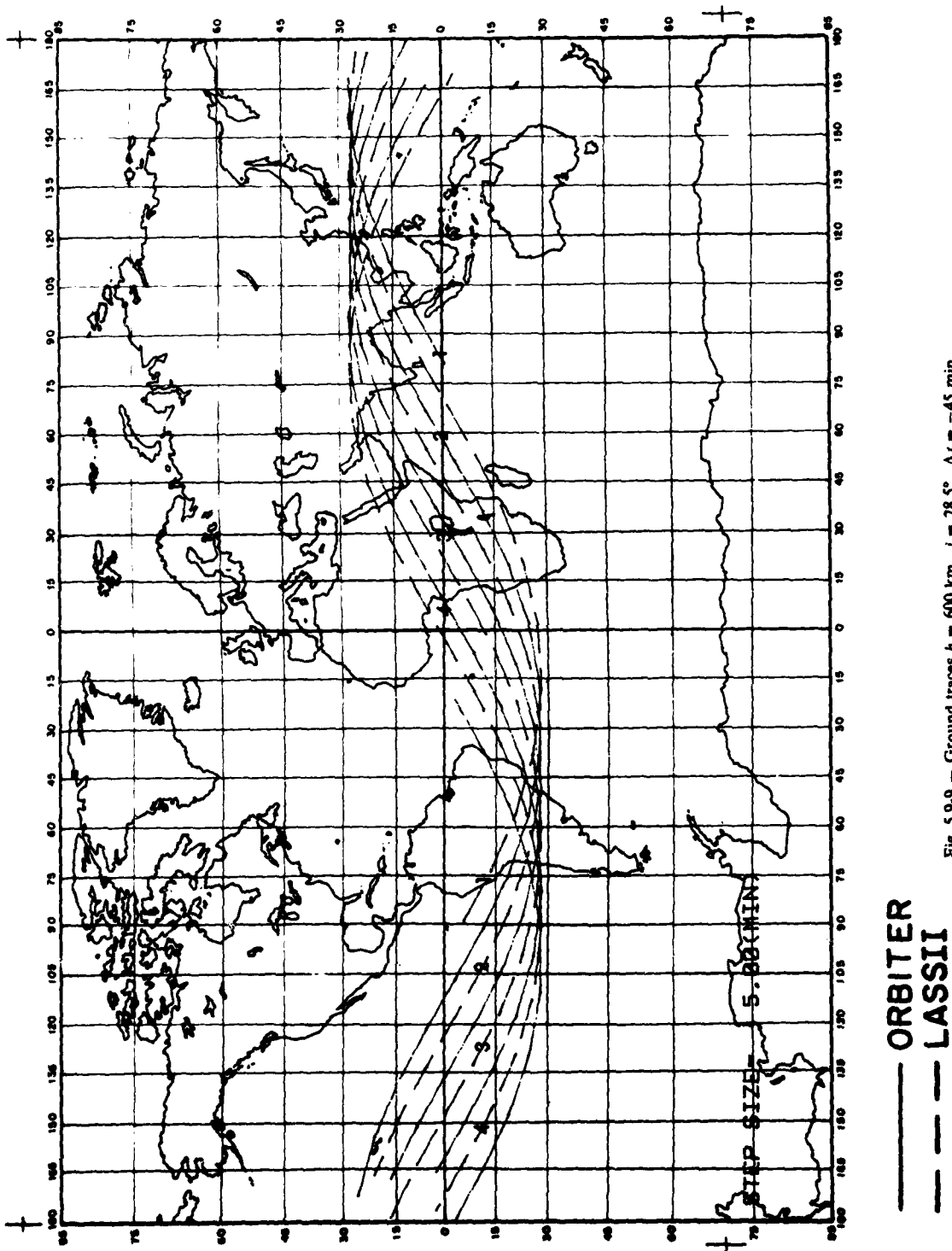
Figures 5.9-10 through 5.9-13 are for LASSII and the orbiter at  $57^\circ$  inclination orbits but otherwise similar to Figs. 5.9-6 through 5.9-9.













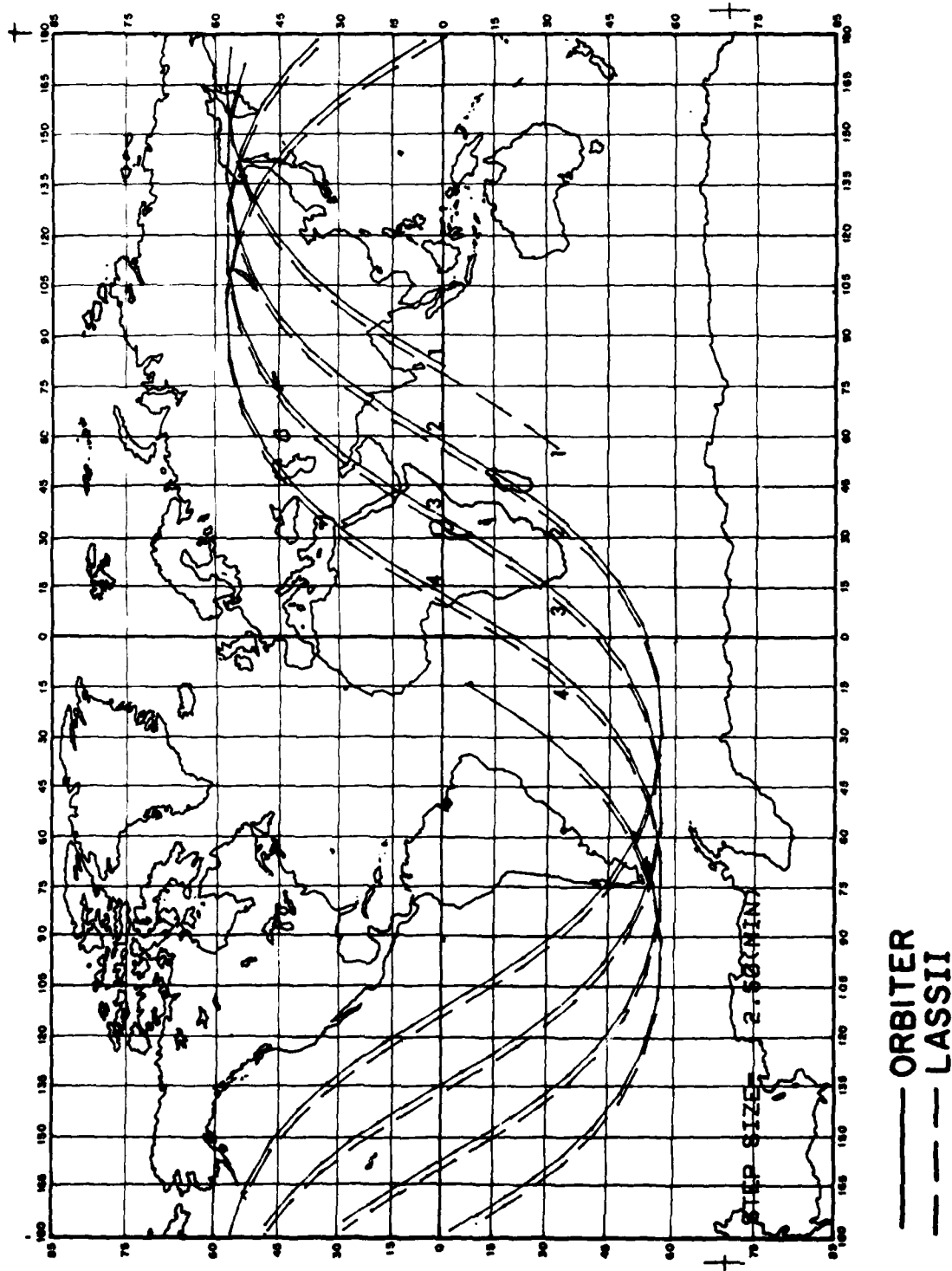
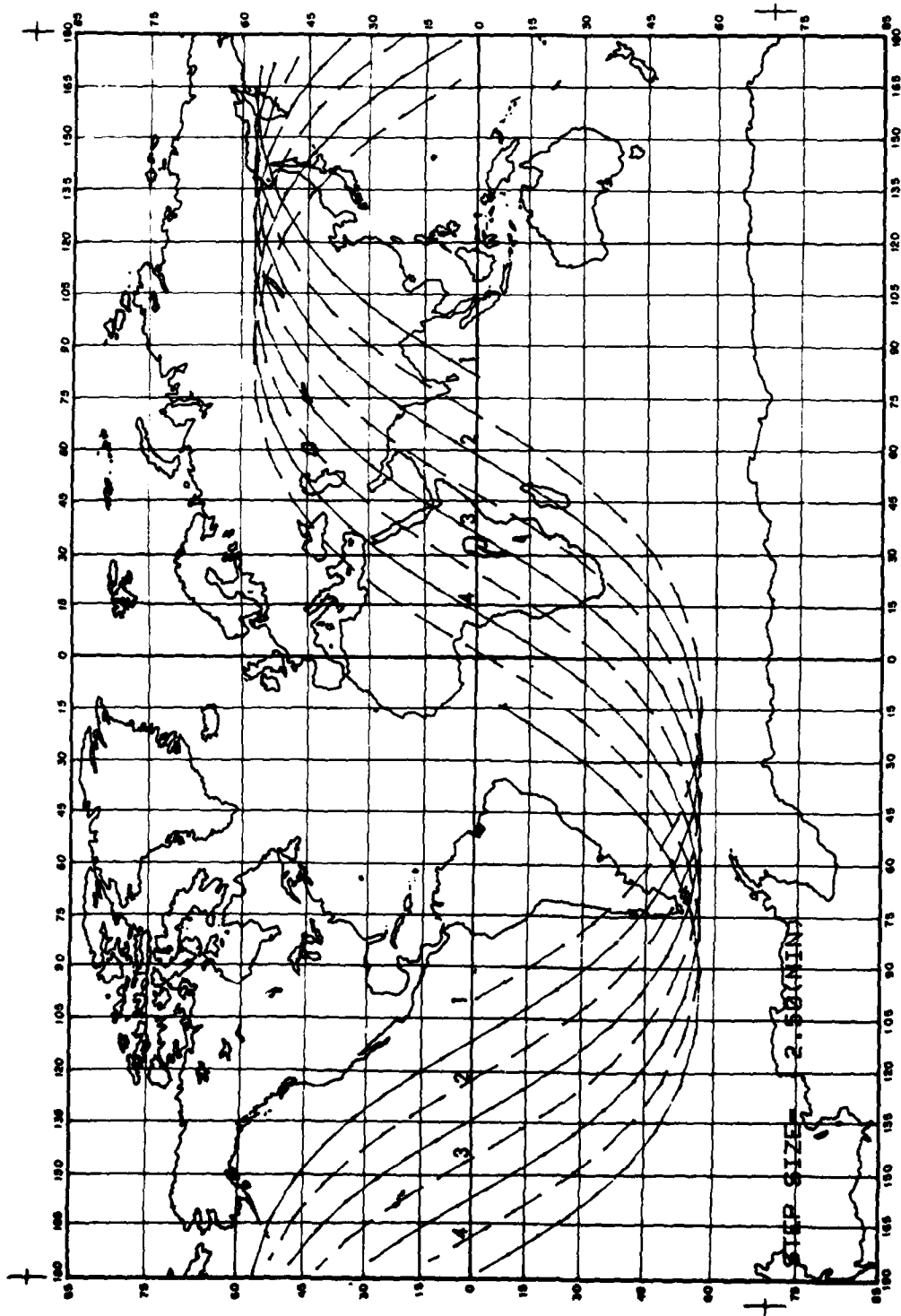


Fig. 5.9-10 — Ground traces  $h = 300$  km,  $i = 57^\circ$ ,  $\Delta t = 10$  min



— ORBITER  
 - - - LASSII

Fig. 5.9-11 — Ground traces  $h = 300$  km,  $i = 57^\circ$ ,  $\Delta t = -45$  min

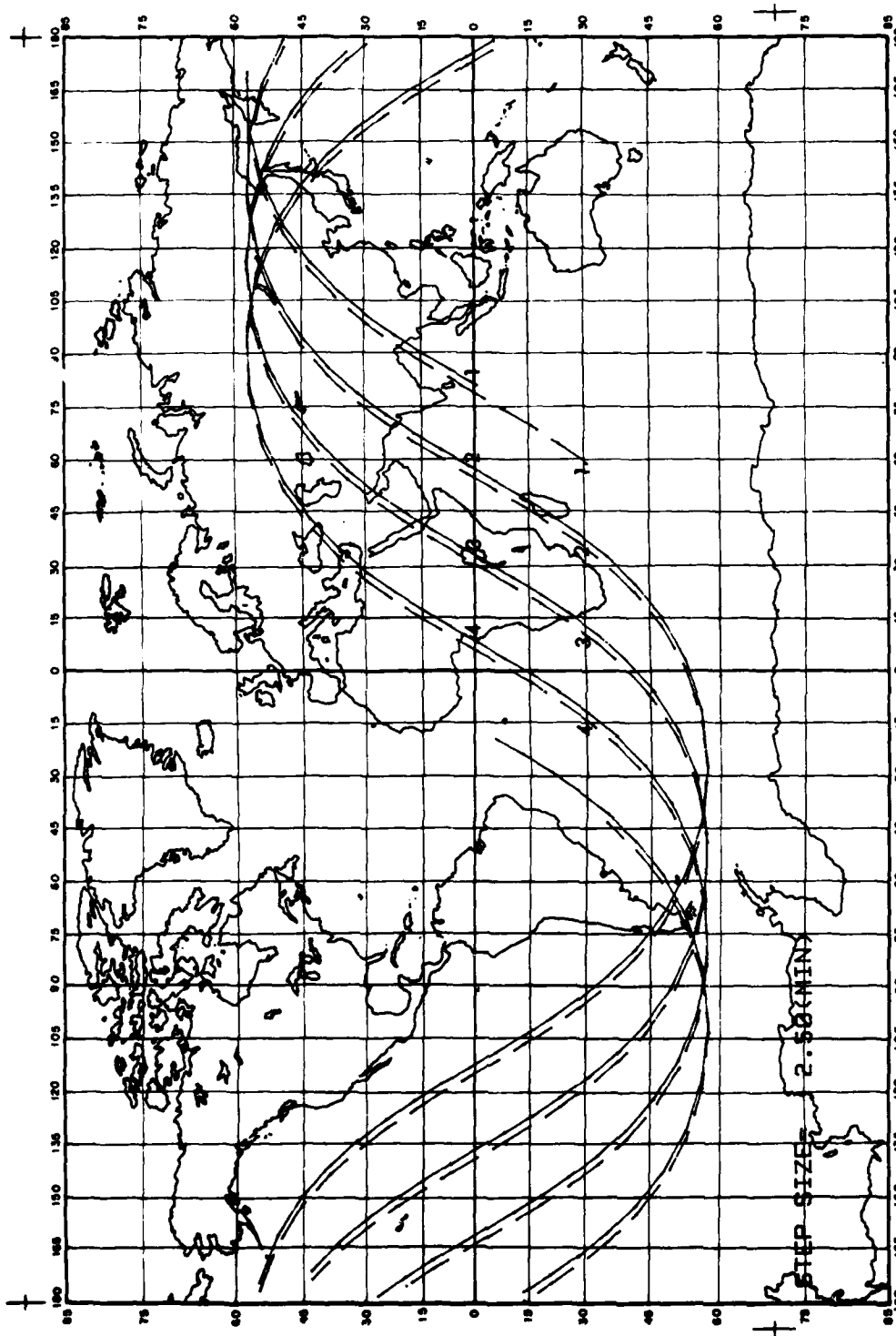
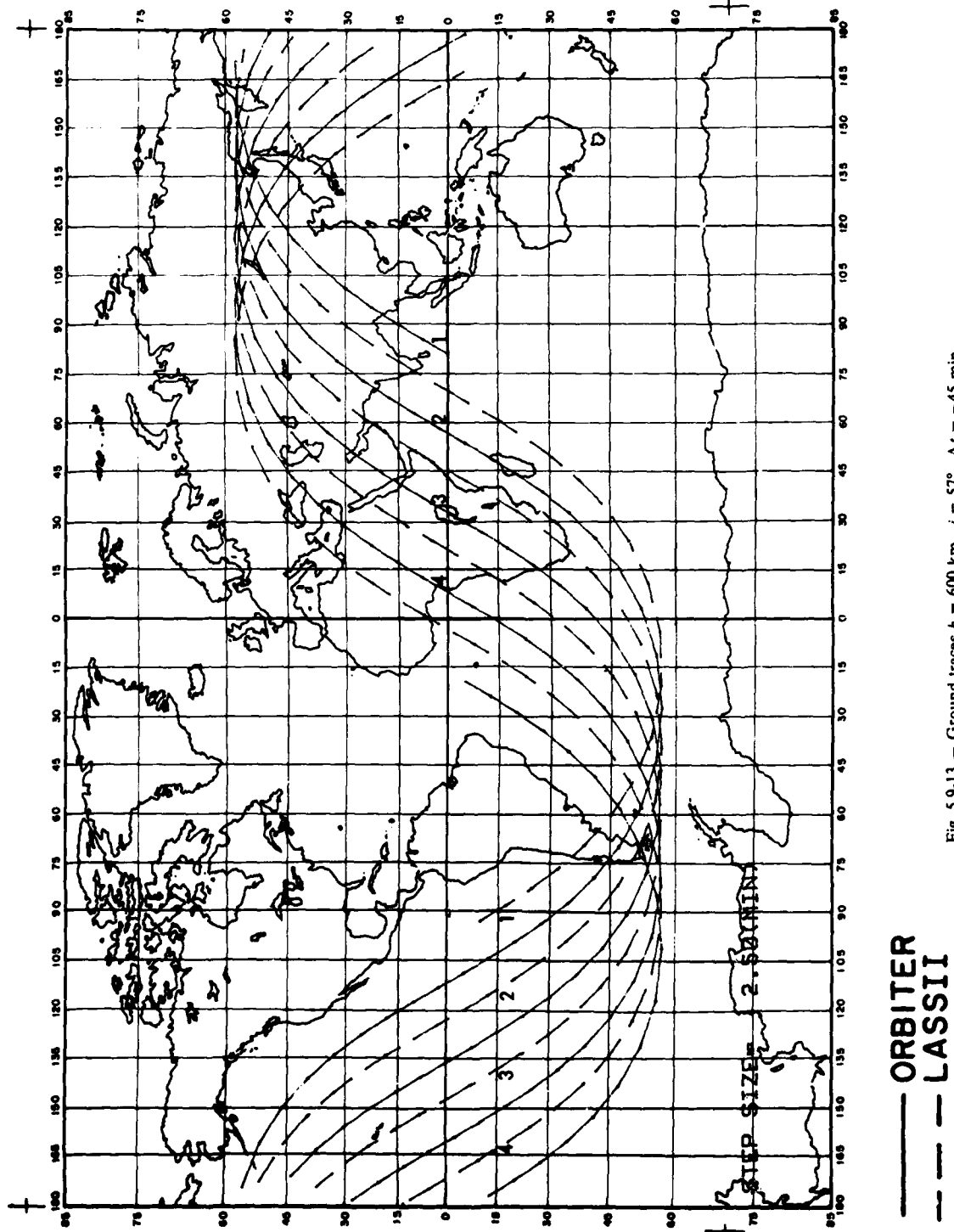


Fig. 5.9-12 — Ground traces  $h = 600$  km,  $i = 57^\circ$ ,  $\Delta t = -10$  min

— ORBITER  
-- LASSII



No importance should be placed on the entire set of orbits may be shifted longitudinally to a different epoch and has no further meaning showing the geometry only.

The Tracking and Data Relay Satellite System can be used for the tracking required for the determination requirements of the LASSII Mission. TDRSS can be used to determine absolute satellite position to less than 1 km and relative positions to at least 100 m when tracking data are received from both relay satellites. Only one TDRSS is required for the LASSII Mission although the errors are somewhat higher.

A full-scale simulation of the tandem mode of operation was carried out. No additional problems are anticipated for the elliptical neighboring orbit mode.

### 5.10 LASSII Computer System

The LASSII system (Scientific Applications and Mission Processor — SCAMP) will support multiple remote users. SCAMP will have available the necessary hardware and software that will provide extensive LASSII data analysis capabilities to the LASSII experimenters.

SCAMP will consist of a 32-bit minicomputer similar to Digital Equipment Corporations' VAX 11/780. It will have 1 megabyte of local memory, system disk, real-time clock, system console, card reader, two magnetic tape units (2400 ft reels, 6250 BPI density), line printer, two local users' terminals, two plotters, an IEEE bus, and bus interface.

In addition, the SCAMP hardware configuration addresses the three critical concerns of potential users: scientific calculation capability, multiple users interface, and mass data storage.

The system will support up to 16 users via a 16-line communications multiplexer with modems. Both raw data and processed data will be available to the LASSII experimenters/scientific community via this remote system. Scientists can assess, process, print, and plot from the LASSII data base from their own offices and laboratories.

Mission data available from LASSII is approximately  $12 \times 10^9$  bytes. This can be accommodated on magnetic tape or hard disk. A recently announced 800 megabyte disk from CDC is a candidate.

The operating system will be a multi-tasking/time sharing system which will support all of the peripherals procured for SCAMP and available to the user.

## 6. REFERENCES

1. H.G. Booker and H.W. Wells, "Scattering of Radio Waves by the F-Region of the Ionosphere," *Terres. Magn. and Atmos. Elec.* **43**, 249, 1938.
2. E.P. Szuszczewicz, "Ionospheric Holes and Equatorial Spread-F Chemistry and Transport," NRL Memorandum Report 3554, July 1977.
3. R.F. Woodman and C. La Hoz, "Radar Observations of F-Region Equatorial Irregularities," *J. Geophys. Res.* **81**, 5447, 1976.

4. D.T. Farley, B.B. Balsley, R.F. Woodman, and J.P. McClure, "Equatorial Spread F: Implications of VHF Radar Observations," *J. Geophys. Res.* **75**, 7199, 1970.
5. C.H.J. Calderon, "Report on Coordinated Satellite and Incoherent Scatter Observations," Report of the Instituto Geofisico del Peru, Radio Observatorio de Jicamarca, October 1975.
6. D.T. Farley, J.P. McClure, D.L. Sterling, and J.L. Green, "Temperature and Composition of the Equatorial Ionosphere," *J. Geophys. Res.* **72**, 5837, 1967.
7. S. Hossain and B.K. Khan, "Model of Equatorial Scintillations from In-Situ Measurements," *Planet. Space Sci.* **24**, 1976.
8. W.B. Hanson and R.A. Greenwald, "Equatorial Spread F: Recent Observations and a Model," *J. Geophys. Res.* **77**, 5625, 1972.
9. W.B. Hanson, "In Situ Measurements of the Spectral Characteristics of Equatorial Spread F," *J. Geophys. Res.* **79**, 1497, 1974.
10. W.B. Hanson, "A Model for the Cause of Equatorial Spread-F," *J. Geophys. Res.* **78**, 2353, 1973.
11. D.T. Farley, "Irregularities in the Equatorial Ionosphere," *Rev. Geophys.* **12**, 285, 1974.
12. M.C. Kelley and F.S. Mozer, "A Review of Incoherent Scatter In Situ Ionospheric Irregularity Measurements and Their Relation to Electrostatic Turbulence," *Effects of the Ionosphere on Space Systems and Communications*, J.M. Goodman ed., National Science Foundation Printing Office, Washington, D.C., 1975, pp. 29-38.
13. J.P. McClure and R.F. Woodman, "Radar Observations of Equatorial Spread F in a Region of Electrostatic Turbulence," *J. Geophys. Res.* **77**, 5617, 1972.
14. J.P. McClure and W.B. Hanson, "A Catalog of Ionospheric F Region Irregularity Behavior Based on OGO-6 Retarding Potential Analyzer Data," *J. Geophys. Res.* **78**, 7431, 1973.
15. J. Aarons and R. S. Allen, "Scintillation Boundary During Quiet and Disturbed Magnetic Conditions," *J. Geophys. Res.* **76**, 170, 1971.
16. J.R. Koster, "Equatorial Scintillation," *Planet. Space Sci.* **20**, 1999, 1972.
17. H.C. Brinton, H.G. Mayr, and G.P. Newton, "Ion Composition in the Nighttime Equatorial F-Region: Implications for Chemistry and Dynamics," *EOS, Trans. Am. Geophys. Union* **56**, 1038, 1975.
18. J.P. McClure, W.B. Hanson, and J.H. Hoffman, "Plasma Bubbles and Irregularities in the Equatorial Ionosphere," *J. Geophys. Res.* **82**, 2650, 1977.
19. F.A. Morse, B.C. Edgar, H.C. Koons, C.J. Rice, W.J. Heikkila, J.H. Hoffman, B.A. Tinsley, J.D. Winningham, A.B. Chistensen, R.F. Woodman, J. Pomalaza, and N.R. Teixeira, "Equion, an Equatorial Ionospheric Irregularity Experiment," *J. Geophys. Res.* **82**, 578, 1977.
20. E.P. Szuszczewicz, "Ionospheric Holes and Equatorial Spread F: Chemistry and Transport," *J. Geophys. Res.* **83**, 2365, 1978.

21. W.B. Hanson and S. Sanatani, "Large  $N_f$  Gradients Below the Equatorial F-Peak," *J. Geophys. Res.* **78**, 1167, 1973.
22. A.J. Scannapieco and S.L. Ossakow, "Nonlinear Equatorial Spread F," *Geophys. Res. Lett.* **3**, 451, 1976.
23. W.B. Hanson, D.L. Sterling, and R.F. Woodman, "Source and Identification of Heavy Ions in the Equatorial F Layer," *J. Geophys. Res.* **77**, 5530, 1972.
24. J.W. Dungey, "Convective Diffusion in the Equatorial F Region," *J. Atmos. Terr. Phys.* **9**, 304, 1956.
25. G. Haerendel, "Theory of Equatorial Spread F," Preprint, Max-Planck Institute für Physik und Astrophysik, Garching, West Germany, 1974.
26. M.K. Hudson and C.F. Kennel, "Linear Theory of Equatorial Spread F," *J. Geophys. Res.* **80**, 4581, 1975.
27. M. Dagg, "The Origin of the Ionospheric Irregularities Responsible for Radio-Star Scintillations and Spread F, 2, Turbulent Motion in the Dynamo Region," *J. Atmos. Terres. Phys.* **11**, 139, 1957.
28. D.F. Martyn, "Large-Scale Movements of Ionization in the Ionosphere," *J. Geophys. Res.* **64**, 2178, 1959.
29. W. Calvert, "Instability of the Equatorial F Layer After Sunset," *J. Geophys. Res.* **68**, 2591, 1963.
30. M.K. Hudson, C.F. Kennel, and P.K. Kaw, "A Two-Step Drift Mode Theory of equatorial Spread F," *EOS, Trans. Am. Geophys. Union* **54**, 1147, 1973.
31. R.N. Sudan, J. Akinrimisi, and D.T. Farley, "Generation of Small-Scale Irregularities in the Equatorial Electrojet," *J. Geophys. Res.* **78**, 240, 1973.
32. P. Chaturvedi and P. Kaw, "An Interpretation for the Power Spectrum of Spread F Irregularities," *J. Geophys. Res.* **81**, 3257, 1976.
33. J.D. Huba, P.K. Chaturvedi, S.L. Ossakow, and D.M. Towle, "High Frequency Drift Waves with Wavelengths Below the Ion Gyroradius in Equatorial Spread F," *Geophys. Res. Lett.* **5**, 695, 1978.
34. M.C. Kelley, G. Haerendel, H. Kappler, A. Valenzuela, B.B. Balsley, D.A. Carter, W.L. Ecklund, C.W. Carlson, B. Häusler, and R. Torbert, "Evidence for a Rayleigh-Taylor Type Instability and Upwelling of Depleted Density Regions During Equatorial Spread F," *Geophys. Res. Lett.* **3**, 448, 1976.
35. S.L. Ossakow, S.T. Zalesak, B.E. McDonald, and P.K. Chaturvedi, "Nonlinear Equatorial Spread F: Dependence on Altitude of the F Peak and Bottomside Background Electron Density Gradient Scale Length," *J. Geophys. Res.* **84**, 17, 1979.
36. S.L. Ossakow, S.T. Zalesak, and B.E. McDonald, "Ionospheric Modification: An Initial Report on Artificially Created Equatorial Spread F," *Geophys. Res. Lett.* **5**, 691, 1978.
37. P.K. Chaturvedi and S.L. Ossakow, "Nonlinear Theory of the Collisional Rayleigh-Taylor Instability in Equatorial Spread F," *Geophys. Res. Lett.* **4**, 558, 1977.

38. M.K. Hudson, "Spread F Bubbles: Nonlinear Rayleigh-Taylor Mode in Two Dimensions," *J. Geophys. Res.* **83**, 3189, 1978.
39. E. Ott, "Theory of Rayleigh-Taylor Bubbles in the Equatorial Ionosphere," *J. Geophys. Res.* **83**, 2066, 1978.
40. S.L. Ossakow and P.K. Chaturvedi, "Morphological Studies of Rising Equatorial Spread F Bubbles," *J. Geophys. Res.* **83**, 2085, 1978.
41. E. Costa and M.C. Kelley, "On the Role of Steepened Structures and Drift Waves in Equatorial Spread F," *J. Geophys. Res.* **83**, 4359, 1978.
42. E. Costa and M.C. Kelley, "Linear Theory for the Collisionless Drift Wave Instability with Wavelengths Near the Ion Gyroradius," *J. Geophys. Res.* **83**, 4365, 1978.
43. M.C. Kelley and E. Ott, "Two-Dimensional Turbulence in Equatorial Spread F," *J. Geophys. Res.* **83**, 4369, 1978.
44. C. Barnes, Jr., Comment on Paper by Henry G. Booker, "A Local Reduction of F-Region Ionization Due to Missile Transit," *J. Geophys. Res.* **66**, 2589, 1961.
45. H.G. Booker, "A Local Reduction of F-Region Ionization Due to Missile Transit," *J. Geophys. Res.* **66**, 1073, 1961.
46. P.A. Bernhardt, C. G. Park, and P. M. Banks, "Depletion of the F2 Region Ionosphere and the Protonosphere by the Release of Molecular Hydrogen," *Geophys. Res. Lett.* **2**, 341, 1975.
47. P.A. Bernhardt, "Response of the Ionosphere to the Injection of Chemically Reactive Vapors," Technical Report No. 17, Radio Science Laboratory, Stanford Electronics Laboratories, Stanford University, May 1976.
48. N.B. Brown, H.C. Stenbaek-Nielsen, and R.D. Hunsucker, "Scarab—An F Region Ionosphere Modification Experiment Using Water," *EOS, Trans. Am. Geophys. Union* **58**, 454, 1977.
49. J.E. Jackson, H.A. Whale, and S.J. Bauer, "Local Ionospheric Disturbance Created by a Burning Rocket," *J. Geophys. Res.* **67**, 2059, 1962.
50. M. Mendillo, G.S. Hawkins, and J.A. Klobuchar, "A Large-Scale Hole in the Ionosphere Caused by the Launch of Skylab," *Science* **187**, 343, 1975.
51. M. Mendillo, G.S. Hawkins, and J.A. Klobuchar, "A Sudden Vanishing of the Ionospheric F Region Due to the Launch of Skylab," *J. Geophys. Res.* **80**, 2217, 1975.
52. M. Mendillo and J.M. Forbes, "Artificially Created Holes in the Ionosphere," *J. Geophys. Res.* **83**, 151, 1978.
53. M.B. Pongratz, G.M. Smith, C.D. Sutherland, and J. Zinn, "Lagopedo—Two F-Region Ionospheric Depletion Experiments," in *Effect of the Ionosphere on Space and Terrestrial Systems*, ed. by J.M. Goodman (Government Printing Office, Washington, D.C., 1978), p. 438.



54. G.W. Sjolander, C.Y. Johnson, J.C. Holmes, and E.P. Szuszczewicz, "Ion Composition Measurements of a Chemically Modified Ionosphere — An Initial Report," in *Effect of the Ionosphere on Space and Terrestrial Systems*, ed. by J.M. Goodman (Government Printing Office, Washington, D.C., 1978), p. 442.
55. D.N. Anderson and P.A. Bernhardt, "Modeling the Effects of an  $H_2$  Gas Release on the Equatorial Ionosphere," *J. Geophys. Res.* **83**, 4777, 1978.
56. G.W. Sjolander and E.P. Szuszczewicz, "Chemically Depleted  $F_2$  Ion Composition: Measurements and Theory," *J. Geophys. Res.*, 1979.
57. M.A. Biondi, "Atmospheric Electron-Ion and Ion-Ion Recombination Processes," *Can. J. Chem.* **47**, 1711, 1969.
58. M.A. Biondi, "Charged Particle Recombination Processes," in *Reaction Rate Handbook*, 2nd ed., DNA 1948H, ed. by M.H. Bortner and T. Baurer (DASIAC, GE TEMPO, Santa Barbara, Calif., 1972), p. 16-1.
59. W. Lindinger, F.C. Fehsenfeld, A.L. Schmeltekopf, and E.E. Ferguson, "Temperature Dependence of Some Ionospheric Ion-Neutral Reactions from 300° - 900°K," *J. Geophys. Res.* **79**, 4753, 1974.
60. M. Oppenheimer, A. Dalgarno, F.P. Trebino, L.H. Brace, H.C. Brinton, and J.H. Hoffman, "Day-time Chemistry of  $NO^+$  from Atmosphere Explorer-C Measurements," *J. Geophys. Res.* **82**, 191, 1977.
61. D.G. Torr, M.R. Torr, J.C.G. Walker, L.H. Brace, H.C. Brintron, W.B. Hanson, J.H. Hoffman, A.O. Nier, and M. Oppenheimer, "Recombination of  $NO^+$  in the Ionosphere," *Geophys. Res. Lett.* **3**, 209, 1976.
62. M. Oppenheimer, A. Dalgarno, and L. Brace, "Recombination Rate Coefficient of  $NO^+$  from Thermosphere Daytime Photochemistry," *EOS, Trans. Am. Geophys. Union* **57**, 297, 1976.
63. S.L. Ossakow, "Research at NRL on Theoretical and Numerical Simulation Studies of Ionospheric Irregularities," NRL Memorandum Report 2907, October 1974.
64. J.C. Holmes and E.P. Szuszczewicz, "Versatile Plasma Probe," *Rev. Sci. Instrum.* **46**, 592, 1975.
65. E.P. Szuszczewicz and J.C. Holmes, "Surface Contamination of Active Electrodes in Plasmas: Distortion of Conventional Langmuir Probe Measurements," *J. Appl. Phys.* **46**, 5134, 1975.
66. W. Bernstein, H. Leinbach, H. Cohen, P.S. Wilson, T.N. Davis, T. Hallinan, B. Baker, J. Martz, R. Zeimke, and W. Huber, "Laboratory Observations of RF Emissions at  $\omega_{pe}$  and  $(N + 1/2) \omega_{ce}$  in Electron Beam-Plasma and Beam-Beam Interactions," *J. Geophys. Res.* **80**, 4375, 1975.
67. W. Bernstein, H. Leinbach, and B. Baker, "Preliminary Results from the Electron Beam-Plasma Experiments in the Very Large Vacuum Facilities at Plum Brook and Johnson Space Center," NOAA Technical Memorandum ERL-SEL 50, August 1977.
68. W. Bernstein, H. Leinbach, P. Kellogg, S. Monson, T. Hallinan, O.K. Garriott, A. Konradi, J. McCoy, P. Daly, B. Baker, and H.R. Anderson, "Electron Beam Injection Experiments: The Beam-Plasma Discharge at Low Pressures and Magnetic Field Strengths," *Geophys. Res. Lett.* **5**, 127, 1978.

69. E.P. Szuszcwicz, "Plasma Diffusion in a Space-Simulation Beam-Plasma Discharge," *Geophys. Res. Lett.* **6**, 201, 1979.
70. F.O. Vonbun, P.D. Argentiero, and P.E. Schmid, "Orbit Determination Accuracies Using Satellite-to-Satellite Tracking," GSFC X-932-77-189, October 1977.
71. P. Argentiero and F. Loveless, "Orbit Determination with the Tracking Data Relay Systems," GSFC X-932-76-185, February 1977.
72. P.E. Schmid, P.D. Argentiero, and F.O. Vonbun, "Satellite-to-Satellite System and Orbital Error Estimates," GSFC X-932-76-5, January 1976.
73. M.J. Keskinen, E.P. Szuszcwicz, S.L. Ossakow, and J.C. Holmes, "Nonlinear Theory and Experimental Observations of the Local Collisional Rayleigh-Taylor Instability in a Descending Equatorial Spread F Ionosphere," *J. Geophys. Res.* **86**, 5785, 1981.
74. R.S. Narcisi and E.P. Szuszcwicz, "Direct Measurements of Electron Density, Temperature and Ion Composition in an Equatorial Spread F Ionosphere," *J. Atm. Terr. Phys.* **43**, 463, 1981.
75. R.T. Tsunoda, "Time Evolution and Dynamics of Equatorial Backscatter Plumes—Growth Phase," *J. Geophys. Res.* **86**, 139, 1981.
76. E.P. Szuszcwicz, J.C. Holmes and M. Singh, "The S3-4 Ionospheric Irregularities Satellite Experiment: Probe Detection of Multi-Ion Component Plasma and Associated Effects on Instability Processes," *J. Astrophys. and Sp. Science*, 1982 (in press).
77. M. Singh, E.P. Szuszcwicz and J.C. Holmes, "The STP/S3-4 Satellite Experiment: Equatorial F-Region Irregularities," NRL Memorandum Report 4531, July 14, 1981.
78. P. Rodriguez, E.P. Szuszcwicz, D.N. Walker, and M. Singh, "The STP/S3-4 Satellite Experiment: High-Latitude Large Scale Density Irregularities," NRL Memorandum Report 4514, May 26, 1981.
79. W. Bernstein, H. Leinbach, P.J. Kellogg, S.J. Manson, and T. Hallinan, "Further Laboratory Measurements of the Beam-Plasma-Discharge," *J. Geophys. Res.* **84**, 7271, 1979.
80. R.J. Jost, H.R. Anderson, and J.D. McGarity, "Measured Electron Energy Distributions During Electron Beam-Plasma Interactions," *Geophys. Res. Lett.* **7**, 509, 1980.
81. E.P. Szuszcwicz, K. Papadopoulos, W. Bernstein, C.S. Lin, and D.N. Walker, "Threshold Criterion for Space-Simulation Beam-Plasma Discharge," *J. Geophys. Res.* **87**, 1565, 1982.

ATE  
LMED  
8